


1-1-2016

# Multiferroicity In Iron Vanadate, Magnetite And Polyvinylidene Fluoride Nanocomposite Films

Ehab Hamdy Abdelmonaim Abdelhamid  
*Wayne State University,*

Follow this and additional works at: [https://digitalcommons.wayne.edu/oa\\_dissertations](https://digitalcommons.wayne.edu/oa_dissertations)

 Part of the [Condensed Matter Physics Commons](#), and the [Materials Science and Engineering Commons](#)

---

## Recommended Citation

Abdelhamid, Ehab Hamdy Abdelmonaim, "Multiferroicity In Iron Vanadate, Magnetite And Polyvinylidene Fluoride Nanocomposite Films" (2016). *Wayne State University Dissertations*. 1503.  
[https://digitalcommons.wayne.edu/oa\\_dissertations/1503](https://digitalcommons.wayne.edu/oa_dissertations/1503)

This Open Access Dissertation is brought to you for free and open access by DigitalCommons@WayneState. It has been accepted for inclusion in Wayne State University Dissertations by an authorized administrator of DigitalCommons@WayneState.

**MULTIFERROICITY IN IRON VANADATE, MAGNETITE AND  
POLYVINYLIDENE FLUORIDE NANOCOMPOSITE FILMS**

by

**EHAB ABDELHAMID**

**DISSERTATION**

Submitted to the Graduate School

of Wayne State University,

Detroit, Michigan

in partial fulfillment of the requirements

for the degree of

**DOCTOR OF PHILOSOPHY**

2016

MAJOR: PHYSICS

Approved By:

---

Advisor

Date

---

Co-advisor

Date

---

---

---

## ACKNOWLEDGEMENTS

*“I have some good news to share: I got accepted in a graduate program in the US!”*

*“That sounds good! But you may need to reconsider. We are leading a good life here, why take the risk?”*

It was the night of January 30<sup>th</sup> 2009, when this conversation took place between me and my wife to be –then– Doaa. I had received the acceptance email from Dr. Ratna Naik, the Department Chair –then– only two weeks before our date of marriage. Both Doaa and I had to quit our jobs to move to the US and start our journey at Wayne State. It has been a long journey, I have to say, full of as many downs as ups as well, but as the saying goes: *“A calm sea does not make a skilled sailor”*. Looking back at it now, I do not regret seizing the opportunity, and I appreciate everyone’s contribution to the moment of my graduation.

This list of thanks can be as long as a thesis chapter by itself, and it starts with my beloved wife Doaa, who left her job, family and friends to be with me on my quest. Her contribution extends to getting me through my moments of gloom throughout the past seven years. She has, and is, always reminding me of my strengths. I owe her for believing in me more than myself.

I’m deeply grateful for all my professors. Each one of them contributed to shaping my scientific mind in some proportion. I’m specifically thankful to my advisors, Dr. Boris Nadgorny and Dr. Ratna Naik, for taking the responsibility of guiding me after the abrupt leave of Dr. Gavin Lawes due to his heartwrenching diagnosis. It is for their efforts that I could make it through. On the same note, I really missed Dr. Lawes’ expertise in almost every day of my PhD work. I wish he could have witnessed my graduation and I think I would have made him proud.

My thanks extend to Dr. Ambesh Dixit, the former colleague and current assistant professor at IIT Jodhpur, India. He taught me most of my lab skills and contributed to my knowledge through face to face and online conversations. Most of the work presented herein is only possible because of his input.

The list goes on to include Dr. Onattu Jayakumar at Bhabha research center in India, who spent a couple of months at Wayne, during which he taught me many useful materials synthesis techniques. I'm also grateful to him and to Dr. Balaji Mandal for providing the sets of PVDF-based samples over which chapter 4 in this thesis is built. On a related note, I thank Dr. Vaman Naik and Dr. Ratna Naik, for without their input, this chapter wouldn't have seen light.

I'm also grateful to Dr. Alan Sebastian for all the hands-on help provided in lab and for all the useful hints and tricks I learnt from him. On the same note, I thank Dr. Gholam Abbas Nazri for his help in the lab on repeated occasions.

I would like to express my gratitude to Dr. Jogindra Wadehra, Dr. Giovanni Bonvicini, Dr. Paul Keyes and Dr. Ashis Mukhopadhyay for being wonderful teachers. I tried not only to learn physics concepts from them, but to grasp classroom smartness as well.

Thanks to Dr. Scott Payson for maintaining a friendly work environment and for his help during my time as a teaching assistant. I've always enjoyed casual conversations with him.

I'm also grateful to Dr. Tsuyoshi Kimura in Osaka University, Japan, for hosting me during the spring of 2014 in his lab. It was in his lab where I learnt the technique of single crystals growth, which I used to make the samples needed for my studies.

I thank Dr. Zhixian Zhou and Dr. Zhi-Feng Huang at Wayne Physics, and Dr. Susil Putatunda at the College of Engineering, for agreeing to participate in my research committee.

I appreciate all the moments I've shared with past and current graduate students at Wayne State. A list of their names can go for miles, so to mention a few I thank Dr. Humeshkar Nemala, Dr. Rupam Mukherjee, Dr. Suvra Laha, Dr. Akila Kumarasiri, Dr. Girfan Shamsutdinov, Dr. Kulwinder Dhindsa, Dr. Vinicio Tarquini, Maheshika Perera, Ajay Kumar, Wissam Fawaz, Chris Zin, Garrett Godfrey, Zhe Wu, Tal Knighton, Ed Kramkowski, Joydeep Roy,...

At last, I'm deeply grateful for my parents for their non-ending support and love. In my ongoing strive to success; it is always my goal to make them proud, in a trivial attempt to match their sacrifices for me.

# TABLE OF CONTENTS

<b>Acknowledgements</b> . . . . .	ii
<b>List of Tables</b> . . . . .	viii
<b>List of Figures</b> . . . . .	ix
<b>Chapter 1 Introduction</b> . . . . .	1
1.1 Types of magnetic ordering . . . . .	1
1.1.1 Linear ordering: diamagnetism and paramagnetism . . . . .	2
1.1.2 Nonlinear ordering: Ferro- Ferri- and Antiferro- magnetism . . . . .	4
1.1.3 Nanomagnets: superparamagnetism . . . . .	7
1.1.4 Exotic magnetic ordering: spiral and helical magnets . . . . .	10
1.2 Magnetic frustration . . . . .	12
1.3 Ferroelectricity . . . . .	14
1.4 Multiferroics . . . . .	17
1.4.1 Types of ferroelectric ordering in multiferroics . . . . .	19
1.4.2 Scarcity of multiferroics . . . . .	22
1.5 Hexaferrites . . . . .	23
1.6 Hybrid multiferroics . . . . .	24
1.7 Scope of the thesis . . . . .	25
<b>Chapter 2 Ferroelectric and Magnetic Anisotropy in Iron Vanadate (FeVO<sub>4</sub>) Single Crystals</b> . . . . .	27
2.1 Background and previous work . . . . .	27
2.2 Experiments and results . . . . .	33
2.2.1 FeVO <sub>4</sub> single crystals preparation . . . . .	33

2.2.2	Structural characterization . . . . .	35
2.2.3	Magnetic measurements . . . . .	39
2.2.4	Dielectric and ferroelectric measurements . . . . .	42
2.2.5	Magneto-dielectric coupling . . . . .	47
2.3	Doped FeVO <sub>4</sub> single crystals . . . . .	50
2.4	Conclusions and future work . . . . .	60
<b>Chapter 3</b>	<b>Dielectric and Magneto-dielectric Properties of Gd-doped Fe<sub>3</sub>O<sub>4</sub> Nanoparticles . . . . .</b>	<b>63</b>
3.1	Background and previous work . . . . .	63
3.2	Experiments and results . . . . .	69
3.2.1	Nanoparticles preparation and characterization . . . . .	69
3.2.2	Magnetic data (summary) . . . . .	69
3.2.3	Dielectric properties . . . . .	70
3.2.4	Magneto-dielectric coupling . . . . .	74
3.2.5	Ferroelectric properties . . . . .	76
3.2.6	Temperature dependent XRD and heat capacity . . . . .	78
3.3	Conclusions and future work . . . . .	80
<b>Chapter 4</b>	<b>Magneto-dielectric Coupling in Polyvinylidene Fluoride (PVDF)-based Nanocomposite Films . . . . .</b>	<b>83</b>
4.1	Overview and previous work . . . . .	83
4.2	Experimental work . . . . .	86
4.2.1	PVDF–Fe <sub>3</sub> O <sub>4</sub> hybrid films with reduced graphene oxide (RGO) and zinc oxide (ZnO) nanofillers . . . . .	86
4.2.2	PVDF films loaded with Fe <sub>3</sub> O <sub>4</sub> and graphene Oxide (GO) . . . . .	94
4.2.3	PVDF-Ni nanohybrids . . . . .	98

4.2.4	Magneto-dielectric properties in PVDF-Barium hexaferrite (BaFe <sub>12</sub> O <sub>19</sub> ) composite films . . . . .	100
4.3	Conclusions . . . . .	101
<b>Chapter 5</b>	<b>Summary and Future Work . . . . .</b>	<b>105</b>
<b>Appendix</b>	<b>Single Crystals Synthesis Using Flux Growth Method . . . . .</b>	<b>108</b>
<b>Bibliography</b>	<b>. . . . .</b>	<b>113</b>
<b>Abstract</b>	<b>. . . . .</b>	<b>126</b>
<b>Autobiographical Statement</b>	<b>. . . . .</b>	<b>128</b>



## LIST OF TABLES

<b>Table 2.1:</b> Measured lattice parameters of FeVO <sub>4</sub> as given in Ref [71]. The figure in parenthesis gives the uncertainty in the last digit . . . . .	28
<b>Table 2.2:</b> Lattice parameters of undoped FeVO <sub>4</sub> , measured by single crystal XRD, estimated using Rietveld fitting and as reported by Robertson <i>et al.</i> [71] . . . . .	38
<b>Table 2.3:</b> Masses (in grams) of precursors used to prepare undoped, Zn- and Mn-doped FeVO <sub>4</sub> single crystals . . . . .	51
<b>Table 2.4:</b> Aimed and measured stoichiometric ratios for Zn- and Mn-doped FeVO <sub>4</sub> crystals . . . . .	52
<b>Table 2.5:</b> Effective moment ( $\mu_{\text{eff}}$ ) and Curie-Weiss temperature ( $\theta_{\text{CW}}$ ) values for pristine and doped FeVO <sub>4</sub> single crystals. The listed values for $\mu_{\text{eff}}$ are in Bohr magneton ( $\mu_{\text{B}}$ ), and values of $\theta_{\text{CW}}$ are in kelvin . . . . .	56
<b>Table 4.1:</b> PVDF composite films and their $\beta$ -phase fractions . . . . .	90
<b>Table 4.2:</b> Magnetostriction and saturation magnetization values of the magnetic nanofillers reported in this chapter, along with the reference in which each values is reported . . . . .	104

## LIST OF FIGURES

<b>Figure 1.1:</b> Schematic M-H plot of (a) a diamagnetic sample and (b) a paramagnetic sample . . . . .	2
<b>Figure 1.2:</b> Schematic representation of ferromagnetic domains . . . . .	5
<b>Figure 1.3:</b> Schematic representation of a typical hysteresis loop . . . . .	6
<b>Figure 1.4:</b> Qualitative relation between coercivity and particle size . . . . .	8
<b>Figure 1.5:</b> ZFC-FC curves obtained for Fe <sub>3</sub> O <sub>4</sub> nanoparticles . . . . .	9
<b>Figure 1.6:</b> M-H curves for Fe <sub>3</sub> O <sub>4</sub> nanoparticles above and below the blocking temperature (200 K, refer to figure 1.5) . . . . .	10
<b>Figure 1.7:</b> (a) Schematic representation of spiral and helical ordering patterns and (b) Spin arrangement of Ni <sup>+2</sup> ions in Ni <sub>3</sub> V <sub>2</sub> O <sub>8</sub> . The red and blue spheres are Nickel ions at two different crystallographic locations. Coupling between two ‘red’ Nickel ions is different than coupling between ‘red’ and ‘blue’ ones . . . . .	11
<b>Figure 1.8:</b> (a) Ising spins on a triangular lattice. It is not possible for each spin to be antiparallel with all its neighbors. (b) The ground state of a triangular cluster of Heisenberg spins . . . . .	12
<b>Figure 1.9:</b> 2D (top) and 3D (bottom) frustrated crystal structures . . . . .	13
<b>Figure 1.10:</b> P-E hysteresis measured at room temperature for BaTiO <sub>3</sub> 300 nm particles . . . . .	15
<b>Figure 1.11:</b> Perovskite ABO <sub>3</sub> crystal structure. Yellow and blue spheres depict the locations of A and B ions respectively. The oxygen ions are represented by red spheres (photo courtesy of chem.yale.edu) . . . . .	16
<b>Figure 1.12:</b> Space and time symmetry restrictions on different ferroic orders . . . . .	18
<b>Figure 1.13:</b> Schematic representation of different multiferroic classes, with the corresponding order parameters and coupling coefficients . . . . .	18
<b>Figure 1.14:</b> Development of ferroelectric order via charge ordering . . . . .	20
<b>Figure 1.15:</b> Vector diagram representation of Dzyaloshinskii-Moriya interaction (Courtesy of Wikipedia.org) . . . . .	21
<b>Figure 1.16:</b> Spontaneous distortion of the oxygen ions octahedron surrounding an Mn <sup>3+</sup> ion as an example on Jahn-Teller effect. Such distortion is sometimes favored because the energy cost of increased elastic energy is balanced by a resultant electronic energy	

saving . . . . .	23
<b>Figure 2.1:</b> Trigonal bipyramidal (left) and octahedral (right) environments of iron in FeVO <sub>4</sub> . . . . .	28
<b>Figure 2.2:</b> Two S-shaped clusters of iron ions (small circles), projected on the a-b plane. The Fe—O bonds are represented by solid lines, and oxygen ions are represented by the large spheres . . . . .	29
<b>Figure 2.3:</b> The three symmetrically inequivalent Fe <sup>3+</sup> sites (represented by colored solid spheres) connected by VO <sub>4</sub> tetrahedra (pale blue). It is important to note that the choice of lattice parameters here is different than those in figure 2.2 . . . . .	29
<b>Figure 2.4:</b> Magnetic structure inside the centrosymmetric S-shaped clusters pair in FeVO <sub>4</sub> . . . . .	31
<b>Figure 2.5:</b> A model representing the vector relation between spins $\vec{e}_1$ , $\vec{e}_2$ , the resulting spin current and electric polarization . . . . .	32
<b>Figure 2.6:</b> (a) The platinum crucible inside the alumina crucible. (b) and (c) A few retrieved single crystals showing their length scale . . . . .	34
<b>Figure 2.7:</b> Illustration of the annealing process applied to grow FeVO <sub>4</sub> single crystals . . . . .	34
<b>Figure 2.8:</b> (a) Powder XRD diffraction pattern obtained for ground FeVO <sub>4</sub> single crystals and (b) Raman spectrum for FeVO <sub>4</sub> single crystals . . . . .	36
<b>Figure 2.9:</b> Rietveld fitting for the XRD spectrum of the undoped FeVO <sub>4</sub> sample . . . . .	37
<b>Figure 2.10:</b> FeVO <sub>4</sub> unit cell, constructed from the single crystal diffractometer data . . . . .	38
<b>Figure 2.11:</b> Magnetic susceptibility and inverse magnetic susceptibility versus temperature data for FeVO <sub>4</sub> single crystals, with the crystals oriented perpendicular to and parallel to the crystallographic axis <i>a</i> . . . . .	40
<b>Figure 2.12:</b> Reversible ferroelectric polarization perpendicular to the crystal long axis (a) and parallel to it (b). The insets in (a) and (b) represent the recorded pyrocurrent signals . . . . .	45
<b>Figure 2.13:</b> Repeated measurements of ferroelectric polarization on different FeVO <sub>4</sub> crystals perpendicular <i>a</i> (a) and along <i>a</i> (b). The different curve colors represent different runs . . . . .	46
<b>Figure 2.14:</b> Relative dielectric constant of FeVO <sub>4</sub> single crystals measured perpendicular to the <i>a</i> -axis (left, black scale) and parallel to the <i>a</i> -axis (right, red scale). The inset shows the relative change in the parallel and perpendicular components of $\epsilon_r$ . . . . .	47

<b>Figure 2.15:</b> Magneto-dielectric coupling perpendicular (a) and parallel (b) to $a$ . The abscissa is the change in dielectric constant with reference to the value at $H = 0$ Tesla . . . . .	49
<b>Figure 2.16:</b> Isothermal $M$ vs $H$ data for $\text{FeVO}_4$ single crystals . . . . .	50
<b>Figure 2.17:</b> The magnetic susceptibility values estimated from the isothermal $M$ - $H$ plots in figure 2.16 . . . . .	50
<b>Figure 2.18:</b> XRD spectra for undoped $\text{FeVO}_4$ and (a) Zn-doped samples and (b) Mn-doped ground crystals. The grey lines at the bottom indicate the positions of the lines listed in the standard powder diffraction file . . . . .	53
<b>Figure 2.19:</b> Raman spectra of undoped and Zn-doped $\text{FeVO}_4$ crystals . . . . .	54
<b>Figure 2.20:</b> Inverse susceptibility versus temperature data for doped $\text{FeVO}_4$ single crystals recorded along the crystallographic axis $a$ and perpendicular to it. The insets highlight the lack of signals to the collinear-to-non-collinear AFM transition around 15 K in case $H$ is parallel to $a$ . . . . .	55
<b>Figure 2.21:</b> Relative change in dielectric constant of (a) Zn-doped and (b) Mn-doped $\text{FeVO}_4$ single crystals, recorded with an electric field perpendicular to the crystallographic axis $a$ . . . . .	57
<b>Figure 2.22:</b> Pyrocurrent (a,b) and polarization moment (c,d) data for the Zn- and Mn-doped $\text{FeVO}_4$ crystals . . . . .	58
<b>Figure 2.23:</b> Reversible ferroelectric polarization of Zn-doped $\text{FeVO}_4$ crystals . . . . .	59
<b>Figure 2.24:</b> The the magnetic effective moment ' $\mu_{eff}$ ' and ferroelectric polarization ' $P$ ' as functions in zinc content in $\text{FeVO}_4$ single crystals . . . . .	59
<b>Figure 3.1:</b> Representation of the tetrahedral and octahedral sites in the spinel structure . . . . .	64
<b>Figure 3.2:</b> Pyrochlore lattice made up by the B sites of the spinel structure. The iron ions are found at the corners of the tetrahedra. The oxygen ions are not shown here for simplicity . . . . .	65
<b>Figure 3.3:</b> Iron ions positions in the paraelectric monoclinic $P2/c$ (left) and the ferroelectric $Cc$ (right) structures. The red arrows indicate the direction of electric dipole moments created by charge ordering . . . . .	68
<b>Figure 3.4:</b> Change in relative dielectric constant ( $\epsilon_r$ ) and dielectric loss of $\text{Fe}_3\text{O}_4$ and Gd-doped $\text{Fe}_3\text{O}_4$ nanoparticles versus temperature. The data for Gd-2.5 sample was recorded only up to 80 K . . . . .	72
<b>Figure 3.5:</b> Semi-log straight line fits of dielectric loss peak frequencies vs temperature . . . . .	

reciprocal for pure and Gd-doped Fe <sub>3</sub> O <sub>4</sub> . . . . .	73
<b>Figure 3.6:</b> Frequency dependence of the dielectric constant (left axes) and dielectric loss tangent (right axes) for Gd-0 and Gd-5 samples at 300 K . . . . .	74
<b>Figure 3.7:</b> Relative change in dielectric constant and dielectric loss tangent as a function of magnetic field for Gd-0 and Gd-5 samples . . . . .	75
<b>Figure 3.8:</b> Calculated ferroelectric polarization moment for Gd-0 and Gd-5. The measured pyrocurrent signals are included in the insets . . . . .	77
<b>Figure 3.9:</b> XRD patterns recorded at different temperatures in the vicinity of Verwey transition for Fe <sub>3</sub> O <sub>4</sub> . The curves are vertically displaced for clarity . . . . .	78
<b>Figure 3.10:</b> Heat capacity of sample Gd-0. The inset shows a $\frac{C}{T^2}$ vs T plot . . . . .	80
<b>Figure 4.1:</b> Structure of vinylidene difluoride, the PVDF monomer . . . . .	84
<b>Figure 4.2:</b> (a) The non-polar $\alpha$ -PVDF phase and (b) the polar $\beta$ -PVDF phase . . . . .	85
<b>Figure 4.3:</b> XRD patterns of commercial PVDF film, prepared pristine PVDF and composite films . . . . .	87
<b>Figure 4.4:</b> Low resolution SEM images for PVDF films . . . . .	88
<b>Figure 4.5:</b> (a) Raman spectra for the PVDF films prepared for this study and the commercial PVDF film. (b) Lorentzian-Gaussian peak fits to the PVDF films spectra . . . . .	89
<b>Figure 4.6:</b> (A) Dielectric constant vs frequency plots, (B) P-E curves, (C) M vs H curves, (D) MD coupling and (E) Dielectric loss vs frequency of (a) PVDF, (b) PVDF-RGO, (c) PVDF-RGO-Fe <sub>3</sub> O <sub>4</sub> , (d) PVDF-RGO-Fe <sub>3</sub> O <sub>4</sub> -ZnO and (e) PVDF-ZnO. Inset in (C) shows FC and ZFC curves for PVDF-RGO-Fe <sub>3</sub> O <sub>4</sub> -ZnO . . . . .	92
<b>Figure 4.7:</b> (A) XRD spectra of PVDF composite films. The inset highlights the GO characteristic peak at $2\theta = 9.6^\circ$ . (B) FTIR spectra for PVDF (a), PVDF-GO (b), PVDF-Fe <sub>3</sub> O <sub>4</sub> (c) and PVDF-GO-Fe <sub>3</sub> O <sub>4</sub> (d) . . . . .	95
<b>Figure 4.8:</b> Room temperature P-E loops at 100 Hz of undoped PVDF and composite films . . . . .	96
<b>Figure 4.9:</b> (a) Dielectric constant and (b) dielectric loss dependence on frequency at room temperature . . . . .	96
<b>Figure 4.10:</b> (a) MD coupling for composite films at room temperature and (b) MD coupling for the PVDF-GO-Fe <sub>3</sub> O <sub>4</sub> film at different temperatures . . . . .	98

<b>Figure 4.11:</b> ZFC-FC curves for the PVDF-GO-Fe <sub>3</sub> O <sub>4</sub> film . . . . .	98
<b>Figure 4.12:</b> MD coupling of the (a) PVDF-Ni and (b) PVDF-functionalized Ni films .	100
<b>Figure 4.13:</b> MD coupling of undoped and lower BHF percentage PVDF films . . . .	101
<b>Figure 4.14:</b> MD coupling in nanofillers loaded PVDF films as a function of magnetostriction and saturation magnetization of the magnetic nanofillers . . . . .	103

## CHAPTER 1: INTRODUCTION

For over a century, understanding the properties of the solid state of matter has been the concern for physicists from all around the globe. Since the beginning of the twentieth century the field has experienced several revolutionary discoveries and inventions. However, many scientists believe that it was the establishment of the field of quantum mechanics that created a paradigm shift in our understanding of condensed matter physics [1]. For instance, the study of magnetic properties of materials is a major sub-area of condensed matter physics. A firm understanding of the field of magnetism is never possible outside the scope of quantum physics.

The interaction between humans and magnetic materials goes back to the oldest known civilizations, but the onset of understanding the physics of magnetism is only about one hundred years old. It is in the light of quantum mechanics that scientists could explain the behavior of magnetic materials in terms of the electron spin and orbital motion. With the spin defined as a fundamental physics quantity, models of microscopic magnetic ordering could be put in words. A description of different known regimes of magnetic ordering is given over the next few pages.

### 1.1 TYPES OF MAGNETIC ORDERING

The magnetic behavior of materials can be qualitatively understood with Bohr's atomic model in mind. According to this model, the negatively charged electrons fill the space around the positively charged nucleus in energy levels hierarchy. In this picture, the electrons manifest two types of angular momenta; orbital and spin, with each type giving rise to a part of the electrons' magnetic moment. In their arrangement within individual energy levels, the electrons are further ordered in sub-levels or orbitals, and each orbital is considered full when it hosts two electrons. Furthermore, Pauli exclusion principle dictates that once two electrons share an

orbital, they must have opposite spins. The distribution of electrons among atomic levels and orbitals is what determines how the material interacts to an external magnetic field.

### 1.1.1 LINEAR ORDERING: DIAMAGNETISM AND PARAMAGNETISM

In response to an applied external magnetic field ( $H$ ), the sample will develop a measurable magnetization ( $M$ ). Materials can be classified in two broad categories in terms of their  $M$  vs  $H$  plot. If the  $M$ - $H$  graph is depicted by a straight line, the material is said to exhibit linear magnetic ordering. On the other hand, nonlinear ordering refers to an  $M$ - $H$  relation that is not a straight line. Nonlinear ordering is discussed in more details in the next section.

For a linear  $M$ - $H$  plot, the slope can be either positive or negative. A negative slope denotes a diamagnetic sample (Fig 1.1(a)). Usually, diamagnetic substances would be characterized by energy levels and orbitals which are completely filled with electrons [2]. In the absence of external magnetic field, the sample would show no measurable magnetization. However, when the field is non-zero, the electrons will be oriented to always give rise to a small negative magnetization, with respect to the direction of the applied field. Some substances belonging to this category are inert gases, water and most covalent compounds.

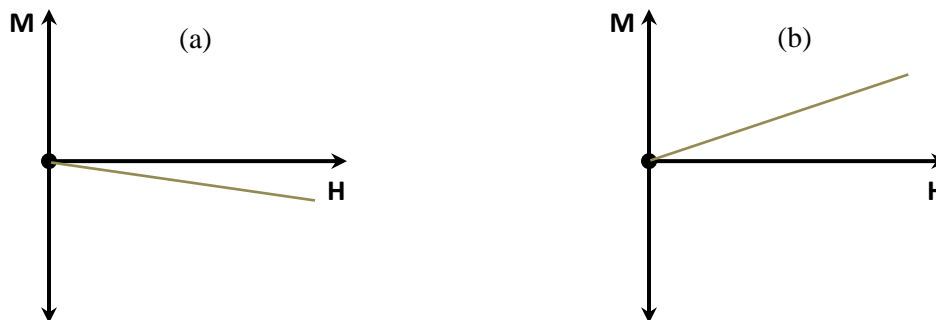


Figure 1.1: Schematic  $M$ - $H$  plot of (a) a diamagnetic sample and (b) a paramagnetic sample.

It is useful to define the slope of  $M$  vs  $H$  plot as the magnetic susceptibility  $\chi$ . For a typical diamagnet,  $\chi$  is negative and in the order of  $\sim 10^{-6}$  [3].



Diamagnetism is also found to occur with superconductivity. In fact, superconductors are characterized by being perfect diamagnets, with  $\chi = -1$ . The origin of diamagnetism in superconductors, however, is more complicated than the simple saturated orbitals notion [2].

It worth noting here that since diamagnetism is synonymous to fully occupied energy levels, all of the known elements and compounds in our universe (except for atomic hydrogen) show some degree of diamagnetism. But since diamagnetism is such a weak property, it is usually screened by other magnetic responses, such as paramagnetism.

The existence of unpaired electrons, whose accommodation among orbitals is governed by Hund's rules, gives rise to a net atomic magnetic moment. If no interaction occurs between the individual atomic moments, these will be randomly oriented, and randomly fluctuating, inside the system, and the material on average would have no net magnetic moment. If an external magnetic field is applied, the moments align themselves parallel to the external field in order to decrease their potential energy, producing a net magnetization in the system. This process is governed by Maxwell-Boltzmann statistics; the net moment value increases with higher magnetic field (before a saturation value is reached), and decreases with higher temperature. This behavior is called paramagnetism. Typical values of paramagnetic susceptibility are positive and in the order of  $10^{-4}$  (Fig 1.1(b)).

At low fields, the paramagnetic susceptibility is related to the absolute temperature by Curie's law (Eq 1.1), where  $C$  is called Curie's constant, and it carries dependence on the system's orbital and spin quantum numbers.

$$\chi = \frac{C}{T} \quad (1.1)$$

Generally speaking, any material with atoms having unpaired electrons will be paramagnetic unless long range ordering occurs. In some cases, the local magnetic moments on

each atom may interact. These interactions are produced by the overlap of electronic wave functions among different atoms in the system, together with the Pauli exclusion principle. If such interactions arise, long range ordering of the magnetic moments occurs, and the M-H relation is no longer a straight line.

### 1.1.2 NONLINEAR ORDERING: FERRO- FERRI- AND ANTIFERRO- MAGNETISM

The inter-atomic interaction which gives rise to long range order is described by the Heisenberg Hamiltonian (Eq 1.2):

$$H_{exchange} = - \sum_{i,j} J \vec{S}_i \cdot \vec{S}_j \quad (1.2)$$

$\vec{S}_i$  and  $\vec{S}_j$  are the spin angular momenta of the  $i^{\text{th}}$  and  $j^{\text{th}}$  atom.  $J$  is called the exchange integral and it depends on the pair of atoms involved. When  $J$  is positive, an energy minimum is achieved through parallel alignment of moments. This phenomenon is known as ferromagnetism. Conversely, antiparallel arrangement of moments is favored in systems with negative  $J$  values, such systems shall be called antiferromagnets when  $\vec{S}_i$  and  $\vec{S}_j$  are equal, or ferrimagnets when  $\vec{S}_i \neq \vec{S}_j$ .

In ferromagnetic systems, we can see from the last expression that minimizing the interaction energy requires aligning all the moments in a given sample to be parallel, giving rise to a large single domain. However, this normally does not happen in macroscopic systems because magnetostatic energy increases linearly with the domain size. This favors the formation of multiple small domains rather than a single large one. Nonetheless, smaller domains imply larger domain wall area, which increases the domain wall energy. As a result of this contest, real systems are divided into magnetic domains separated by domain walls when they order ferromagnetically (Fig 1.2).

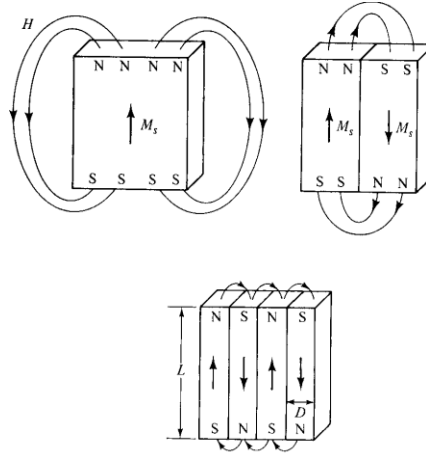


Figure 1.2: Schematic representation of ferromagnetic domains [2].

These domains are randomly oriented, and the net magnetic field along any direction is nearly zero. On applying an external magnetic field, magnetic domains aligned along the field direction will grow, eventually producing one large domain, whose magnetization is parallel to the external applied field. At this point, the sample is saturated. If the external field is now turned off, the sample does not return to complete randomness again, but rather retains a remanent magnetization ( $M_r$ ). One needs to apply a negative external magnetic field, called the coercive field ( $H_c$ ), to reduce magnetization to zero. The relation between the external magnetic field and the sample magnetization in this case depends on the sample's history and is non-linear, hence given the name hysteresis loop (Figure 1.3).

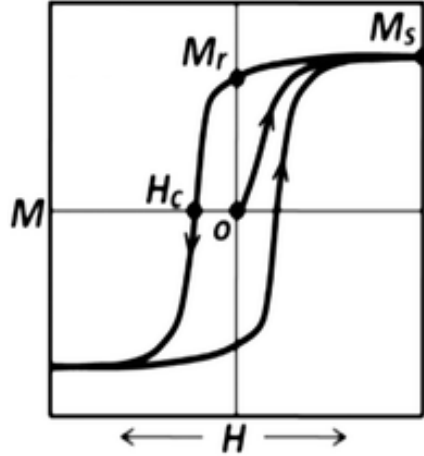


Figure 1.3: Schematic representation of a typical hysteresis loop [4].

A material with a high coercive field value is called a hard magnet. Such behavior is useful in memory applications. On the other hand, materials having low coercivity are labeled soft magnets, and are suitable in transformers and motor cores.

Long range ordering interactions given in equation 1.2 prevail only below a certain transition temperature. This behavior is parameterized in the light of Landau mean field theory in terms of a slight modification to Curie's law:

$$\chi = \frac{C}{T - T_c} \quad (1.3)$$

Where  $T_c$  is a constant called Curie temperature for ferromagnets, and Neel temperature for antiferromagnets. Equation 1.3 is called Curie-Weiss law, and it suggests a singularity in susceptibility in the vicinity of  $T_c$ . Above  $T_c$ , the system becomes paramagnetic and displays a linear  $1/\chi$  vs  $T$  relation, in accordance with equation 1.2. In this regime, applying the appropriate units conversion allows us to write Curie's constant as in equation 1.4 [3]:

$$C = \frac{\mu_o N_A \mu_{eff}^2 \mu_B^2}{3k_B} \quad (1.4)$$

Where  $\mu_o$  is the permeability of free space,  $N_A$  is Avogadro's number,  $\mu_B$  is Bohr magneton,  $k_B$  is Boltzmann's constant and  $\mu_{eff}$  is the effective magnetic moment per ion. Bohr magneton is useful to quantify the atomic/ionic magnetic moment, since it equals the moment of one electron. Using the above relation, together with equation 1.2, the effective moment  $\mu_{eff}$  can be estimated from the  $1/\chi$  vs  $T$  plot.

As mentioned before, the magnetic order pattern depends on the values of the exchange integral  $J$ . Complicated magnetic structures can arise from different exchange constants between different pairs of spins. This will be discussed in more details in section 1.1.4.

### 1.1.3 NANOMAGNETS: SUPERPARAMAGNETISM

A system whose dimensions fall in the order of nanometers is characterized by a high surface-to-volume ratio. It is due to this, added to quantum confinement effects, that the observable properties of nanostructures of some materials are different to their bulk properties. In addition to nanoparticles drawing attention because of their optical properties and their use as catalysts in chemical reactions, owing to their large surface area [5], their magnetic properties are also remarkable. When materials known to be ferro- or ferri-magnetic in bulk are prepared in the form of nanoparticles whose volume is smaller than a certain threshold (figure 1.4), they exhibit a set of properties known as superparamagnetism [6].

We discussed above how a bulk specimen of a ferromagnetic materials develops magnetic domains separated by domain walls. Dissimilarly, each magnetically ordered nanoparticle constitutes one single domain. Due to crystal anisotropy, there will be in general a preferred direction –inside each particle- along which magnetization aligns. The ionic spins perform a  $180^\circ$  flip along this direction as a result of thermal relaxations, with the average time between flips given by equation 1.5 [7, 8]:

$$\tau = \tau_o \exp\left(\frac{KV}{k_B T}\right) \quad (1.5)$$

Where  $\tau_o$  is a characteristic relaxation time, and is usually in the order of  $10^{-10}$  sec [7]. It is perceived from the above equation that  $\tau$  depends on the temperature, the volume of the particle as well as the anisotropy constant  $K$ . Also, the equation bears exponential dependence on the ratio between two types of energies: The anisotropic energy barrier  $KV$ , and the thermal energy  $k_B T$ .

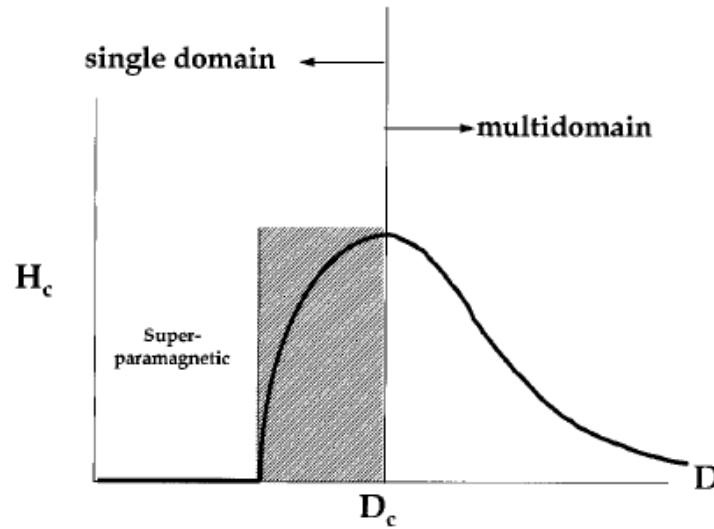


Figure 1.4: Qualitative relation between coercivity and particle size [6].

For all practical purposes, a measured sample will consist of an astronomical number of particles whose sizes express a statistical distribution around some mean value. Since the orientation of particles' moments is described by an *average* relaxation time, comparing the time of measurement to  $\tau$  will be crucial in determining the state of the system. It is important to keep in mind that a particle's relaxation time depends on its size. When the temperature is low, the average time between moment flips will be much larger than the measurement time, and the system will be in a *blocked* state. On the other hand, at higher temperatures, the moments will have enough time to show several flips within the measurement time, leading to an average

magnetization value of zero in the absence of external magnetic field. Such argument enables us to define a Blocking Temperature  $T_B$ , below which the system is blocked. Such temperature is marked by wide peak in the zero field cooled – field cooled (abbreviated ZFC-FC) magnetization curve of the superparamagnetic sample (figure 1.5). The width of the  $T_B$  peak originates from the size distribution of magnetic nanoparticles in a given system. A detailed explanation of how such curve is obtained can be found in the literature [7, 9].

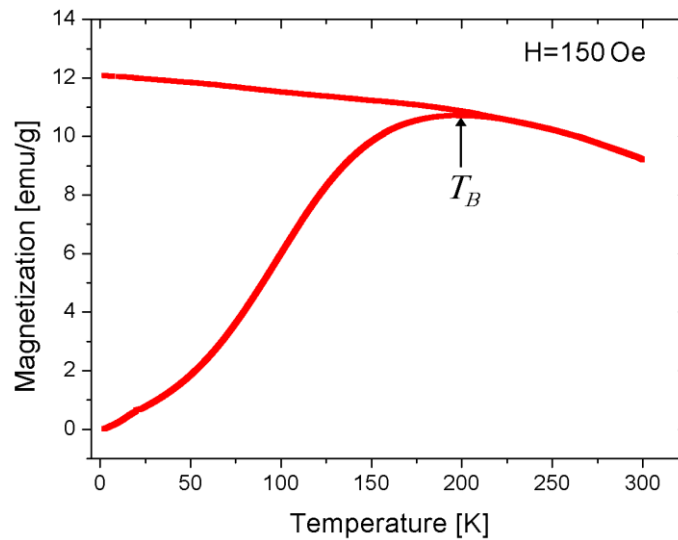


Figure 1.5: ZFC-FC curves obtained for Fe<sub>3</sub>O<sub>4</sub> nanoparticles [10].

Another interesting observation feature in superparamagnetic systems is the non-zero coercivity below the  $T_B$ . This happens because the thermal energy is too low to overcome the crystalline anisotropy energy. Therefore, the particles' magnetic moments tend to rotate back to their easy directions, resulting in non-zero magnetization at zero magnetic field. On the other hand, above  $T_B$  the moments are randomized due to high thermal energy, resulting in zero coercivity (figure 1.6) [10].

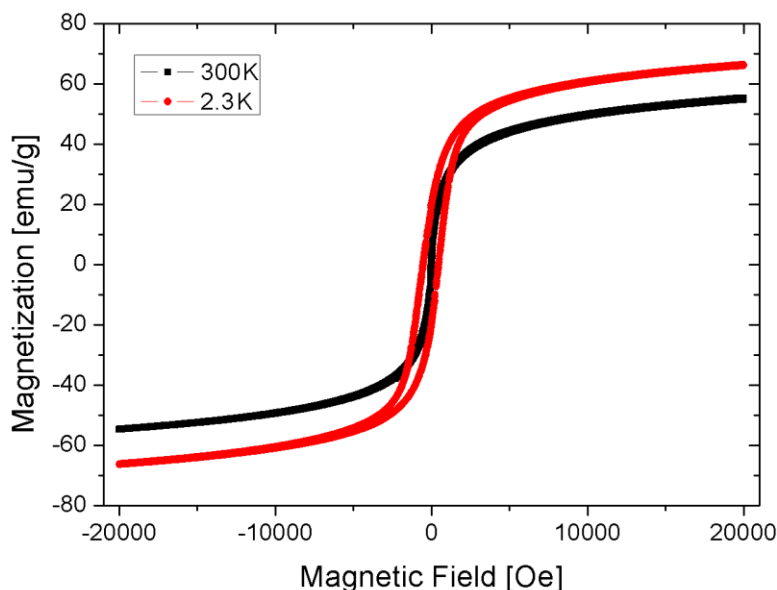


Figure 1.6: M-H curves for  $\text{Fe}_3\text{O}_4$  nanoparticles above and below the blocking temperature (200 K, refer to figure 1.5) [10].

Several applications aim to utilize magnetic nanoparticles for their unusual properties. For instance, they can be utilized in cancer treatment through magnetic hyperthermia [11, 12], in waste water treatment [13], chemical catalysis [14] and information storage [15].

#### 1.1.4 EXOTIC MAGNETIC ORDERING: SPIRAL AND HELICAL MAGNETS

It was noted earlier that complex magnetic ordering patterns could be a result of competing two or more exchange integral values. The outcome in many cases is a non-collinear antiferromagnetic order. Examples on the resulting spin patterns are spiral, triangular and helical orders (Fig 1.7(a)). For instance,  $\text{Ni}^{+2}$  ions in  $\text{Ni}_3\text{V}_2\text{O}_8$  develops a spiral spin structure (Fig 1.7(b)) due to  $J$  for nearest neighbors being different than  $J$  for next nearest neighbors [16].



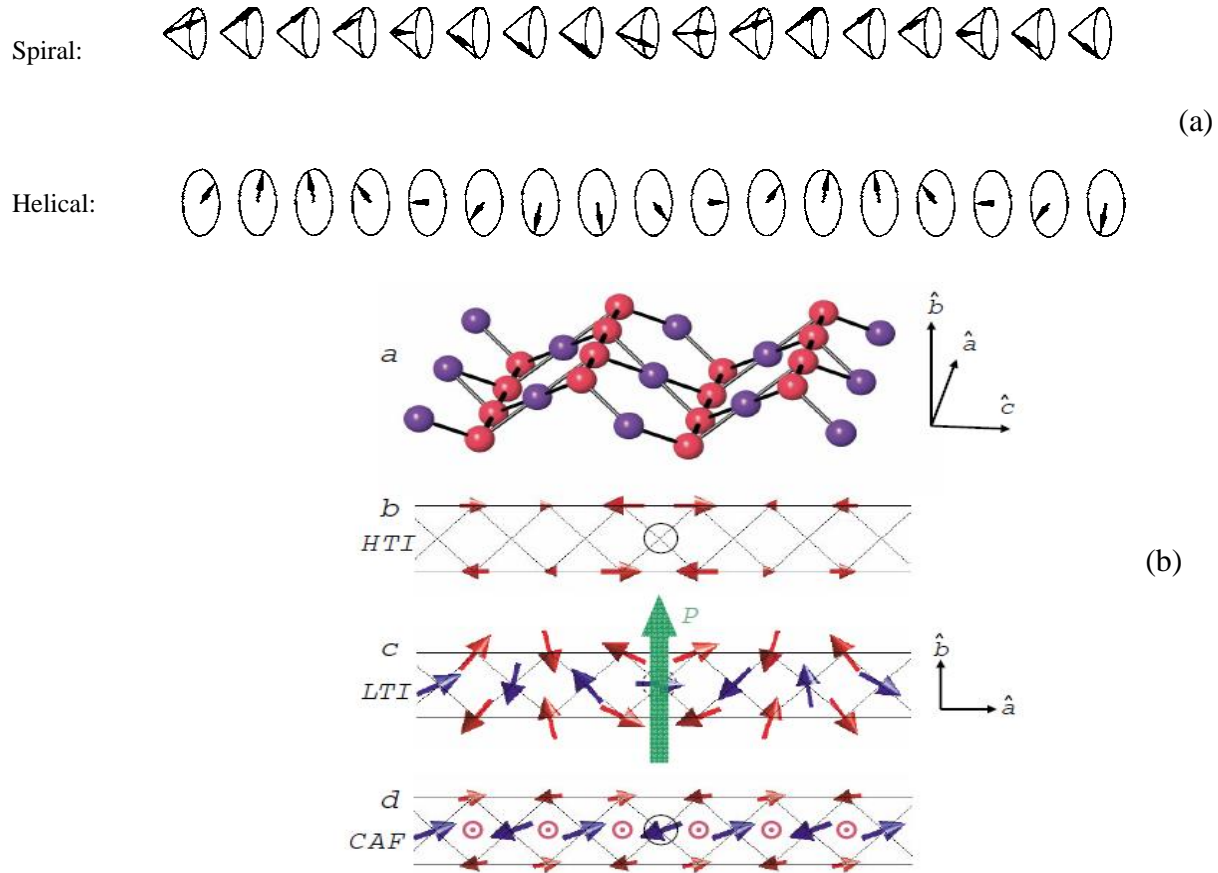


Figure 1.7: (a) Schematic representation of spiral and helical ordering patterns [3] and (b) Spin arrangement of  $\text{Ni}^{+2}$  ions in  $\text{Ni}_3\text{V}_2\text{O}_8$ . The red and blue spheres are Nickel ions at two different crystallographic locations. Coupling between two ‘red’ Nickel ions is different than coupling between ‘red’ and ‘blue’ ones [16].

Some sort of periodicity can be easily noticed in the above spin arrangement patterns. A spin wave vector can be associated with this periodicity. If the spin wave vector is represented as a rational multiple of one of the lattice vectors, the magnetic structure is called to be *commensurate*. A nonlinear magnetic pattern is *incommensurate* in general.

The spiral and helical spin orders are of particular importance because it has been shown recently that they could result in the development of a spontaneous ferroelectric polarization moment [17]. This finding will be presented in more details along with examples in the coming sections.

## 1.2 MAGNETIC FRUSTRATION

We have seen before how the alignment of adjacent spins is defined by the exchange integral in the Heisenberg Hamiltonian  $J$  (Eq 1.2) being positive or negative. We now consider the case of a set of Ising spins, waiting to be accommodated on a planar triangular lattice. Unlike Heisenberg spins, which are free to assume any direction in the crystal lattice, an Ising spin is allowed to point either up or down only, relative to a fixed crystal direction. It can be easily seen from figure 1.8 that for three antiferromagnetically interacting Ising spins occupying the corners of a triangle, a unique ground state (i.e.: minimum interaction energy state) cannot be reached. Once two of the spins are antiparallel to minimize their mutual Hamiltonian, the third spin can no longer find a direction that is satisfactory for both of his two neighbors on the triangle's corners. Considering this argument, one can readily say that antiferromagnetic interactions are not suited well with triangular lattice symmetry. Such situation is known as geometrical frustration [18].

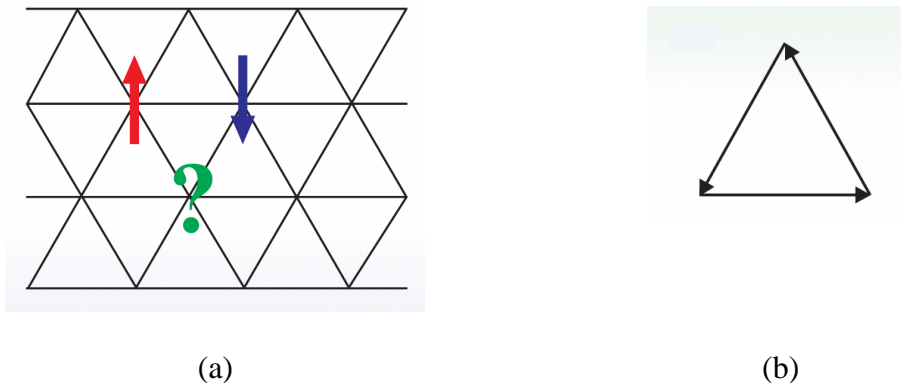


Figure 1.8: (a) Ising spins on a triangular lattice. It is not possible for each spin to be antiparallel with all its neighbors. (b) The ground state of a triangular cluster of Heisenberg spins [18].

Although the argument presented hereinabove evoked Ising spins on triangular lattice, geometrical frustration is not restricted to that case. In real crystals, systems with triangle-based

symmetry and antiferromagnetic interactions often show strong geometrical frustration [19]. In 3-D, triangular lattice translates to face-centered cubic, which can be regarded as edge-sharing tetrahedra. Also, kagome lattice in 3-D is analogous to B-site spinel lattice (Pyrochlore  $Fd\bar{3}m$ ) or a corner-sharing tetrahedra (Figure 1.9).

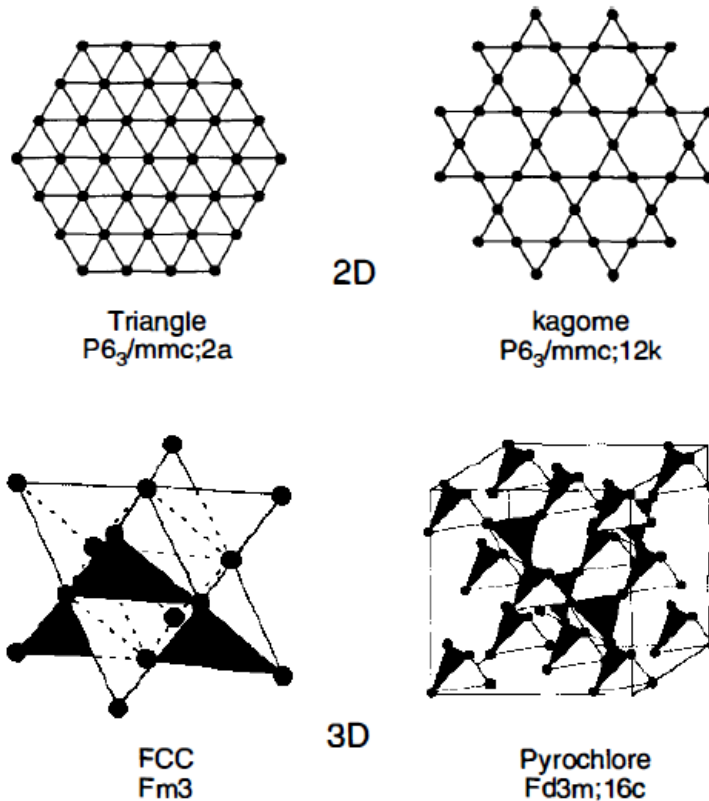


Figure 1.9: 2D (top) and 3D (bottom) frustrated crystal structures [19].

Now, it might seem that it is unfeasible for spins on a triangular based lattice to achieve equilibrium. In reality, a significant number of magnetically ordered systems with ranging degrees of frustration have been identified. This is because real compounds deviate from ideal models for a few reasons [19]:

- 1- Most of the spins found in real life systems are Heisenberg spins, with x- y- and z- components, not simple Ising spins with an up-down configuration.

- 2- The strength of interactions varies throughout a crystal, even among equivalent crystal sites. This is due to crystal impurities and defects. Typically, geometrical frustration gives rise to a degenerate manifold of ground states rather than a single stable ground state configuration [18]. The crystal imperfections give rise to slight perturbations, which results in breaking the degeneracy.

Frustration can be identified experimentally from the inverse magnetic susceptibility ( $1/\chi$ ) vs temperature ( $T$ ) plot. For an antiferromagnetic system, the  $1/\chi$  vs  $T$  behavior could be fit to a straight line above the ordering Neel temperature ( $T_N$ ). The straight line intersection with the x-axis, which is called Curie-Weiss temperature ( $\theta_{CW}$ ), informs us about the nature of interactions in the system under investigation. A positive  $\theta_{CW}$  indicates a ferromagnetic system, while an antiferromagnet is distinguished by a negative  $\theta_{CW}$ . A frustrated antiferromagnet is characterized by a  $\theta_{CW}$  whose absolute value is higher than  $T_N$ . The ratio  $\frac{|\theta_{CW}|}{T_N}$  is empirically defined as the frustration index  $f$  [19].

Care should be taken in estimating the frustration index from  $1/\chi$  vs  $T$  curves. In particular, data should be linear at a high temperature range, in the order of  $\theta_{CW}$ . Also, the effective moment, estimated through Curie's constant (equation 1.4) should correspond to the expected value of the magnetic ion in the studied system.

### 1.3 FERROELECTRICITY

A single atom or molecule would possess an electric dipole moment if the centers of masses of positive and negative charges do not coincide. Such displacement between the opposite charges' centers of masses can arise due to many reasons. For example, such electric dipole moment may arise due to unequal charge ordering on different crystal sites [20], or due to lattice distortions in the crystal structure [21]. The electric dipole moment resulting from such

displacement may be permanent, with the most famous example being the water molecule, or may be temporary, occurring only in the presence of external electric field, giving rise to the dielectric response.

We have discussed previously how a ferromagnetic material develops a non-zero magnetic moment in the absence of external magnetic field. An analogous behavior exists in terms of electric dipole moments. If molecules, or unit cells, have a permanent electric dipole moment, there is a chance for interactions to occur between adjacent moments, leading to long range order among the dipoles. This ferroelectric order generally occurs in domains, each of which having one large electric moment along some direction. Under the influence of external electric field, the sample would show the same hysteresis behavior described before in terms of magnetism, with the discussion referring to electric field and electric dipole moment instead (Figure 1.10).

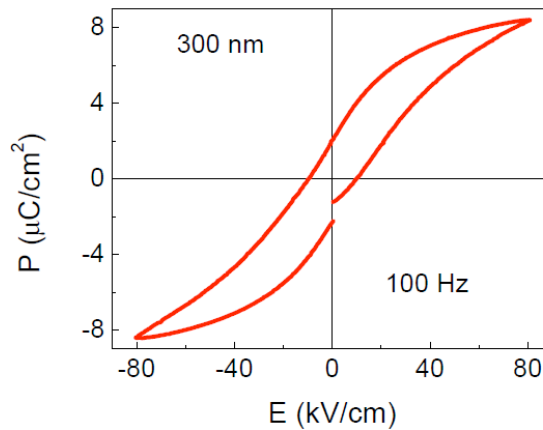


Figure 1.10: P-E hysteresis measured at room temperature for BaTiO<sub>3</sub> 300 nm particles [22].

Ferroelectricity can be quantified in terms of ferroelectric polarization, which is said to be the order parameter associated with ferroelectric ordering (the order parameter describing ferromagnetism is the magnetic moment). The development of an order parameter is

accompanied by a symmetry breaking. Ferroelectric ordering is accompanied by a break in space reversal symmetry, while ferromagnetic ordering invokes time reversal symmetry breaking [23].

There is a number of ways by which such permanent ferroelectric moment arises. For examples, the most widely studied ferroelectric materials are those called ‘Perovskites’. Perovskite is a name given to materials having a crystal structure  $ABO_3$ , with A and B representing cations. This class of materials was named after Calcium Titanate ( $CaTiO_3$ ). The ideal perovskite structure is face centered cubic with the anions at the face centers. Cation B is surrounded by an octahedron of anions, and cation A is surrounded by a cuboctahedron of anions (Figure 1.11). The size of cation A is larger than B, and the relative ion sizes determine whether the structure has an ideal cubic symmetry, or whether some lattice distortions would take place [24]. As mentioned before, the absence of inversion symmetry center is a necessary (but not sufficient) condition for a spontaneous polarization. Thus, a perfect cubic crystal, which exhibits spatial inversion symmetry, is not expected to be ferroelectric.

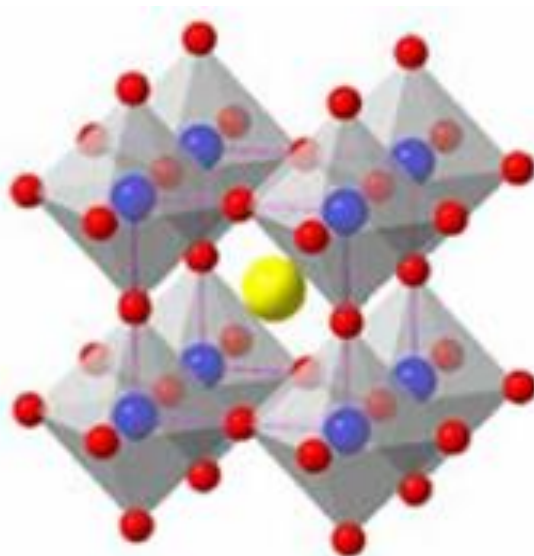


Figure 1.11: Perovskite  $ABO_3$  crystal structure. Yellow and blue spheres depict the locations of A and B ions respectively. The oxygen ions are represented by red spheres (photo courtesy of chem.yale.edu).

The development of ferroelectricity in perovskites can be explained as follows: the local electric field generated due to displacement of  $\text{Ti}^{4+}$  increases much faster than the restoring elastic force, leading to a permanent distortion. This process is known as ‘polarization catastrophe’. The spontaneous polarization of  $\text{BaTiO}_3$  at room temperature is about  $1500 \text{ C/cm}^2$ , and Curie’s temperature is  $120 \text{ }^\circ\text{C}$  [25, 26].

In the perovskite structure, if the B ion is magnetic, there is a possibility of multiferroic order in the perovskite systems, with the ferroelectric and magnetic properties arising from the different cations.  $\text{BiFeO}_3$  is an example of such a system [27, 28]. Multiferroic ordering is the topic of the coming section.

## 1.4 MULTIFERROICS

The word ‘ferromagnetic’ was historically coined to refer to the long range magnetic order developing in magnetic iron oxide. Since then, the prefix ‘*ferro*’ has been used to describe other types of observable ordering. In addition to ferromagnetism and ferroelectricity, two other types of ordering have been identified, namely ferroelasticity, where a material retains spontaneous strain in the absence of external stress [29], and ferrotoroidicity, which refers to the formation of magnetic vortices [30]. Restrictions on time and space symmetry apply for each of these orders, such restrictions are summarized in figure 1.12.

A material showing two or more ferroic orders simultaneously is called multiferroic [31]. Needless to say, such class of materials is the subject of considerable research, not only for the promising applications, but also for the rich and fascinating physics concepts behind such ordering. Materials which are simultaneously ferroelectric and ferromagnetic are of specific importance due to potential applications as -for example- multiple state memory elements where data can be stored in both electric and magnetic orders. Also, by providing the ability to

simultaneously utilize their magnetic and electric polarizations, they provide an extra degree of freedom in device design [32, 33]. Moreover, systems showing concurrent ferroelectric and ferromagnetic orders are called magnetoelectrics if magnetic (electric) order can be controlled by applying electric (magnetic) field. It should be emphasized, however, that a magnetoelectric system needn't be multiferroic. An example of the latter case is  $\text{Cr}_2\text{O}_3$  [34].


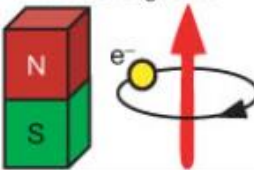
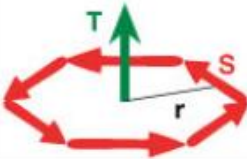
Time \ Space	Invariant	Change
	Invariant	Ferroelastic 
Change	Ferromagnetic 	Ferrotoroidic 

Figure 1.12: Space and time symmetry restrictions on different ferroic orders [30].

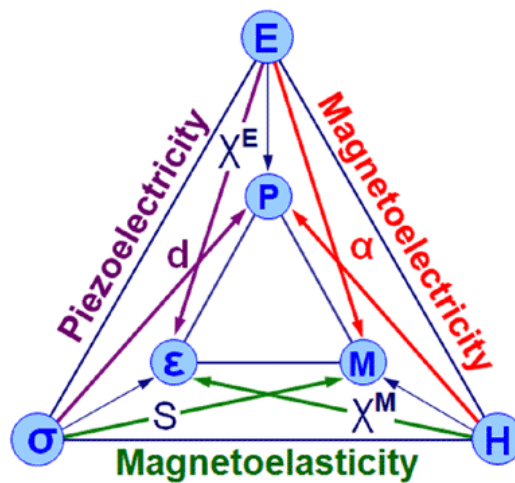


Figure 1.13: Schematic representation of different multiferroic classes, with the corresponding order parameters and coupling coefficients [35].



Since the study of ferroelastic and ferrotoroidic systems is beyond the scope of this thesis, the term ‘multiferroic’ will be used in reference to systems exhibiting simultaneous ferroelectricity and ferromagnetism.

#### 1.4.1 TYPES OF FERROELECTRIC ORDERING IN MULTIFERROICS

We discussed earlier the mechanism responsible for ferroelectricity in perovskites. Such mechanism is important mainly for pedagogical purposes and is not unique. On the other hand, a number of different procedures have been identified as to cause ferroelectric ordering in multiferroic materials. In some cases, the factors developing ferroelectricity are unrelated to the magnetic ordering in the system, which results in a generally weak magnetoelectric coupling. Such systems with independent magnetic and electric orders are called type I multiferroics. On the contrary, the class of type II multiferroics includes systems where the magnetic order parameter provides the break in space reversal symmetry needed to create electric ordering [20]. In this section we present various mechanisms for ferroelectricity in multiferroics:

- Lone pair activity: A lone pair of electrons is defined as a pair of valence electrons that is not shared with other atoms in the chemical formula [36]. It has been shown that such pair is sometimes stereochemically active and produces the needed structural distortion to create ferroelectricity. For example, the origin of ferroelectric order in  $\text{BiMnO}_3$  is shown to be the Bi ion  $6s^2$  lone pair of electrons [37, 38]. Other compounds where electrons lone pair prompt ferroelectricity include  $\text{Bi}_2\text{WO}_6$  [39],  $\text{CsPbF}_3$  [40], and  $\text{BiFeO}_3$  [41]. It should be noted that for all these compounds, the ferroelectric order is triggered by the non-magnetic ion. Therefore, lone pair ferroelectricity is observed in type I multiferroics.
- Charge ordering: The process of charge ordering can be explained with the help of figure 1.14 [42]. The figure depicts a 1-dimensional chain of ‘sites’; where sites can be atoms,

ions or molecules. In (A), the sites are neutral and separated by equal distances. In (B), alternate positive and negative charges build on the sites, creating equal and opposite electric dipole moments. This situation is referred to as ‘Site-Centered Charge ordering’. Since space inversion symmetry is maintained, the state in picture (B) does not have a net dipole moment. In figure 1.14(C), certain distortion causes sites dimerization, resulting in alternating strong and weak bonds. This situation is referred to as ‘Bond-Centered Charge ordering’, and space inversion symmetry is still conserved. In (D) it is shown that a combination of Site-Centered and Bond-Centered charge ordering states annihilates inversion symmetry, hence giving rise to a net dipole moment.

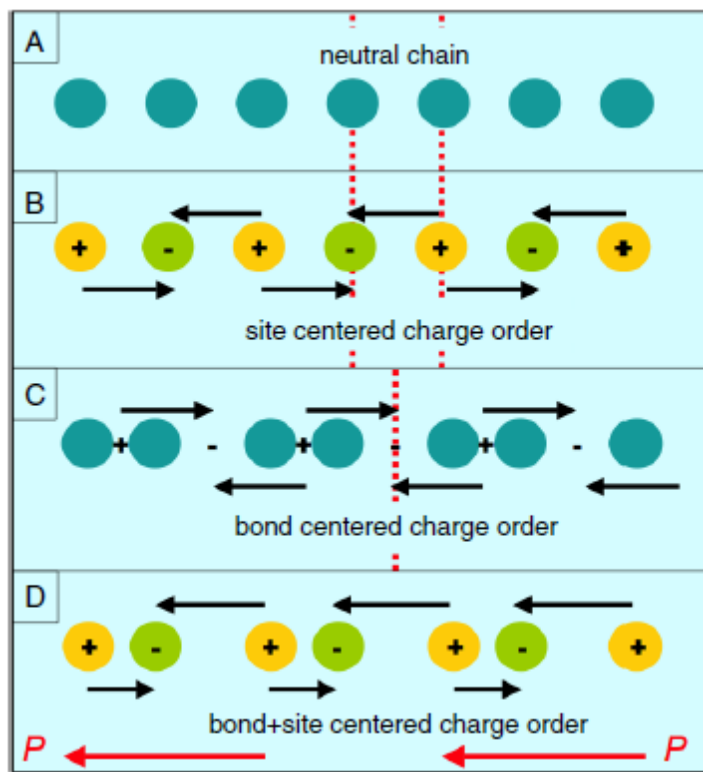


Figure 1.14: Development of ferroelectric order via charge ordering [42].

Charge ordered ferroelectricity is observed in type I multiferroics, such as  $\text{Fe}_3\text{O}_4$  [43] and  $\text{LuFe}_2\text{O}_4$  [44]. It has been also noted in some type II multiferroics, like  $\text{TbMn}_2\text{O}_5$  [45] and  $\text{Ca}_3\text{Co}_{1.04}\text{Mn}_{0.96}\text{O}_6$  [46].

- Geometrical distortions: Ferroelectric order driven by structural geometric distortions has been observed in  $\text{YMnO}_3$  [47]. In this system,  $\text{Mn}^{3+}\text{O}_5$  polyhedra would tilt in such a way that forces imbalanced Y ions distribution, with respect to a fixed crystal plane. Such distortion induces ferroelectric moment along the  $c$ -axis.
- Spin-Orbit interactions: Another ferroelectricity inducing mechanism that is observed in type II multiferroics is called Dzyaloshinskii-Moriya interaction [48, 49]. This is a three-fold antisymmetric exchange interaction, which takes place between two magnetically ordered spins via a close-by ligand, leading to spin canting (Figure 1.15). It can be written as:

$$H_{DM} = \vec{D}_{ij} \cdot (\vec{S}_i \times \vec{S}_j) \quad (1.6)$$

Where the direction of  $\vec{D}_{ij}$  is determined by  $\vec{D}_{ij} \propto \vec{r}_{ij} \times \vec{x}$ .

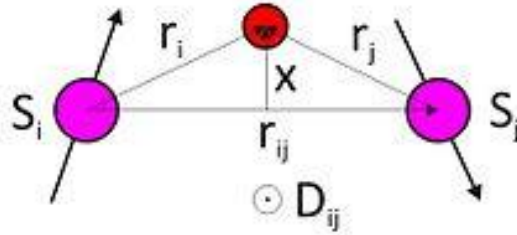


Figure 1.15: Vector diagram representation of Dzyaloshinskii-Moriya interaction (Courtesy of Wikipedia.org).

Besides inducing spiral magnetic ordering, such distortions, in some cases, lead to small shifts in the ligand ions, which in turn break charge distribution symmetry [50]. Since symmetry breaking here is induced by magnetic ordering, strong magnetoelectric

coupling is anticipated. Multiferroicity in  $\text{FeVO}_4$  [51] and  $\text{RMnO}_3$  (where  $\text{R}=\text{Gd, Tb, Dy}$ ) is attributed to Dzyaloshinskii-Moriya interaction [52]. This effect can also be described in terms of the spin current, describing the precession of spins [50].

#### **1.4.2 SCARCITY OF MULTIFERROICS**

As mentioned before, multiferroic materials are potential candidates for a wide range of applications. Therefore, one aspect of ongoing research on multiferroics aims to discover and synthesize more multiferroic systems. While it is not uncommon to observe one kind of ferroic ordering in novel systems, multiferroicity is a relatively rare phenomenon. The reasons behind this observation are examined in Ref [32]. Specifically, the article digs into the cause behind the rarity of mutual occurrence of ferroelectricity and ferromagnetism, where a number of aspects are examined for being responsible for such observation, like crystal symmetry, electric properties and  $d$ -shell occupancy. The article concludes that while the presence of unpaired electrons is essential to generate localized magnetic moments, it eliminates the tendency for a distortion that removes the center of symmetry. Furthermore, by examining a number of systems, it seems that Jahn-Teller distortions (Figure 1.16) are particularly unfavorable for magnetic ions in systems showing ferroelectricity.

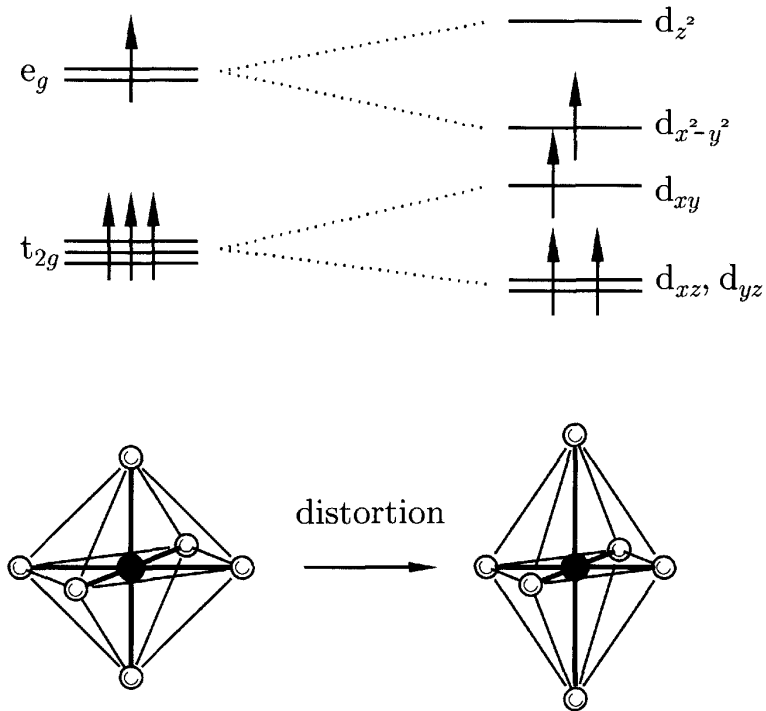


Figure 1.16: Spontaneous distortion of the oxygen ions octahedron surrounding an  $\text{Mn}^{3+}$  ion as an example on Jahn-Teller effect [3]. Such distortion is sometimes favored because the energy cost of increased elastic energy is balanced by a resultant electronic energy saving.

## 1.5 HEXAFERRITES

The term ‘hexa-ferrites’ refer to iron-based magnetic oxides with hexagonal crystal structure. The main constituents are iron and oxygen, along with other cations, which make up three distinct building blocks. The variation of the stacking sequences of these building blocks allows for defining six types of hexagonal ferrites [53]. Besides their use as permanent magnets, common applications of hexaferrites include magnetic recording and data storage materials, and as components in electrical devices, particularly those operating at microwave/GHz frequencies [54].

Hexaferrites are also important because of the non-collinear nature of their magnetic order, which attracts research interests for potential magneto-electric properties. Recently, a

hexagonal ferrite of M-type was reported to show room temperature electric field-controlled magnetization [55]. The M-type class also includes barium hexaferrite ( $\text{BaFe}_{12}\text{O}_{19}$ ), which possesses a room temperature magnetic saturation moment of about 60 emu/g and a Curie point of  $\sim 450$  °C in powder form [56]. However, it was mentioned that in spite of having a conical spin state, its low resistivity prevents the observation of room temperature magnetoelectric behavior [53]. Some work on barium hexaferrite-polymer hybrid films will be presented in Chapter 4.

## 1.6 HYBRID MULTIFERROICS

In general, magnetoelectric coupling is experimentally found to be a weak effect in single phase systems, a problem which hinders its employment for technological applications. Therefore, considerable research efforts are devoted towards coming up with ways to enhance it. One way to work around this problem is to design hybrid systems in which magnetoelectricity is induced via strain [57]. The main concept in designing such system is to use electric (magnetic) field to induce strain in the ferroelectric (ferromagnetic) component of the composite, and the strain passes on to the other component through the interface [58]. By following this strategy, coupling coefficients which exceed those of single phase systems by up to 5 orders of magnitude have been achieved [59]. However, by considering the change in the free energy of the magnetoelectric medium upon applying electric or magnetic fields, it was shown that for the system to be thermodynamically stable, the magnetoelectric response coefficient ( $\alpha$ ) is bounded by the product of the electric permittivity ( $\chi^e$ ) and magnetic permeability ( $\chi^m$ ) of the medium [60]:

$$\alpha_{ij} \leq (\chi_{ii}^e \chi_{jj}^m)^{\frac{1}{2}} \quad (1.7)$$

The quantities in equation (1.7) are tensors in general, with the subscripts  $i$  and  $j$  denoting the tensor indices.

A variety of composite systems have been prepared and studied for magnetoelectric coupling, including eutectic mixtures [61], nanocomposites [62-64] and laminated structures [65-67]. Possible applications considered are optical waves amplitude and polarization modulators, data storage and AC/DC magnetic field detectors [59].

In chapter 4 of this thesis, some work on polyvinylidene fluoride (PVDF) based magnetoelectric composites will be presented. In particular, the effect of loading self-standing PVDF films with magnetite nanoparticles, along with different nanofillers, will be considered. We also investigate the magneto-dielectric properties of PVDF-Nickel and PVDF-Barium Hexaferrite nanocomposites.

## **1.7 SCOPE OF THE THESIS**

With the increasing demand on cheaper and better performance multifunctional materials for different applications, it is becoming more crucial to have a better understanding of the physics needed to tailor more devices and materials to fit better in every day's technological needs. In a tiny effort for this cause, we explore the multiferroic and magnetoelectric properties of a few single phase and multiphase systems in this thesis.

In chapter 1, we study  $\text{FeVO}_4$  as an example on low symmetry multiferroics. We focus on the anisotropy in those crystals in an attempt to nail the origin of the ferroelectric and magnetoelectric behaviors. For the same purpose, we also study doped single crystals of  $\text{FeVO}_4$ .

Our focus in chapter 2 is Gd-doped  $\text{Fe}_3\text{O}_4$  nanoparticles, where we study the effect of doping on the ferroelectric polarization moment and on the ferroelectric relaxation mechanism. We also investigate the structural and dielectric changes accompanying Verwey transition.

Finally, we present the magnetoelectric properties of a number of PVDF-based composite and self-standing films in chapter 3. The effect of using different magnetic and non-magnetic nanofillers on PVDF piezoelectricity is researched.



## CHAPTER 2: FERROELECTRIC AND MAGNETIC ANISOTROPY IN IRON VANADATE ( $\text{FeVO}_4$ ) SINGLE CRYSTALS

### 2.1 BACKGROUND AND PREVIOUS WORK

The two types of single phase multiferroic materials have been described in Chapter 1; type I and type II. Type II materials are characterized by the origin ferroelectric ordering associated with a magnetic structural transition. While this class of multiferroics is characterized by strong magnetoelectric coupling, it is also marked by low ordering temperatures, usually accessible only via cryogenic cooling. As a result, type II materials have not been considered for practical applications.

In order to develop a functional multiferroic material one needs to understand the physics behind ferroic ordering and the factors triggering strong magnetoelectric coupling. One way this can be done is by carrying out first principle calculations on a given multiferroic system, given its unit cell parameters, to predict its observable quantities, such as its ferroelectric polarization moment.

$\text{FeVO}_4$  provides a good example for type II multiferroics. With a  $P\bar{1}$  triclinic crystal structure [68, 69], the only symmetry element of the point group is the inversion symmetry. Furthermore, this symmetry should be broken once the ferroelectric order develops, giving rise to a polar phase with no symmetry constraints on the direction of polarization. As such,  $\text{FeVO}_4$  is an ideal system for testing the results of first principle calculations [69].

The first attempt to determine the crystal structure of  $\text{FeVO}_4$  was carried out by Levinson *et al.* [70] using X-ray diffraction data on single crystals grown from molten flux. The lattice parameters were then confirmed and refined by Robertson *et al.* [71]. The obtained lattice parameters of the triclinic  $P\bar{1}$  space group are listed in table 2.1. It was also reported in [71] that

the system hosts  $\text{Fe}^{3+}$  ions at three symmetry inequivalent sites: two  $\text{Fe}^{3+}$  ions are surrounded by six  $\text{O}^{2-}$  ions each in a distorted octahedral environment, while the third  $\text{Fe}^{3+}$  is surrounded by five  $\text{O}^{2-}$  ions in a distorted trigonal bipyramidal environment (figure 2.1). The  $\text{V}^{5+}$  ions, on the other hand, are surrounded by four  $\text{O}^{2-}$  ions constructing distorted tetrahedrons. The structural distortions arise mainly due to Coulomb repulsion between iron ions.

Lattice parameter	Value	Lattice parameter	Value
$a$	6.719(7) Å	$\alpha$	96.65(8) $^\circ$
$b$	8.060(9) Å	$\beta$	106.57(8) $^\circ$
$c$	9.254(9) Å	$\gamma$	101.60(8) $^\circ$

Table 2.1: Measured lattice parameters of  $\text{FeVO}_4$  as given in [71]. The figure in parenthesis gives the uncertainty in the last digit.

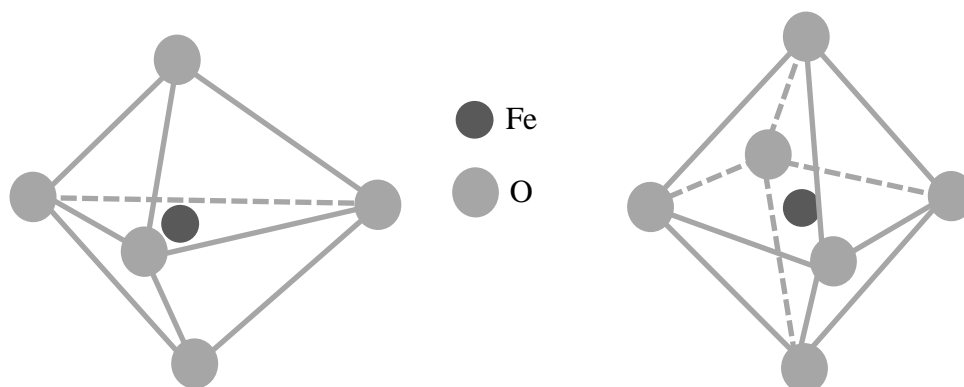


Figure 2.1: Trigonal bipyramidal (left) and octahedral (right) environments of iron in  $\text{FeVO}_4$ .

Each three  $\text{Fe}^{3+}$  occupying nonequivalent sites form an *S*-shaped cluster (figure 2.2). Another way to visualize it is to regard every six  $\text{Fe}^{3+}$  ions as formed out of two identical  $\text{Fe}_3\text{O}_{13}$  monomers, related with a center of inversion [72]. The *S*-shaped clusters themselves are joined together by the  $\text{VO}_4$  tetrahedra (figure 2.3).

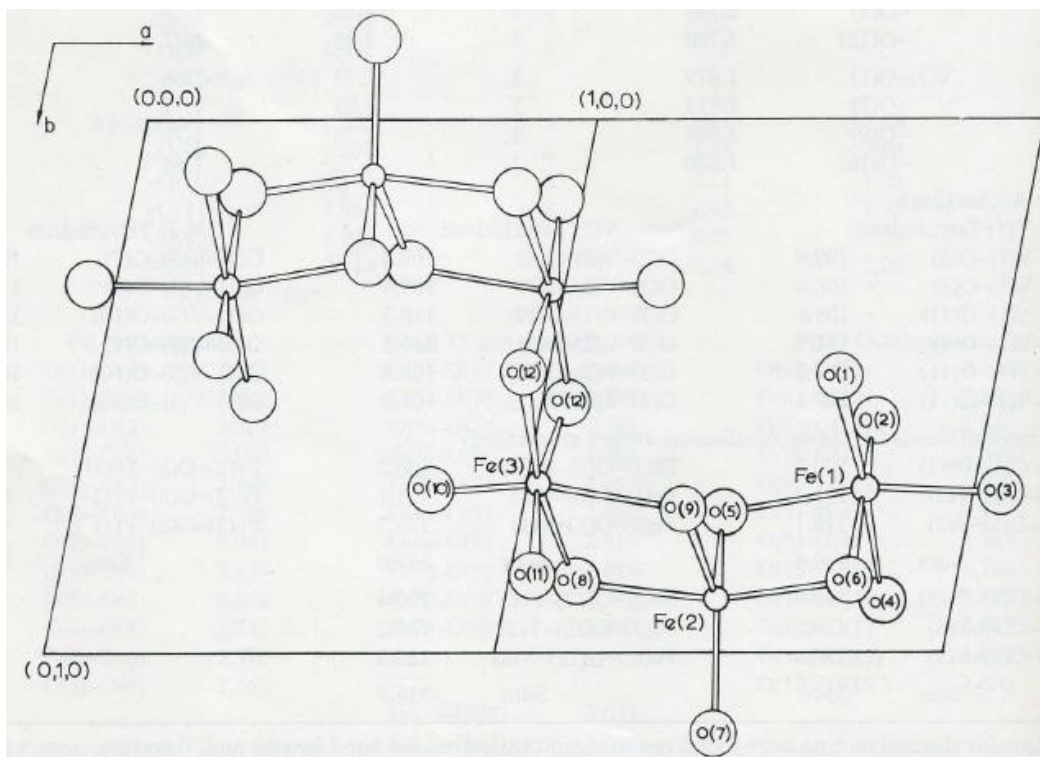


Figure 2.2: Two *S*-shaped clusters of iron ions (small circles), projected on the *a-b* plane. The Fe-O bonds are represented by solid lines, and oxygen ions are represented by the large spheres [71].

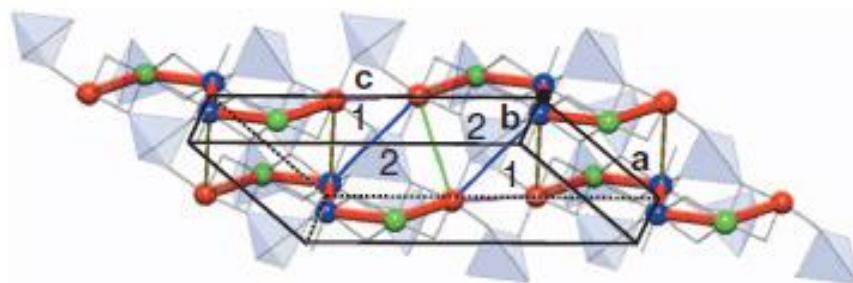


Figure 2.3: The three symmetrically inequivalent  $\text{Fe}^{3+}$  sites (represented by colored solid spheres) connected by  $\text{VO}_4$  tetrahedra (pale blue) [72]. It is important to note that the choice of lattice parameters here is different than those in figure 2.2.

A careful look at figures 2.2 and 2.3 reveals that the local environments of  $\text{Fe}^{3+}$  and  $\text{V}^{5+}$  ions consists of edge-sharing polyhedra, which makes  $\text{FeVO}_4$  prone to geometrical frustration [73, 74].

The magnetic properties of FeVO<sub>4</sub> have been reported in a number of articles [68, 72, 75-78]. It is well established that FeVO<sub>4</sub> is paramagnetic above 22 K, and develops collinear antiferromagnetic ordering between 22 K and 15 K. Below 15 K, the magnetic structure is non-collinear antiferromagnetic. In both cases, the magnetic order parameter is incommensurate with the crystal lattice parameters.

There are two different types of magnetic interactions here: *inter*-cluster and *intra*-cluster interactions. The prefix ‘*intra*’ means inside or within. The intra-cluster interactions are between Fe<sup>3+</sup> and Fe<sup>3+</sup> (direct exchange), and Fe<sup>3+</sup>—O—Fe<sup>3+</sup> (super exchange). Both of these interactions are antiferromagnetic, and are represented by the thick red lines in figure 2.3. On the other hand, the inter-cluster interactions are along the Fe<sup>3+</sup>—O—O—Fe<sup>3+</sup> chains, and are portrayed by the thin colored lines in figure 2.3 [72]. The inter- and intra-cluster interactions engage an odd number of Fe<sup>3+</sup> ions in closed loops, making it impossible to satisfy antiferromagnetic collinear arrangements throughout the whole structure, and introducing potential for frustration.

The magnetic structure of FeVO<sub>4</sub> was determined at different temperatures by neutron diffraction, and reported in reference [72]. It is revealed that the magnetic propagation vector  $\bar{k}$  generates an incommensurate magnetic moment that is a function of position inside different unit cells ( $\bar{R}_l$ ), given by:

$$\bar{M}_j(\bar{R}_l) = \bar{A}_j \cos(2\pi\bar{k} \cdot \bar{R}_l + \bar{\varphi}_j) + \bar{B}_j \sin(2\pi\bar{k} \cdot \bar{R}_l + \bar{\varphi}_j) \quad (2.1)$$

Equation 2.1 describes an ellipse with  $\bar{A}_j$  and  $\bar{B}_j$  being the major and minor axes irrespectively. With reference to figure 2.4, it can be seen that the magnetic phase developing between 15 K and 22 K is collinear with  $\bar{B}_j = 0$ , while the phase forming below 15 K is helical. The magnetic structure calculated by neutron diffraction refinement suggests that the two halves

of the  $S$ -shaped clusters referred to before are centrosymmetric with regards to magnetic vector amplitude only, but the phases, on the other hand, do not maintain the same relation.

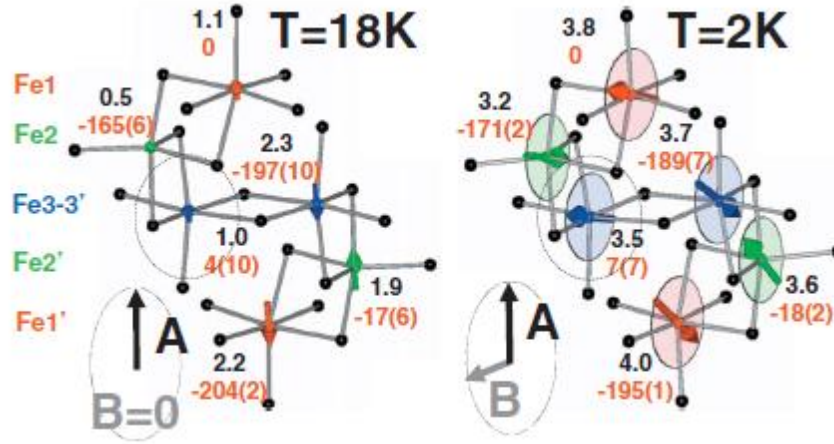


Figure 2.4: Magnetic structure inside the centrosymmetric  $S$ -shaped clusters pair in FeVO<sub>4</sub> [72].

The absence of centrosymmetry in both magnetic phases suggests that the motive for ferroelectricity developing below 15 K is not the break of space inversion symmetry, but rather the transition to a non-collinear magnetic structure.

The connection between non-linear spin structures and ferroelectricity was brought up in chapter 1. It was shown by Katsura *et. al.* [17] that ferroelectric polarization moment does not always necessitate inversion symmetry breaking to arise, but can be the result of non-collinear spin structures. To shed some light on this situation, consider the three atom model shown in figure 2.5, in which two transition metal ions, M1 and M2, are bonded through an Oxygen atom O. The spins at M1 and M2, labeled  $\vec{e}_1$  and  $\vec{e}_2$  respectively, are non-collinear, giving rise to what can be called ‘spin current’  $\vec{j}_s$ . The direction of  $\vec{j}_s$  is obtained by the cross product of the two unit vectors  $\hat{e}_1$  and  $\hat{e}_2$ .

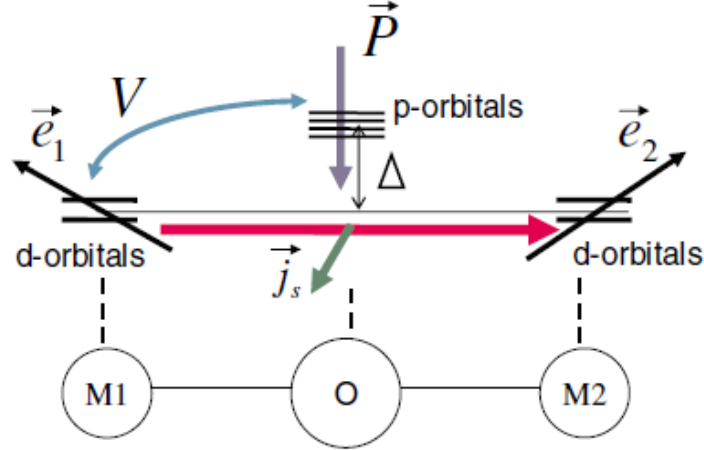


Figure 2.5: A model representing the vector relation between spins  $\vec{e}_1$ ,  $\vec{e}_2$ , the resulting spin current and electric polarization [17].

There is a charge hopping process taking place between the M  $d$ -orbitals and the O  $p$ -orbital, which contributes to the total Hamiltonian of the system. Applying second-order perturbation theory yields the resulting ferroelectric polarization in the form:

$$\vec{P} \sim \left(\frac{e}{V}\right) \hat{e}_{12} \times \vec{j}_s \quad (2.2)$$

Where  $V$  is called the charge transfer integral and  $\hat{e}_{12}$  is the unit vector connecting M1 and M2.

Doped  $\text{FeVO}_4$  samples were also studied to investigate the effect of magnetic and nonmagnetic doping on the multiferroic properties [76, 79]. Magnetic and heat capacity measurements showed the two magnetic transitions to persist for up to 20% doping fraction of Zn, Cr and Mn dopants. Some of the doped samples were also shown to retain ferroelectricity below 15 K.

Motivated by the previous work on type II multiferroics in general, and on  $\text{FeVO}_4$  in particular, the aim of the current work is to investigate the fundamental mechanisms responsible for magnetically induced ferroelectricity in low symmetry multiferroics. Our target is to correlate changes in the ferroelectric polarization vector with modifications in selected spin-charge

coupling mechanisms, produced by chemical substitution, in order to identify the specific interactions responsible for the multiferroic order.

In this chapter, the procedure to prepare  $\text{FeVO}_4$  single crystals is described, followed by a detailed survey of structural and multiferroic characterization, highlighting the anisotropic behavior in  $\text{FeVO}_4$  single crystals. Afterwards, studies on doped  $\text{FeVO}_4$  single crystals are reported.

## **2.2 EXPERIMENTS AND RESULTS**

### **2.2.1 $\text{FeVO}_4$ SINGLE CRYSTALS PREPARATION**

Single crystals of  $\text{FeVO}_4$  were grown from molten flux following the standard procedure described in [68, 70, 71]. The method of growing single crystals from molten flux, known as flux-growth method, will be presented in more details in the appendix of this thesis. The used reagents were iron (II) oxalate dihydrate  $\text{FeC}_2\text{O}_4 \cdot 2\text{H}_2\text{O}$  (CAS# 6047-25-2) and vanadium (V) oxide  $\text{V}_2\text{O}_5$  (CAS# 1314-62-1). The powders were mixed in a molar ratio of 1:1; with the excess  $\text{V}_2\text{O}_5$  to act as a solvent medium. After thorough mixing, the powder was kept in a platinum crucible and covered with a platinum cap (figure 2.6 (a)). The platinum crucible was in turn kept inside a bigger alumina crucible, covered, and heated in a conventional muffle furnace to  $975\text{ }^\circ\text{C}$  at a rate of  $40\text{ }^\circ\text{C}/\text{hour}$ . The mixture was kept at  $975\text{ }^\circ\text{C}$  for 6 hours to achieve a homogenous melt, after which it was cooled to  $650\text{ }^\circ\text{C}$  at a rate of  $8\text{ }^\circ\text{C}/\text{hour}$ . The crucible was then rapidly cooled to room temperature at a rate of  $\sim 5\text{ }^\circ\text{C}/\text{min}$  (figure 2.7).

The obtained crystals were needle-shaped, with  $\sim 1\text{ cm}$  length and a few millimeters cross section (figure 2.6(b,c)). The larger crystals found on the flux surface could be separated mechanically, and the flux was kept under hot dilute nitric acid for several hours to free more crystals.

Dilute nitric acid was used also to clean the platinum crucibles from any residual flux. In the few cases where some of the flux persisted, the crucible was filled with potassium pyrophosphate  $K_4P_2O_7$  (CAS# 7320-34-5) and heated at  $1050\text{ }^\circ\text{C}$  for two hours. The residual flux after this process could be washed with tepid water.

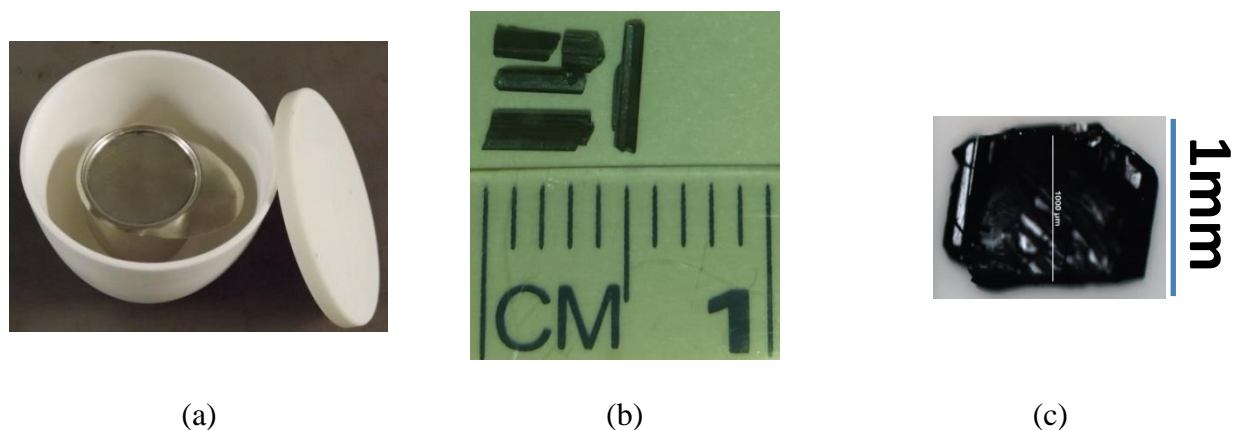


Figure 2.6: (a) The platinum crucible inside the alumina crucible. (b) and (c) A few retrieved single crystals showing their length scale.

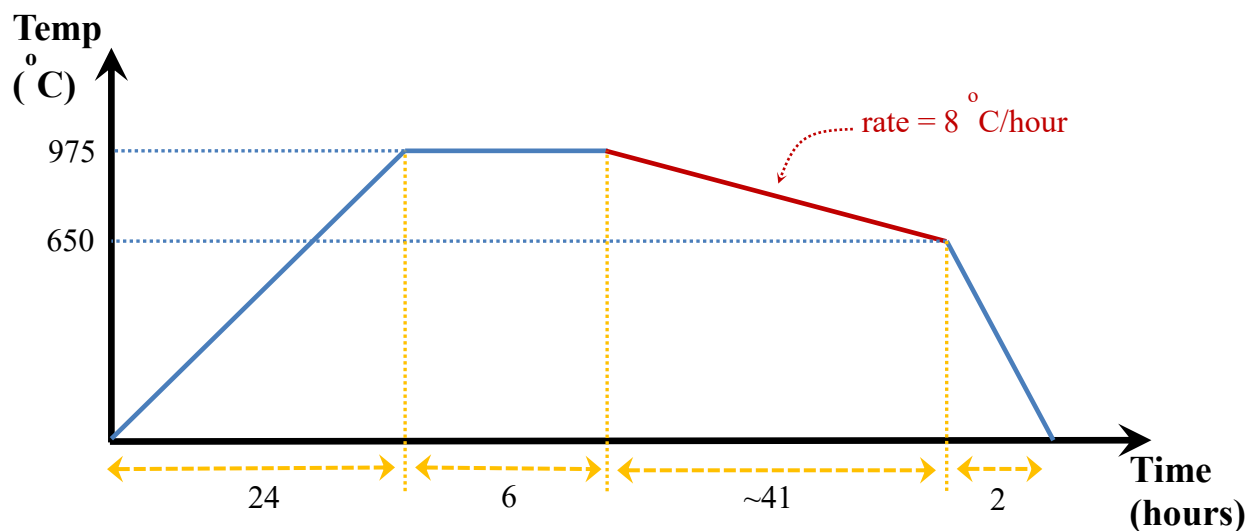


Figure 2.7: Illustration of the annealing process applied to grow  $FeVO_4$  single crystals.



### 2.2.2 STRUCTURAL CHARACTERIZATION

The  $\text{FeVO}_4$  triclinic  $P\bar{1}$  structure was first confirmed by grinding a few washed crystals into powder and getting a powder X-ray diffraction (XRD) spectrum using a Bruker Rigaku Miniflex-600 diffractometer with Cu K- $\alpha$  ( $\lambda = 1.54 \text{ \AA}$ ) X-rays. The obtained peaks were matched with those listed in the standard powder diffraction file (*Joint Committee for Powder Diffraction #38-1372*). The recorded spectrum is shown in figure 2.8(a), where the grey lines at the bottom of the plots represent the standard peak positions. The  $(hkl)$  indices of the highest peaks are also indicated.

Raman spectrum was also recorded on single crystals using a Renishaw inVia Raman microscope spectrometer, utilizing a 785 nm line from a diode laser source and a 50X objective. The resolution of the spectrometer using 1200 grooves per mm grating was  $\sim 3.5 \text{ cm}^{-1}$ . The spectrum recorded for  $\text{FeVO}_4$  single crystals, given in figure 2.8(b), matches earlier reports [77, 80], with the peaks at 958, 887, 824, 728  $\text{cm}^{-1}$  corresponding to symmetric and asymmetric stretching of the V=O bond. The peaks at 361 and 318  $\text{cm}^{-1}$  represent the bending vibrations of the  $(\text{VO}_4)^{3-}$  tetrahedra. Finally, the modes between 136 and 210  $\text{cm}^{-1}$  are due to the presence of bridging V—O—Fe bonds in  $\text{FeVO}_4$  [80].

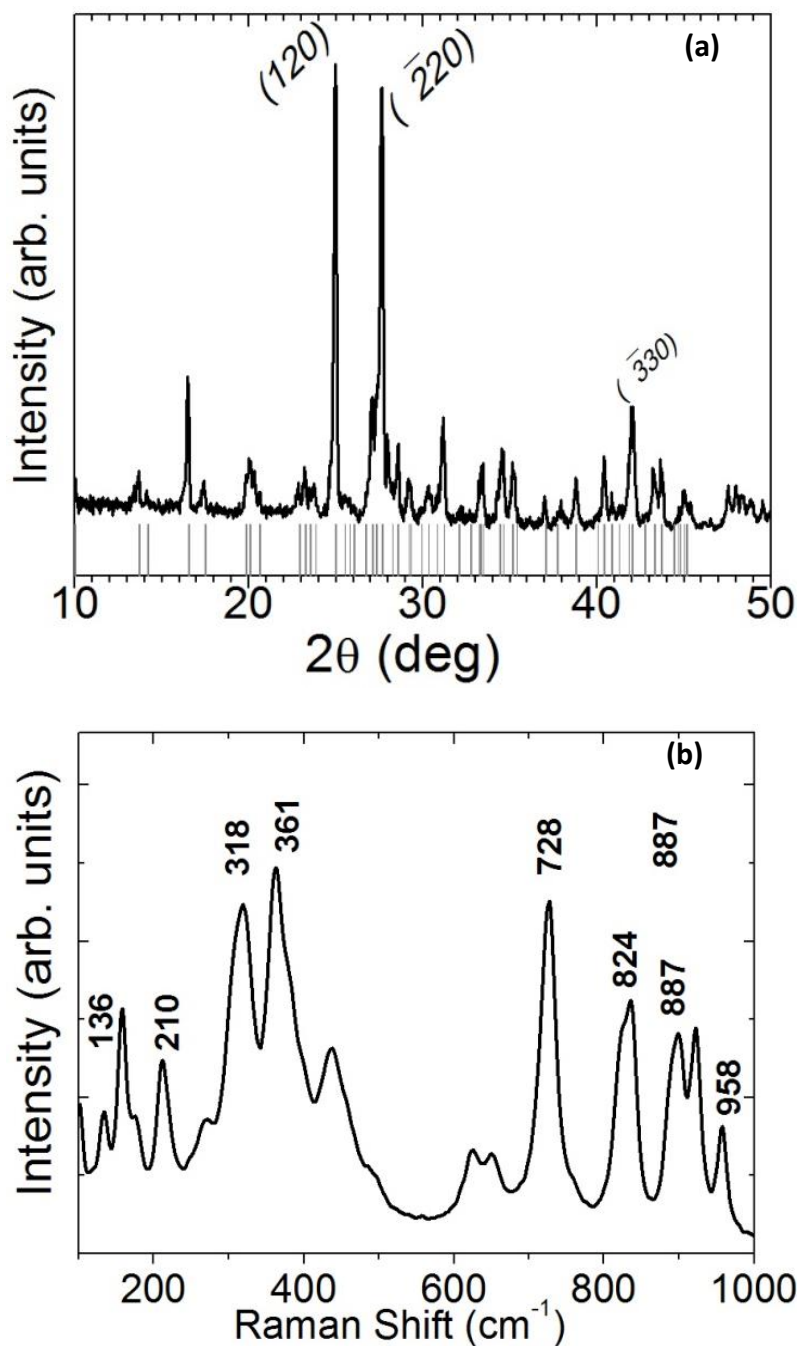


Figure 2.8: (a) Powder XRD diffraction pattern obtained for ground  $\text{FeVO}_4$  single crystals and (b) Raman spectrum for  $\text{FeVO}_4$  single crystals.

The lattice parameters of were estimated by applying Rietveld refinement on its XRD spectrum. Figure 2.9 shows the fitted data plot, and table 2.2 lists the obtained lattice parameters.

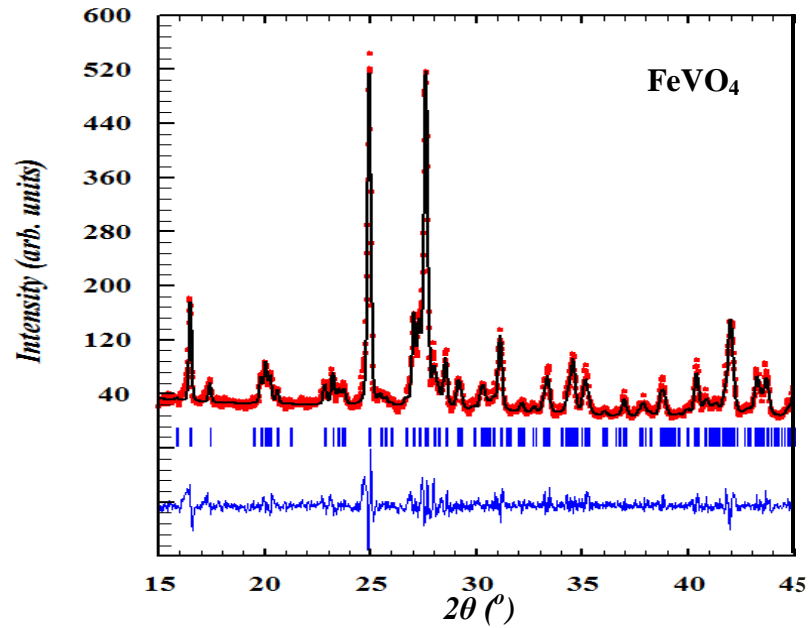


Figure 2.9: Rietveld fitting for the XRD spectrum of the undoped FeVO<sub>4</sub> sample.

To get more insight into the structure, a single crystal XRD Bruker D8 diffractometer was used to measure the lattice parameters. The obtained values (at 100 K) are also included in table 2.2, and are in good agreement with the previously reported values [68, 71]. The long axis of the needle shaped crystals is matched to the crystallographic  $a$ -axis, which also agrees with the previous work by He *et al.* where the same growth routine was used [68].

Lattice parameter	Reported Value	From Single crystals XRD	From Rietveld fitting
$a$	6.719(7) Å	6.7032(3) Å	6.7330(7) Å
$b$	8.060(9) Å	8.0486(4) Å	8.079(1) Å
$c$	9.254(9) Å	9.3301(4) Å	9.3691(9) Å
$\alpha$	96.65(8)°	96.643(2)°	96.566(6)°
$\beta$	106.57(8)°	106.613(2)°	106.644(8)°
$\gamma$	101.60(8)°	101.471(2)°	101.56(1)°

Table 2.2: Lattice parameters of undoped  $\text{FeVO}_4$ , measured by single crystal XRD, estimated using Rietveld fitting and as reported by Robertson *et al.* [71].

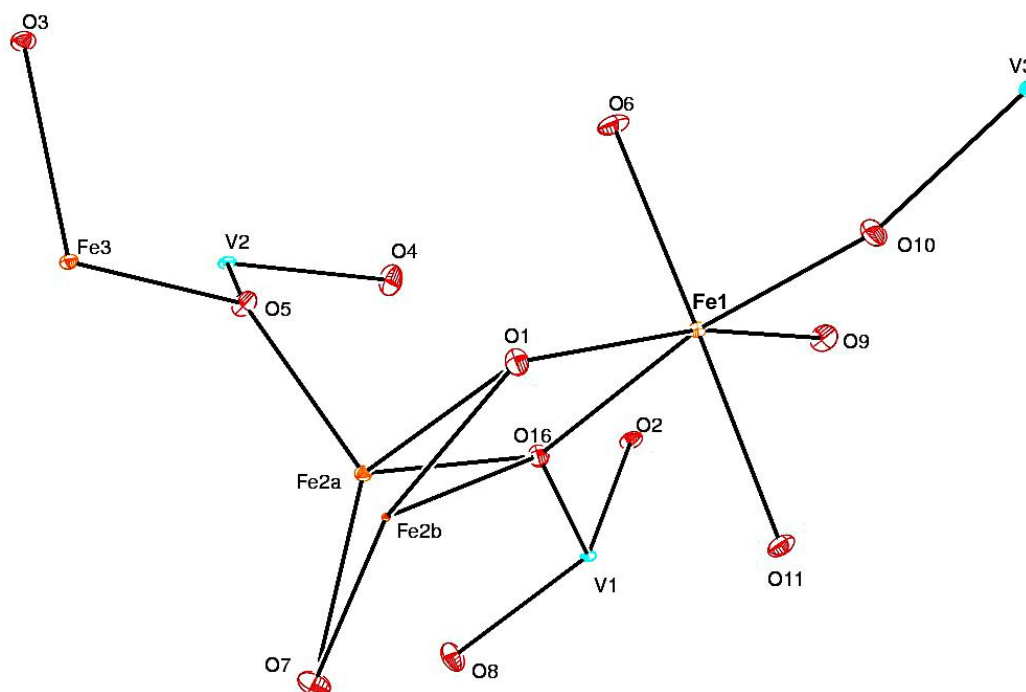


Figure 2.10:  $\text{FeVO}_4$  unit cell, constructed from the single crystal diffractometer data.

### 2.2.3 MAGNETIC MEASUREMENTS

Magnetic measurements were carried out using a Quantum Design Superconducting Quantum Interference Device (SQUID) magnetometer (MPMS-5S). Since the mass of individual crystals is small ( $\sim 4$  mg at most), the absolute magnetic moment of each crystal would be insufficient to obtain accurate results. To work around this problem, several crystals are arranged in parallel with the help of an optical microscope, and attached to a piece of cardboard with GE Varnish (GE-7031). The cardboard could be oriented to set the crystals' long axis perpendicular and parallel to the applied magnetic field. Measurements of magnetic moment versus temperature confirm the antiferromagnetic nature of the formed crystals (figure 2.11), with the AFM transition showing at  $\sim 21.5$  K, both along  $a$  ( $H \parallel a$ ) and perpendicular to  $a$  ( $H \perp a$ ). However, the non collinear AFM transition manifests itself in magnetic data only when the applied field is directed perpendicular to  $a$ , in agreement with the data reported earlier by Daoud-Aladine *et al.* [72], signifying  $a$  as an easy magnetic axis.

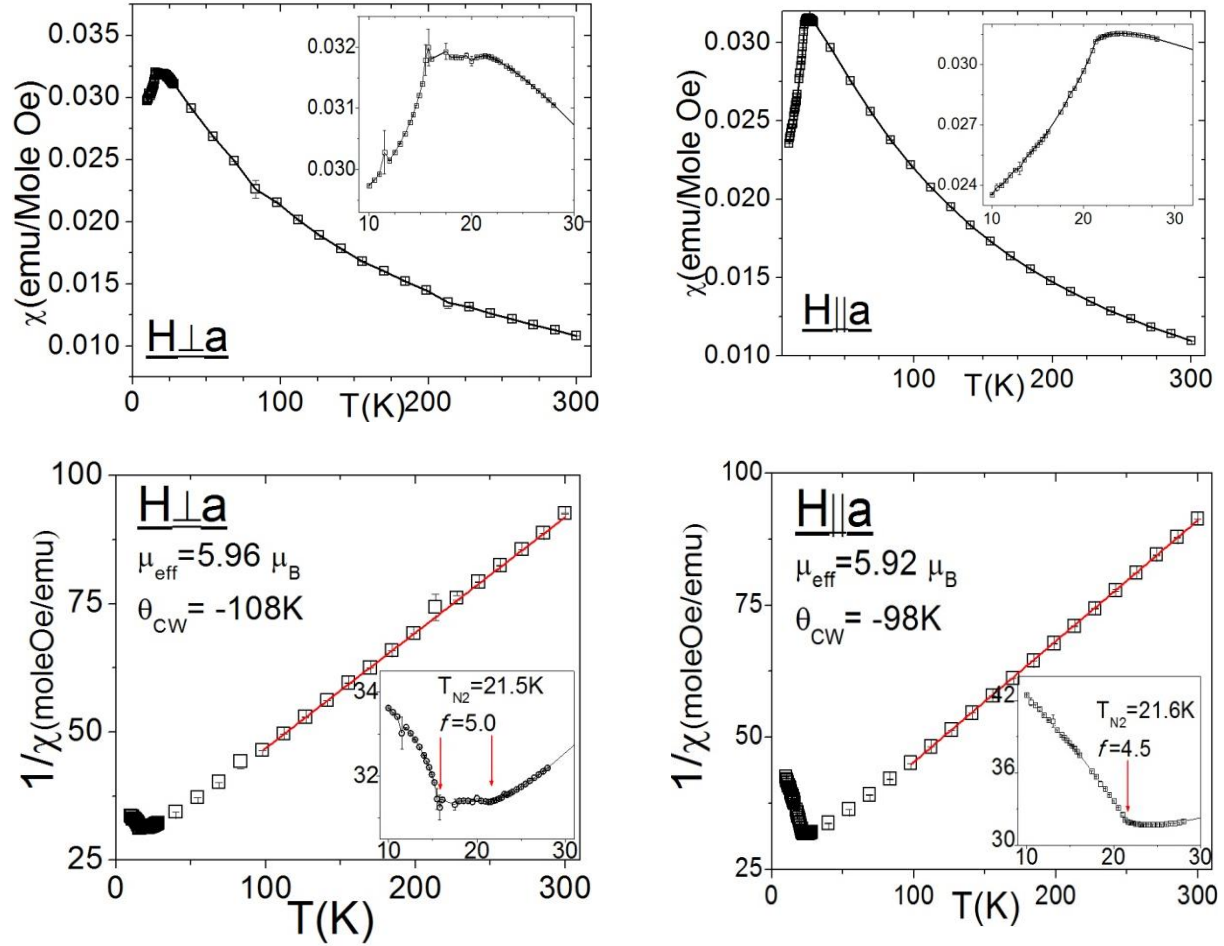


Figure 2.11: Magnetic susceptibility and inverse magnetic susceptibility versus temperature data for  $\text{FeVO}_4$  single crystals, with the crystals oriented perpendicular to and parallel to the crystallographic axis  $a$ .

The high temperature portion of  $1/\chi$  vs  $T$  plots can be fit to a straight line following the Curie-Weiss law:

$$\frac{1}{\chi} = \frac{T}{C} - \frac{\theta_{CW}}{C} \quad (2.3)$$

Here  $C$  is Curie's constant and  $\theta_{CW}$  is Curie-Weiss temperature. By fitting the  $1/\chi$  vs  $T$  graph to a straight line, one can obtain an estimate of  $\theta_{CW}$  as the quotient of dividing the intercept by the slope. The estimated values for  $\theta_{CW}$  from figure 2.11 are 98 K ( $H \parallel a$ ) and 108 K ( $H \perp a$ ).

On the other hand, the linear portion can be traced by equation 2.4:

$$\chi_m = \frac{\mu_o N_A \mu_{eff}^2 \mu_B^2}{3k_B T} \quad (2.4)$$

Where  $\chi_m$  is the molar magnetic susceptibility,  $\mu_o$  is the free space permeability,  $N_A$  is Avogadro's number and  $k_B$  is Boltzmann's constant. Also,  $\mu_B$  is the Bohr magneton, and is used to quantify the ionic magnetic moment since it corresponds to the magnetic moment produced by a single electron in the  $1s$  orbital in the hydrogen atom ( $\mu_B = 9.274 \times 10^{-24} \frac{\text{Joule}}{\text{Tesla}}$ ) [3].

With reference to equation 2.4,  $\mu_{eff}$  is called the effective magnetic moment, and is a good measure of the magnetic properties since it is independent of temperature in materials obeying Curie-Weiss law [81]. Upon rearranging equation 2.4, one obtains:

$$\mu_{eff} = \sqrt{\frac{3k_B}{\mu_o N_A \mu_B^2}} \times \sqrt{\chi_m T} \quad (2.5)$$

By putting in the appropriate values of constants in *cgs* units, and keeping in mind that the slope of  $1/\chi_m$  vs  $T$  graph equals  $\frac{1}{\chi_m T}$ , we reach

$$\mu_{eff} = \sqrt{\frac{8}{\text{slope}}} \quad (\text{in cgs units}) \quad (2.6)$$

Based on equation 2.6, the effective moment ( $\mu_{eff}$ ) is calculated from the  $\text{FeVO}_4$  magnetic data to be  $5.92 \mu_B$  and  $5.96 \mu_B$  for  $H \parallel a$  and  $H \perp a$  respectively. These numbers are consistent with the theoretical value for  $\text{Fe}^{3+}$  ion calculated from equation 2.7, with  $s = \frac{5}{2}$ , considering contribution from electrons' spins only with Landé  $g$ -factor of 2.

$$\mu_{eff}(\text{theoretical}) = g\sqrt{s(s+1)}\mu_B \quad (2.7)$$

The frustration index, defined as  $f = \frac{-\theta_{CW}}{T_N}$  [19], is found to be a little smaller along  $a$ .

This suggests the existence of weaker interactions between magnetic  $\text{Fe}^{3+}$  ions in this direction,

that is, the super-super exchange interaction between the iron ions on the different  $S$ -shaped clusters depicted in figure 2.2.

#### 2.2.4 DIELECTRIC AND FERROELECTRIC MEASUREMENTS

When a specimen of a dielectric material is subject to an external electric field, bound charges will displace giving rise to electric dipole moments, defined as (lowercase  $p$ ):

$$p = q|\vec{x}| \quad (2.8)$$

Where  $\vec{x}$  is the displacement vector of bound charge ‘ $q$ ’. For a specimen with charge density  $nq$ , one can define the polarization density as (uppercase  $P$ ):

$$P = nq|\vec{x}| \quad (2.9)$$

A ferroelectric specimen kept below its ferroelectric transition temperature (Curie’s temperature) develops spontaneous dipole moments and polarization density, the values of which will be greater if the sample is cooled down under an external electric field because individual moments will seek a minimum potential energy configuration (i.e.: will align parallel to the external field). On the other hand, warming up a ferroelectric specimen to the Curie point will eliminate its polarizability. In such process, the bound charges are regarded as effectively moving to neutralize the dipoles which existed in the ferroelectric before (i.e.: below the Curie point). Such motion of charges takes place over a very short time period, generating a current density:

$$\frac{dP}{dt} = nq \frac{d|\vec{x}|}{dt} = \frac{I(t)}{A} \quad (2.10)$$

Here,  $I(t)$  is dubbed the ‘Pyrocurrent’ because it is generated as a result of heating the specimen.

The integration of  $I(t)$  yields the *polarization moment per unit volume*:

$$P = \int \frac{I(t)}{A} dt \quad (2.11)$$



In this work, we utilize equation 2.11 to get the ferroelectric polarization moment as a function of temperature by integrating the pyrocurrent data with respect to time. First, we select a relatively large  $\text{FeVO}_4$  crystal for the ease of making aluminum foil masks. Then, gold electrodes were deposited on both sides of the crystal, to which gold wires were attached by conductive silver paint. The sample is then cooled down to  $T < 10$  K under high voltage ( $\pm 200$  V) provided by a Keithely 6517A electrometer, while the temperature control is provided through a Quantum Design Physical Property Measurement System (PPMS). The field applied was high enough to ensure the sample is saturated. The poling high voltage creates an electric field in the order of kV/cm, and acts to align the ferroelectric domains which form below the ferroelectric transition temperature. Once the target low temperature is reached, the high voltage is turned off and the sample is warmed up to 25 K at a rate of 5 K/minute while recording the pyrocurrent signal using the same Keithely electrometer. The signal is recorded versus temperature while keeping track of the time change as well.

The ferroelectric transition in  $\text{FeVO}_4$  crystals is marked by a sharp peak in the pyrocurrent data, which is observed with the electric field parallel to the crystallographic axis  $a$  ( $E \parallel a$ ) as well as normal to it ( $E \perp a$ ). The reversibility of the generated polarization moment is shown by repeating the measurement after reversing the poling voltage. Integration of the pyrocurrent signal with respect to time gives the ferroelectric polarization moment, which is found to be about three times larger when measured along the crystal  $a$ -axis (figure 2.12), with values of  $9 \mu\text{C}/\text{m}^2$  and  $27 \mu\text{C}/\text{m}^2$  for  $E \perp a$  and  $E \parallel a$  respectively. The observation of such large anisotropy along different directions is significant, because it is the first time to measure the ferroelectric polarization moment in  $\text{FeVO}_4$  single crystals. These measurements were repeated a few times on different crystals to be confirmed (figure 2.13). The obtained values for the  $E \perp a$

case are found to be a little higher than those reported earlier for polycrystalline pellets [77] and thin films [82], and significantly higher for  $E \parallel a$ . It should be noted that applied voltage in our measurements corresponds to an electric field of  $\sim 350$  kV/m, which is an order of magnitude less than the one applied in thin films measurements in reference [82]. The observation of our polarization values being higher, in spite of applying a lower electric field, strongly supports the ferroelectric anisotropy in  $\text{FeVO}_4$  single crystals.

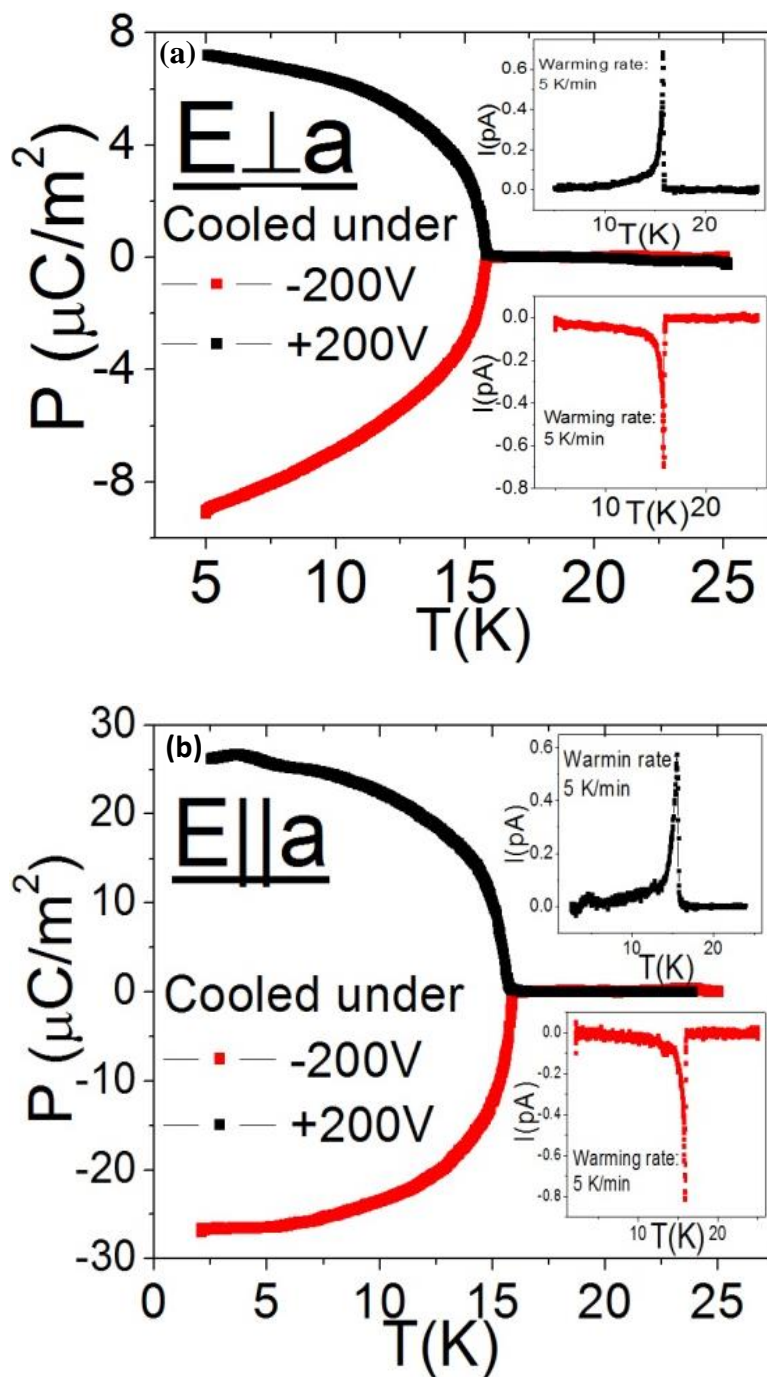


Figure 2.12: Reversible ferroelectric polarization perpendicular to the crystal long axis (a) and parallel to it (b). The insets in (a) and (b) represent the recorded pyrocurrent signals.

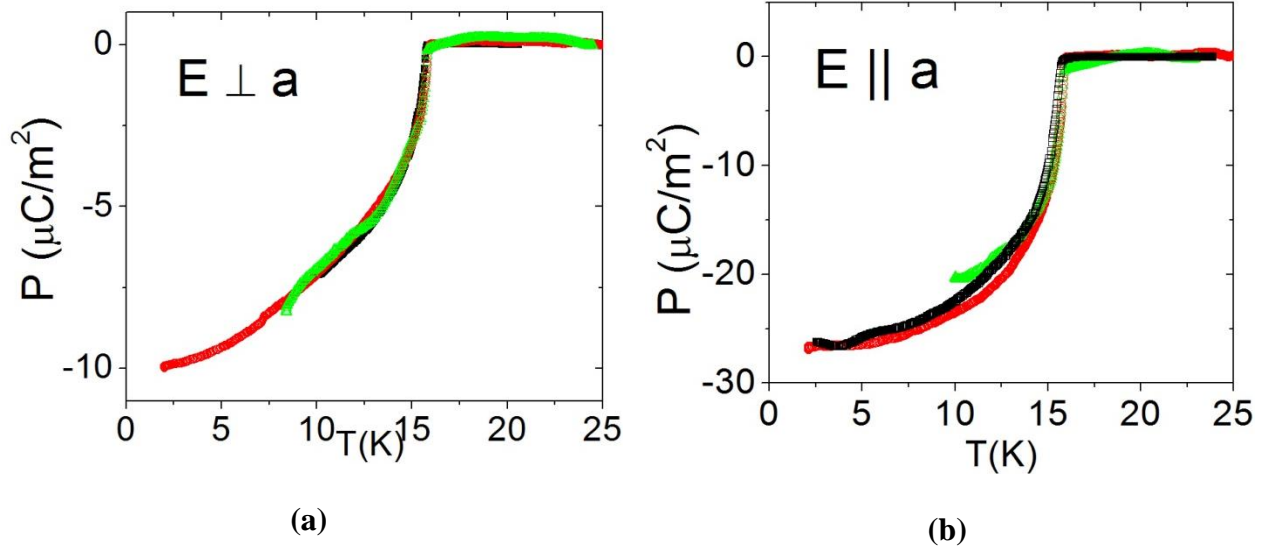


Figure 2.13: Repeated measurements of ferroelectric polarization on different  $\text{FeVO}_4$  crystals perpendicular  $a$  (a) and along  $a$  (b). The different curve colors represent different runs.

The dielectric constant of the  $\text{FeVO}_4$  crystals as a function of temperature was extracted from capacitance data recorded using an HP 4284A Precision LCR meter. The data were recorded at 100 kHz and 1 V peak-to-peak voltage value. The temperature control was again provided by the PPMS, where the temperature was scanned from 12 K to 18 K at 1 K/minute. By knowing the area of the electrodes ' $A$ ' and the thickness of the sample ' $d$ ', the dielectric constant is calculated from the capacitance with the help of equation 2.8:

$$\epsilon_r = \frac{C \times d}{\epsilon_0 A} \quad (2.12)$$

Figure 2.14 represents the relative dielectric constant of  $\text{FeVO}_4$  single crystals when measured along two normal directions with respect to the crystal  $a$ -axis. The measured values are much higher when compared with dielectric constant of powder samples reported in literature [75, 77, 82], owing to the absence of grain boundary effects. The data show a more significant change along  $a$  axis here as well, indicating that the charge distribution within the individual S-shaped clusters contributes more to the macroscopic polarization moment.

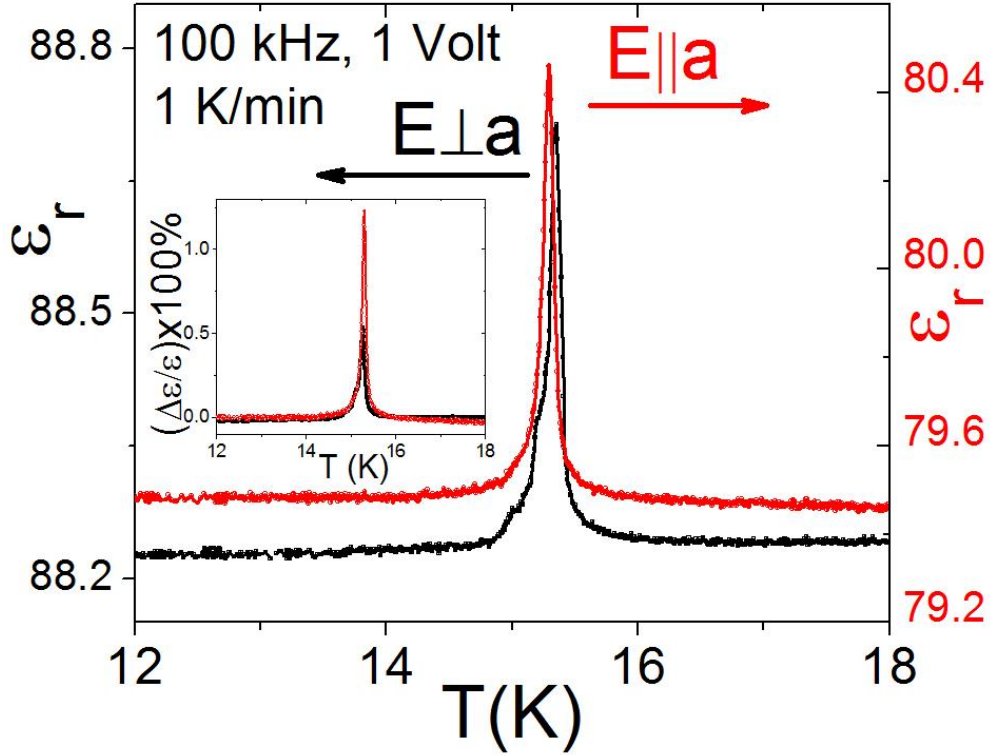


Figure 2.14: Relative dielectric constant of  $\text{FeVO}_4$  single crystals measured perpendicular to the  $a$ -axis (left, black scale) and parallel to the  $a$ -axis (right, red scale). The inset shows the relative change in the parallel and perpendicular components of  $\epsilon_r$ .

## 2.2.5 MAGNETO-DIELECTRIC COUPLING

In general, the free energy for the magnetically ordered phase can be written as [82]:

$$F = F_M + F_E + V \quad (2.13)$$

Where  $F_M$  and  $F_E$  represent the magnetic and dielectric contributions to the free energy, respectively.  $V$ , on the other hand, represents the magneto-electric coupling term. According to the Landau treatment of the Mean Field Theory, the free energy can be written as a power series of the order parameter (or parameters) [83]. For simplicity, it is usually assumed the order parameters are small to allow keeping only the lower powers of expansion. Accordingly, the term  $V$  from equation 2.13 can be written in terms of the two magnetic order parameters  $\sigma_1(q)$  and  $\sigma_2(q)$  as:

$$V = \sum_{\gamma} [a_{\gamma} \sigma_1(\vec{q}) \sigma_2(\vec{q})^* + a_{\gamma}^* \sigma_1(\vec{q})^* \sigma_2(\vec{q})] P_{\gamma} \quad (2.14)$$

Where  $q$  is called the ordering wave vector,  $P_{\gamma}$  is the ferroelectric polarization component in the  $\gamma$ -direction and  $a_{\gamma}$  are the expansion coefficients. Note that  $V$  has to be inversion invariant, which disallows terms such as  $|\sigma_1(\vec{q})|^2$  and  $|\sigma_2(\vec{q})|^2$ . Furthermore, the effect of the space inversion operator  $\mathcal{J}$  on the vectors  $\vec{P}$  and  $\sigma_i(\vec{q})$  is given in equations 2.15:

$$\mathcal{J}(\vec{P}) = -\vec{P} \quad (2.15-a)$$

$$\mathcal{J}(\sigma_i(\vec{q})) = (\sigma_i(\vec{q}))^* \quad (2.15-b)$$

Which implies that the coefficients  $a_{\gamma}$  are pure imaginary (i.e.:  $a_{\gamma} = ir_{\gamma}$ ), allowing us to write  $V$  as:

$$V = 2 \sum_{\gamma} r_{\gamma} |\sigma_1(\vec{q}) \sigma_2(\vec{q})| \sin(\varphi_1 - \varphi_2) P_{\gamma} \quad (2.16)$$

With  $\varphi_1$  and  $\varphi_2$  denoting the phases of the order parameters  $\sigma_1$  and  $\sigma_2$ . Equation 2.16 is important because it indicates that the two order parameters have to be out of phase for magneto-electric coupling to occur [82].

We investigate the synthesized  $\text{FeVO}_4$  single crystals for magneto-electric coupling by measuring the relative change in dielectric constant as a function of magnetic field at several fixed temperatures. The samples were kept at a fixed temperature while the magnetic field was swept between  $\pm 8$  Tesla. The data shows a negative magneto-capacitive coupling, which generally increases at lower temperatures (figure 2.15) similar to what was reported before on  $\text{Ni}_3\text{V}_2\text{O}_8$  single crystals [84]. This effect is attributed to field induced spin reorientation, as proposed by Dixit *et al.* [82]. The coupling also originates at lower field values along the  $a$ -axis, which could be linked to the observation that the  $a$ -axis is a magnetically easy direction.

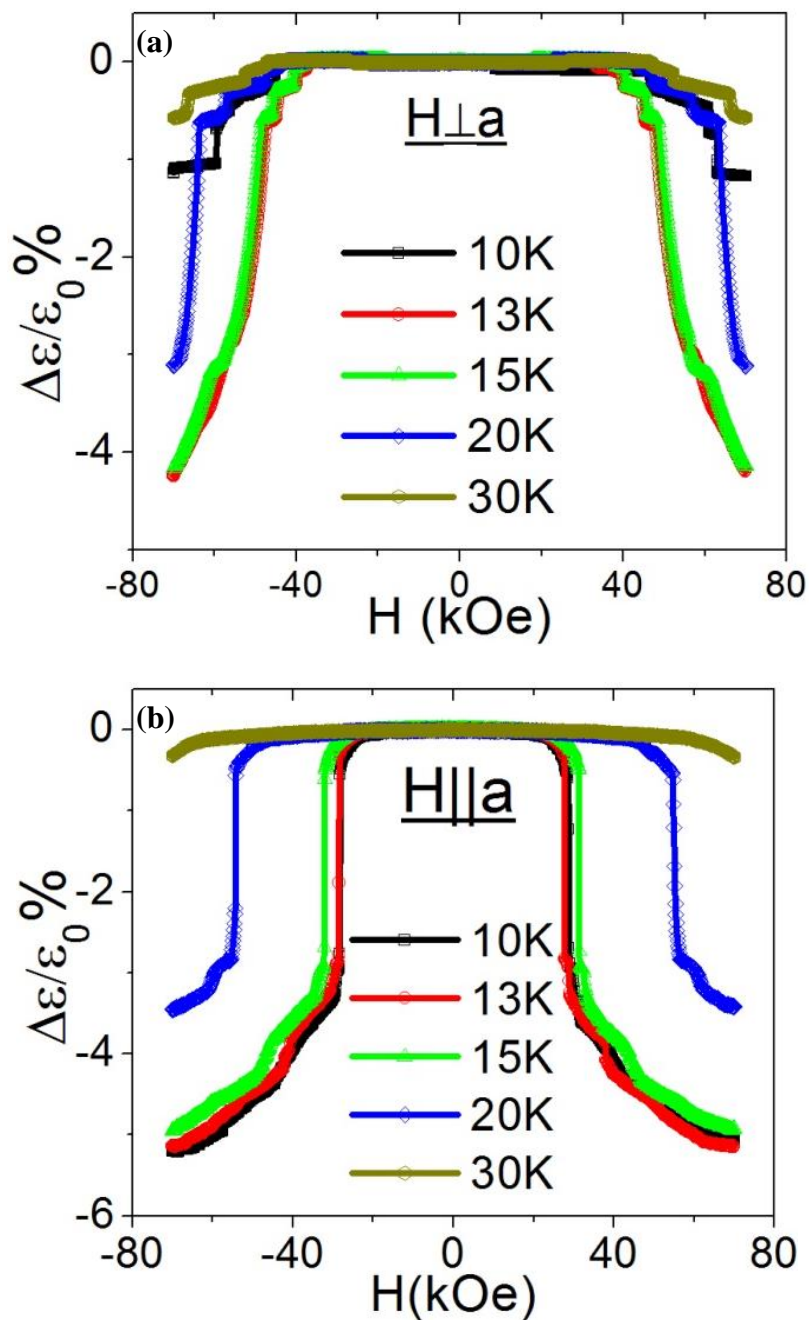


Figure 2.15: Magneto-dielectric coupling perpendicular (a) and parallel (b) to  $a$ . The abscissa is the change in dielectric constant with reference to the value at  $H = 0$  Tesla.

To investigate the basis of such coupling, we recorded the crystals' M-H behavior at fixed temperatures. The proposed magnetic field-induced spin orientations would have been shown as anomalies in isothermal M-H behavior. On the contrary, the data show linear

paramagnetic response at temperatures above and below the two Néel transitions. The isothermal magnetic susceptibility values, estimated from the M-H plots in figure 2.16 are represented in figure 2.17.

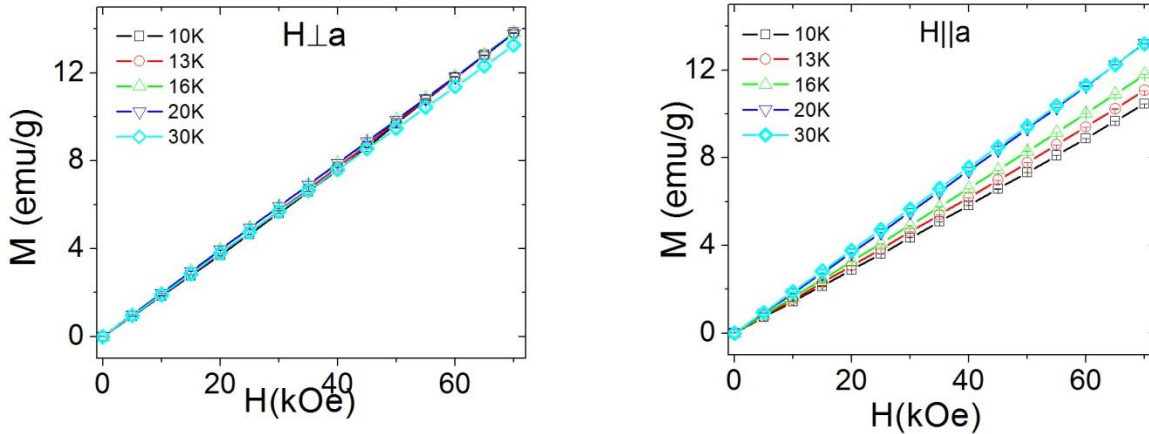


Figure 2.16: Isothermal M vs H data for  $\text{FeVO}_4$  single crystals.

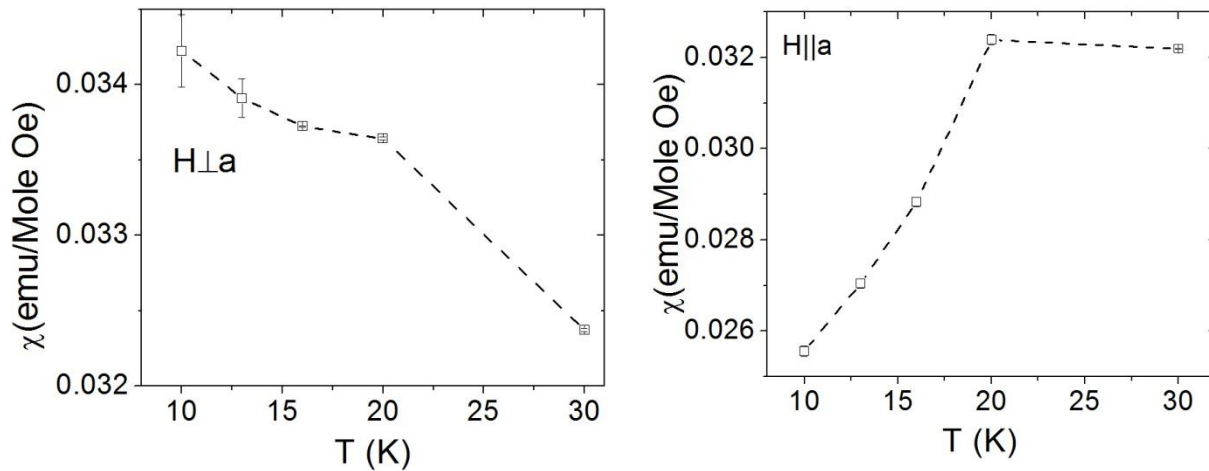


Figure 2.17: The magnetic susceptibility values estimated from the isothermal M-H plots in figure 2.16.

### 2.3 DOPED $\text{FeVO}_4$ SINGLE CRYSTALS

Doped  $\text{FeVO}_4$  single crystals were prepared following the same procedure, aiming to replace some of the iron content with zinc and manganese. Divalent zinc is chosen with the intention to explore the role of exchange striction in  $\text{FeVO}_4$  ferroelectricity. By substituting  $\text{Fe}^{3+}$



( $s = \frac{5}{2}$ ) with non-magnetic  $\text{Zn}^{2+}$  ( $s = 0$ ), we reduce the average spin at the iron site, which would modify the exchange striction along with the resulting ferroelectric moment [50]. On the other hand,  $\text{Mn}^{3+}$  ( $s = 2$ ) was used for having single-ion anisotropy, hence altering the strength of spin-orbit coupling allowing for examining the role of Dzyaloshinskii-Moriya interaction [85].

The Zn and Mn ions were introduced in the form of oxalates; zinc oxalate dihydrate  $\text{ZnC}_2\text{O}_4 \cdot 2\text{H}_2\text{O}$  (CAS# 4255-07-6) and manganese oxalate dihydrate  $\text{MnC}_2\text{O}_4 \cdot 2\text{H}_2\text{O}$  (CAS# 6556-16-7). The precursors were mixed in the proper stoichiometric amounts aiming for 5%, 10% and 20% substitution percentages. Table 2.3 lists the masses (in grams) of precursors used for each composition.

$\text{Fe}_{1-x}\text{Zn}_x\text{VO}_4$	Iron oxalate	Zinc Oxalate	Manganese Oxalate	Vanadium Oxide
$x=0$	25	---	---	25.30
$x=0.05$	23.49	1.30	---	25
$x=0.1$	22.25	2.60	---	25
$x=0.2$	19.78	5.20	---	25
$\text{Fe}_{1-x}\text{Mn}_x\text{VO}_4$				
$x=0.05$	23.49	---	1.23	25
$x=0.1$	22.25	---	2.46	25
$x=0.2$	19.78	---	4.92	25

Table 2.3: Masses (in grams) of precursors used to prepare undoped, Zn- and Mn-doped  $\text{FeVO}_4$  single crystals.

EDAX analysis was used to study the stoichiometry of the synthesized crystals. The spectra were recorded using a JSM-7600 field-emission scanning electron microscope. The data

revealed significant discrepancies between the aimed stoichiometries and the actual ones, indicating that most of the dopant ions are not incorporated into the structure. The dopant contents reported by EDAX are listed in table 2.4.

Aimed Stoichiometry	Measured by EDAX	Aimed Stoichiometry	Measured by EDAX
$\text{Fe}_{1-x}\text{Zn}_x\text{VO}_4$		$\text{Fe}_{1-x}\text{Mn}_x\text{VO}_4$	
x=0.05	$0.032 \pm 0.009$	x=0.05	$0.013 \pm 0.006$
x=0.1	$0.051 \pm 0.020$	x=0.1	$0.008 \pm 0.001$
x=0.2	$0.041 \pm 0.011$	x=0.2	$0.016 \pm 0.002$

Table 2.4: Aimed and measured stoichiometric ratios for Zn- and Mn-doped  $\text{FeVO}_4$  crystals.

XRD and Raman analysis were used to confirm the structure of doped crystals. Some washed crystals were ground to obtain powder XRD patterns (figure 2.18). The formation of secondary phases can be ruled out within the XRD detection limits. On the other hand, Raman spectra for the Zn-doped samples are quite similar to the undoped one (figure 2.19), except for the expected slight change in peak intensities of the weak modes associated with the V—O—Fe bonds between  $136$  and  $210 \text{ cm}^{-1}$ . This observation confirms the substitution of some  $\text{Fe}^{3+}$  ions by  $\text{Zn}^{2+}$ .

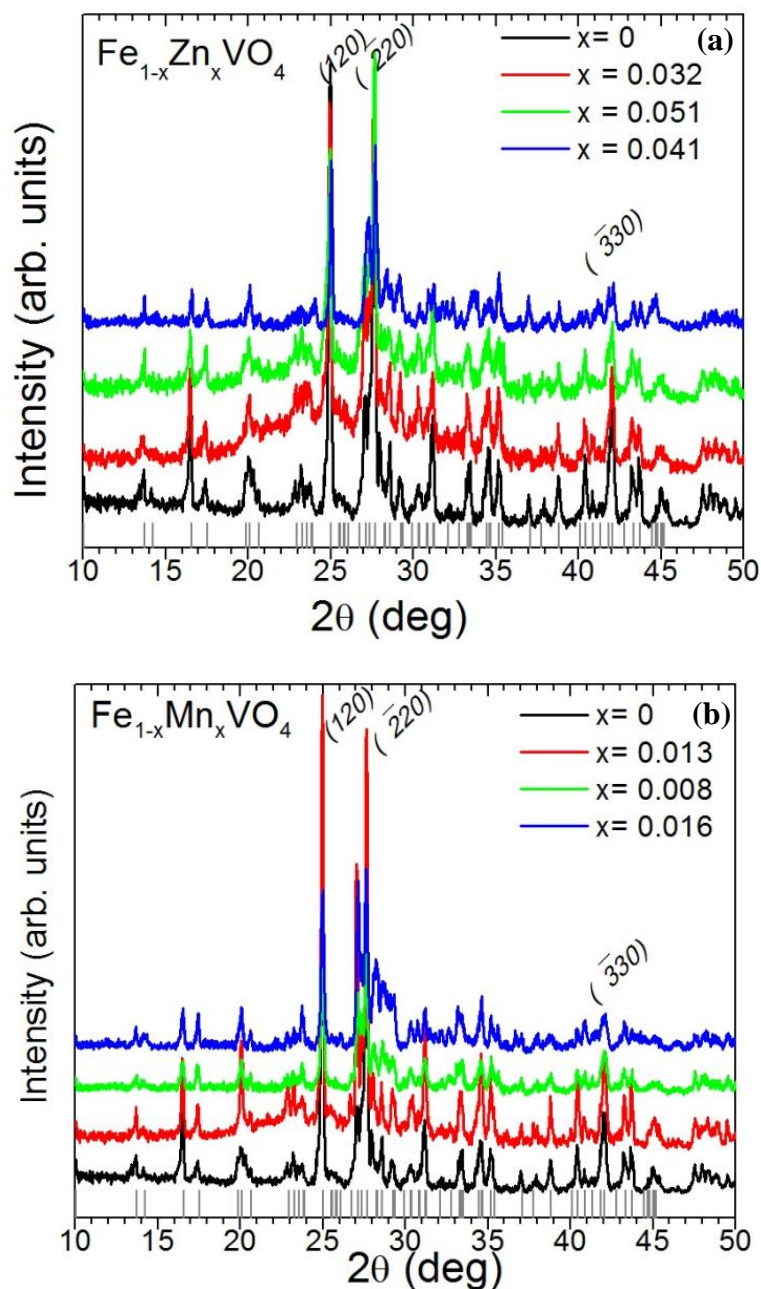


Figure 2.18: XRD spectra for undoped  $\text{FeVO}_4$  and (a) Zn-doped samples and (b) Mn-doped ground crystals. The grey lines at the bottom indicate the positions of the lines listed in the standard powder diffraction file.

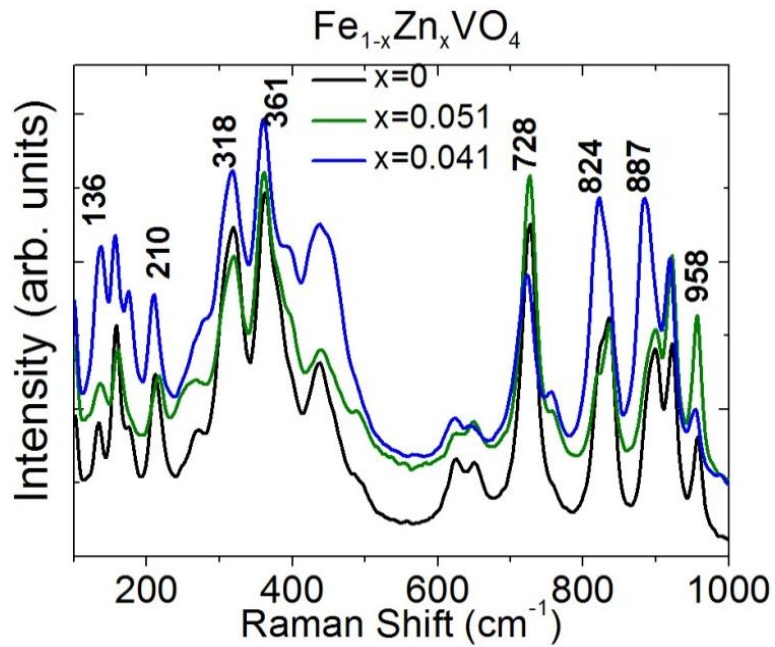


Figure 2.19: Raman spectra of undoped and Zn-doped  $\text{FeVO}_4$  crystals.

Magnetic measurements carried out on doped crystals reveal similar behavior to that of the undoped ones. All samples become antiferromagnetic below  $\sim 22$  K, and the collinear-to-non-collinear transition observed only when magnetization is measured along the  $a$ -axis (figure 2.20).

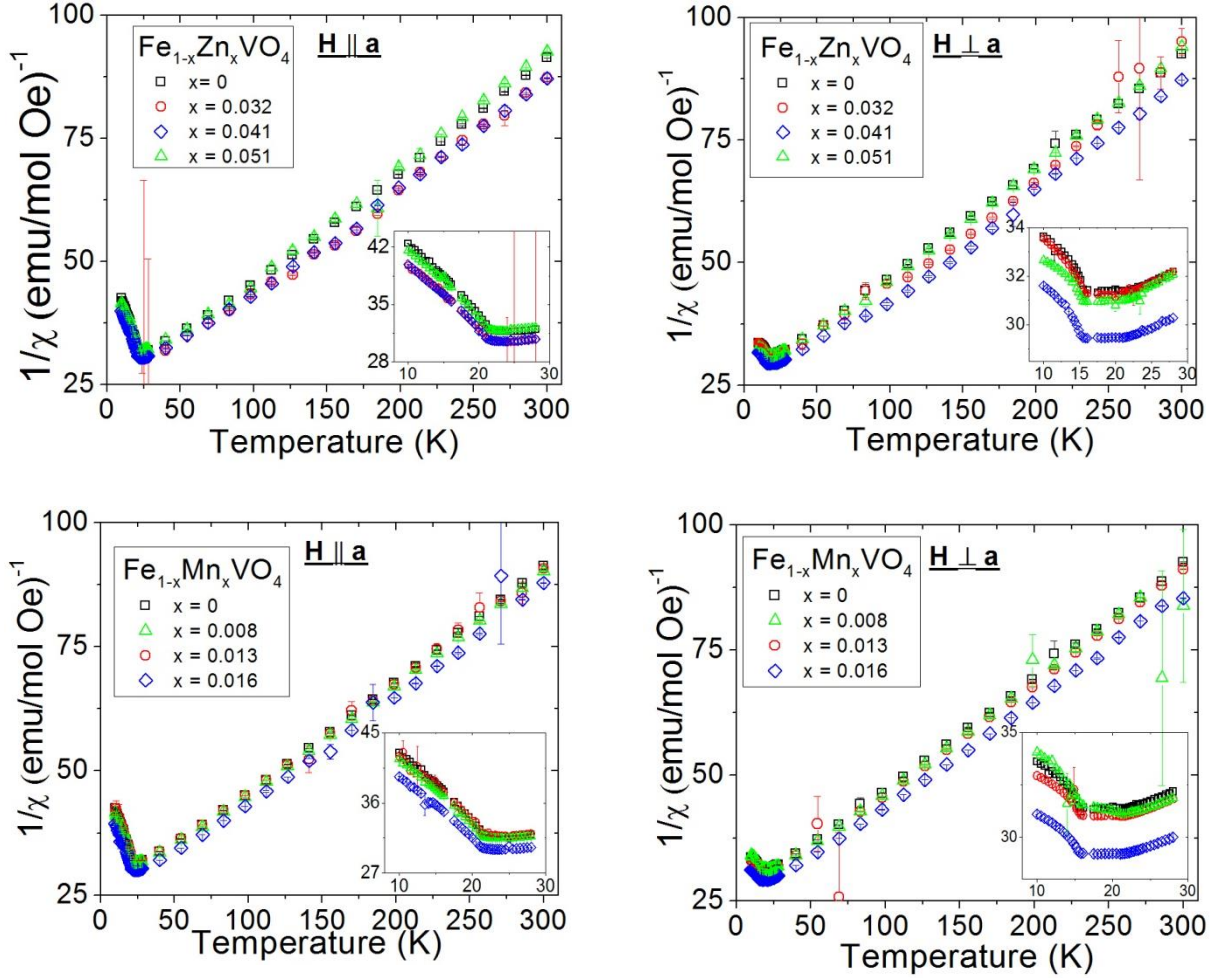


Figure 2.20: Inverse susceptibility versus temperature data for doped  $\text{FeVO}_4$  single crystals recorded along the crystallographic axis  $a$  and perpendicular to it. The insets highlight the lack of signals to the collinear-to-non-collinear AFM transition around 15 K in case  $H$  is parallel to  $a$ .

The effective moment ( $\mu_{eff}$ ) and Curie-Weiss temperature ( $\theta_{CW}$ ) values are estimated from the linear portions ( $T > 100$  K) in figure 2.20 plots and listed in table 2.5.

	Effective Moment ( $\mu_{eff}$ )			Curie-Weiss Temperature ( $\theta_{CW}$ )	
	H $\perp$ a	H $\parallel$ a		H $\perp$ a	H $\parallel$ a
FeVO <sub>4</sub>	5.96±0.01	5.92±0.01		108±0	98±0
Fe <sub>1-x</sub> Zn <sub>x</sub> VO <sub>4</sub>					
x=0.032	6.14±0.08	6.06±0.02		113±1	100±1
x=0.041	6.02±0.01	6.04±0.01		95±1	98±1
x=0.051	5.87±0.01	5.75±0.01		100±0	85±1
Fe <sub>1-x</sub> Mn <sub>x</sub> VO <sub>4</sub>					
x=0.008	5.94±0.01	5.96±0.01		104±0	100±0
x=0.013	5.98±0.02	5.94±0.01		104±1	100±0
x=0.016	6.15±0.02	5.99±0.02		105±0	92±0

Table 2.5: Effective moment ( $\mu_{eff}$ ) and Curie-Weiss temperature ( $\theta_{CW}$ ) values for pristine and doped FeVO<sub>4</sub> single crystals. The listed values for  $\mu_{eff}$  are in Bohr magneton ( $\mu_B$ ), and values of  $\theta_{CW}$  are in kelvin.

The effective moment per magnetic ion is expected to get reduced upon substitution of magnetic Fe<sup>3+</sup> ion ( $s = \frac{5}{2}$ ) with Zn<sup>2+</sup> ( $s = 0$ ) and Mn<sup>3+</sup> ( $s = 2$ ). However, the evolution of  $\mu_{eff}$  shown in table 2.5 does not support such expectation;  $\mu_{eff}$  is seen to be highest for the Zn-doped sample having the lowest zinc content (x=0.032) and shows a steady decrease with increasing zinc content. This can be due to disturbances in local symmetry upon replacing Fe<sup>3+</sup> with Zn<sup>2+</sup>, which leads to changes in  $d$ -orbitals degeneracy and electrons' occupancy in these orbitals, giving rise to a non-zero orbital angular momentum. Increasing Mn<sup>3+</sup> content, on the other hand, results in a higher effective moment per magnetic ion.

The collinear-to-non-collinear AFM transition marking the onset of ferroelectric ordering is observed in dielectric data of the doped crystals as well. The relative change in dielectric constant is shown in figure 2.21 as a function of temperature for some of the compositions, where the y-axis represents the relative change in the dielectric constant with respect to its value far away from the transition (at  $T = 12$  K). We note that doping drastically reduced the amplitude of the relative change. Also, since the doped crystals tend to grow smaller compared to the undoped ones, the dielectric data could only be obtained for a few compositions; for crystal whose facets were big enough to make electrodes without shorting the sample.

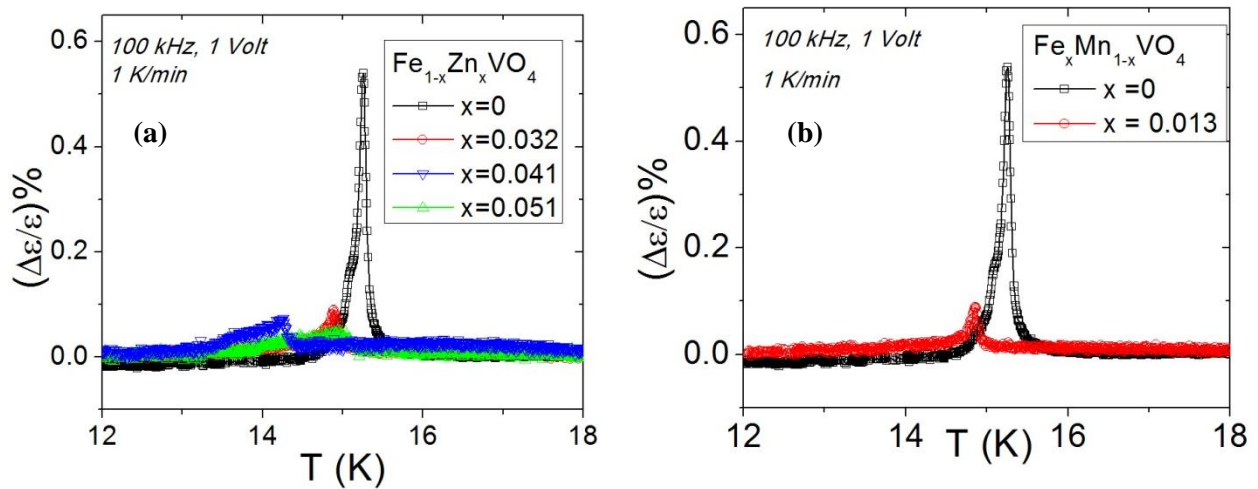


Figure 2.21: Relative change in dielectric constant of (a) Zn-doped and (b) Mn-doped  $\text{FeVO}_4$  single crystals, recorded with an electric field perpendicular to the crystallographic axis  $a$ .

The low temperature AFM transition was proven to mark a ferroelectric transition by recording the pyrocurrent signals for the crystals with different dopant contents (figure 2.22 (a,b)). The measurements were carried out in a similar manner to the undoped samples, with a poling voltage of -200 V. The ferroelectric polarization moments were calculated by integrating the pyrocurrent signals with respect to time (figure 2.22(c,d)). The polarization moment is shown to decrease in Zn- and Mn-doped samples. In the Zn-doped samples, this is attributed to the

difference in valency between  $\text{Zn}^{2+}$  and  $\text{Fe}^{3+}$  resulting in increased leakage in the doped crystals. On the other hand, the polarization values reported for Mn-doped polycrystalline samples [76] are slightly higher than the ones we report here on single crystals, which we attribute to the inherent imperfections observed in the doped crystals. Finally, the ferroelectric nature of the Zn-doped crystals is further confirmed by reporting the reversibility of the polarization moment in figure 2.23.

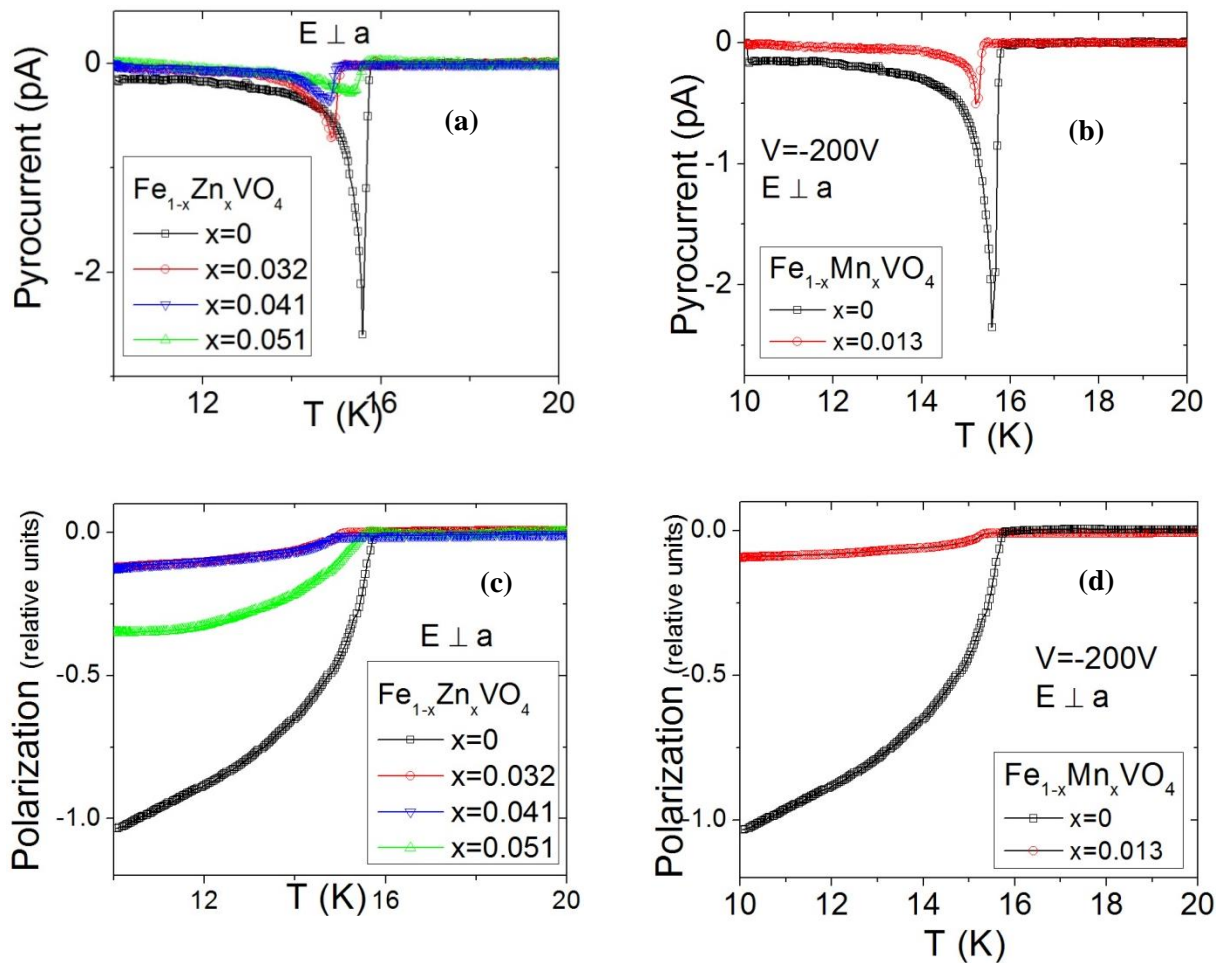


Figure 2.22: Pyrocurrent (a,b) and polarization moment (c,d) data for the Zn- and Mn-doped  $\text{FeVO}_4$  crystals.



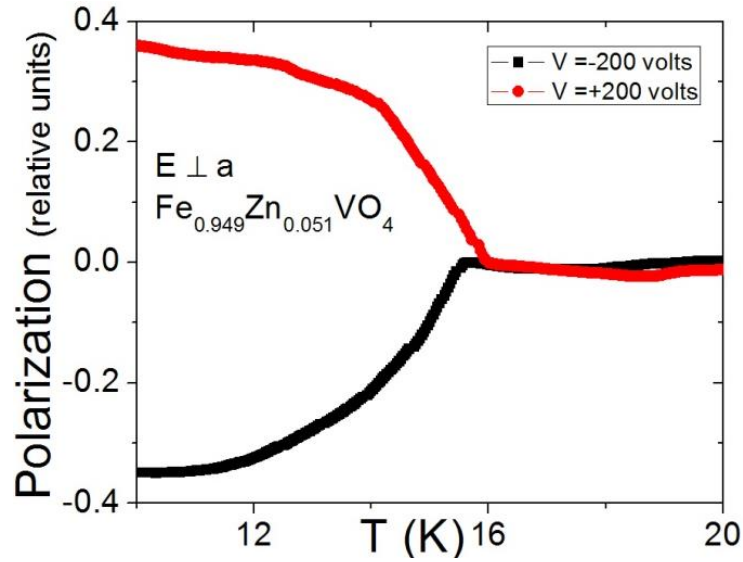


Figure 2.23: Reversible ferroelectric polarization of Zn-doped FeVO<sub>4</sub> crystals.

The dependences of the magnetic effective moment ' $\mu_{eff}$ ' and ferroelectric polarization ' $P$ ' on the zinc content are plotted in figure 2.24. The plot suggests an inverse relation between ' $\mu_{eff}$ ' and ' $P$ '. More data points between 0% and 3% are needed to confirm such behavior.

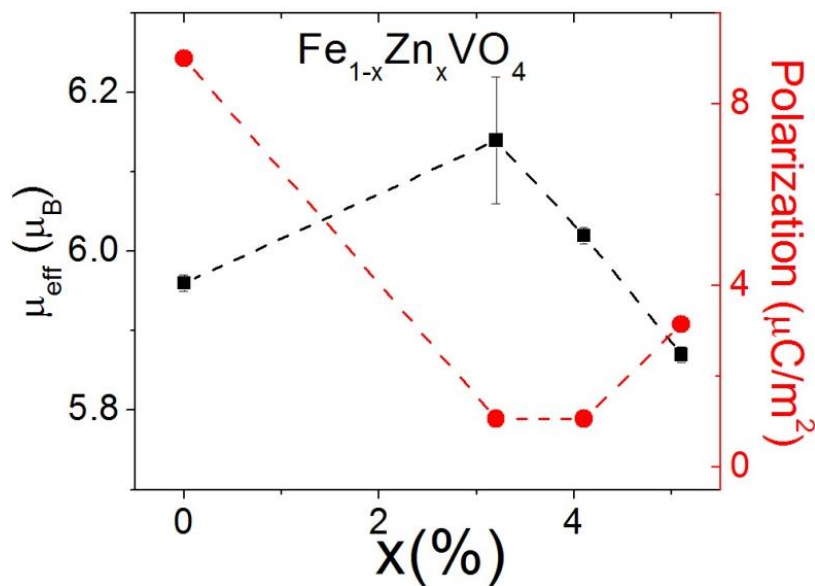


Figure 2.24: The the magnetic effective moment ' $\mu_{eff}$ ' and ferroelectric polarization ' $P$ ' as functions in zinc content in FeVO<sub>4</sub> single crystals.

## 2.4 CONCLUSIONS AND FUTURE WORK

Undoped single crystals of triclinic  $\text{FeVO}_4$  are synthesized from molten flux by flux-growth method for the purpose of studying the anisotropy in magnetic and ferroelectric properties. Measurements were performed along two orthogonal directions with respect to the crystals' direction of growth, which was revealed to be the crystallographic  $a$ -axis. It is shown from the temperature dependence of the inverse susceptibility data below the AFM-paramagnetic transition at 22 K that the relative change in susceptibility is higher along the  $a$ -axis than when recorded perpendicular to the  $a$ -axis (figure 2.11). This denotes  $a$  as a magnetically easy axis and favorable for magnetic moments alignment. As a consequence, the non-collinear-to-collinear transition around 15 K is not revealed in the magnetic data perpendicular to the  $a$ -axis.

The components of ferroelectric polarization moment of  $\text{FeVO}_4$  single crystals along  $a$  and normal to  $a$  were calculated by integrating the pyrocurrent signals. The polarization moment density of  $\text{FeVO}_4$  was shown to be higher in the direction of  $a$  (figure 2.12), denoting this direction to be favorable from the electric polarization viewpoint as well. This is supported by noting that the relative change in dielectric constant versus temperature (figure 2.14) is larger along the  $a$ -axis.

In an attempt to reveal the origin of multiferroic coupling in  $\text{FeVO}_4$ , we recorded the relative change in dielectric constant as a function of magnetic field at various temperature values, chosen around the two Néel points; 15 K and 22 K. The data manifest a strong dependence of the dielectric behavior on magnetic field, with the onset of change in dielectric constant occurring at higher magnetic field values perpendicular to the  $a$ -axis. This behavior could not be attributed field-induced spin reorientations as suggested earlier [82], with the single crystals isothermal M vs H data showing primarily a paramagnetic linear response.

Zinc-doped  $\text{FeVO}_4$  single crystals were prepared to investigate the role of magnetically induced lattice distortions in creating the spontaneous ferroelectric moment. Substituting  $\text{Fe}^{3+}$  with  $\text{Zn}^{2+}$  aims to reduce exchange striction between the two ions, since the latter has a lower spin magnetic moment. On the other hand, manganese-doped crystals were also prepared to test for the role played by Dzyaloshinskii-Moriya interaction (i.e.: spin-orbit coupling) in  $\text{FeVO}_4$  ferroelectricity. Estimating the crystals' stoichiometries by EDAX indicated the difficulty of incorporating zinc and manganese elements in the  $\text{FeVO}_4$  structure, which is mainly due to the insolubility of these metals in the flux material used,  $\text{V}_2\text{O}_5$ . The doped crystals were also found to be smaller in size than the undoped ones, which rendered it hard to carry out the desired ferroelectric characterization on some compositions.

The magnetic susceptibility dependence on temperature was measured for the doped crystals, where the data were found to be qualitatively similar to the undoped  $\text{FeVO}_4$ , in being antiferromagnetic below 22 K. The effective moment per magnetic ion values were found to be higher than undoped  $\text{FeVO}_4$  for some Zinc contents, unlike theoretical expectations. We attribute this to doping-induced asymmetries in  $\text{Zn}^{2+}$  environments, leading to a non-zero orbital quantum number. The ferroelectric nature of doped crystals was confirmed for some compositions through measuring the polarization moments, where it showed dramatic decrease for the doped samples, owing to induced imperfections and leakage effects. Finally, we note that the ferroelectric transition showed slight shifts towards lower temperatures upon doping.

In the future, we suggest looking for a more suitable method to incorporate the selected dopants in the  $\text{FeVO}_4$  matrix, by adjusting the used times and temperature values in flux growth or by choosing another synthesis route; floating zone method for example. It will also be useful to look into substituting iron with gadolinium ( $\text{Gd}^{3+}$ ) instead of manganese ( $\text{Mn}^{3+}$ ); because rare

earth ions are also characterized by single ion anisotropy beside gadolinium having a better solubility in  $V_2O_5$  flux than manganese.

We also should look into introducing changes in phonon modes by substituting vanadium ( $V^{23}$ ) with heavier transition ions from the same group in the periodic table, namely niobium ( $Nb^{41}$ ) or tantalum ( $Ta^{73}$ ). This will give us a better understanding of the role of spin-phonon coupling in  $FeVO_4$  multiferroicity. However, achieving  $V^{5+}$  doping using the herein reported synthesis method will be difficult; since  $V_2O_5$  is used as the solvent for precursors. Different crystal growth routes may be explored.

## CHAPTER 3: DIELECTRIC AND MAGNETO-DIELECTRIC PROPERTIES OF Gd-DOPED $\text{Fe}_3\text{O}_4$ NANOPARTICLES

### 3.1 BACKGROUND AND PREVIOUS WORK

In chapter 1, different mechanisms of ferroelectricity were presented. We discussed how the long range ordering of charges distribution in an array of atoms or molecules breaks spatial inversion symmetry and creates a net dipole moment (figure 1.14). In type-II multiferroics, the magnetic ordering and charge ordering mechanisms and can have the same origin and set in at the same temperature. On the other hand, magnetism and ferroelectricity in type-I have different origins and often occur at different temperatures. Among the materials belonging to the latter type is magnetite ( $\text{Fe}_3\text{O}_4$ ), which is probably one of the most studied transition metal oxides.

$\text{Fe}_3\text{O}_4$  is known to be the first magnetic material discovered by mankind. It crystallizes in face-centered cubic lattice structure, and belongs to the inverse spinel group (Space group:  $Fd3m$ ) [86]. A normal spinel structure has the formula  $AB_2O_4$ , with the cations  $A^{2+}$  and  $B^{3+}$  surrounded by oxygen anions in tetrahedral and octahedral environments respectively. Such configuration of cations is not unique, and a situation can be found where the  $A^{2+}$  ions occupy the octahedral sites along with half of the  $B^{3+}$  ions, while the other half rests at the tetrahedral sites. Such arrangement is named inverse spinel, of which  $\text{Fe}_3\text{O}_4$  is one example with  $A^{2+}$  and  $B^{3+}$  representing  $\text{Fe}^{2+}$  and  $\text{Fe}^{3+}$  ions respectively.

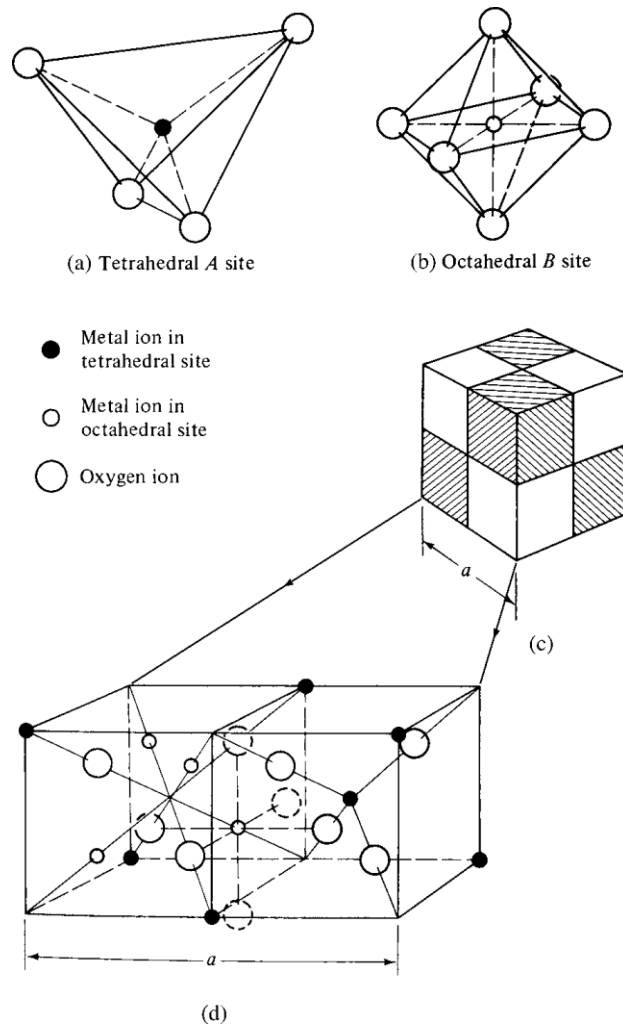


Figure 3.1: Representation of the tetrahedral and octahedral sites in the spinel structure [2].

Two types of magnetic interactions exist in  $\text{Fe}_3\text{O}_4$ ;  $\text{Fe}^{2+}$  and  $\text{Fe}^{3+}$  ions on the octahedral sites are parallel aligned due to double exchange interaction, while  $\text{Fe}^{3+}$  ions on the tetrahedral sites couple to their likes on the octahedral sites via super exchange interaction, arranging antiferromagnetically and cancelling out each other [87]. Thus, the observed net moment in bulk  $\text{Fe}_3\text{O}_4$  is due to  $\text{Fe}^{2+}$  ions, making magnetite a ferrimagnetic material with Curie temperature around 850 K [88]. Furthermore, when magnetite is prepared in nanoparticles form with an average particle size below a certain threshold, it shows superparamagnetic behavior [89].

A hopping mechanism of electrons is going on among the  $\text{Fe}^{2+}$  and  $\text{Fe}^{3+}$  ions occupying the octahedral sites, which can be effectively described as  $\text{Fe}^{2+}$  and  $\text{Fe}^{3+}$  are exchanging positions.  $\text{Fe}_3\text{O}_4$  undergoes an electronic and structural transition around 120 K, known as Verwey transition [90-92], at which this hopping of charges among the octahedral sites ceases to take place. This marks the onset of a charge-ordered phase, and triggers an abrupt rise in resistivity, changing the system from being a conductor to an insulator [93].

As noted earlier,  $\text{Fe}_3\text{O}_4$  forms an inverse spinel cubic structure, with the octahedral  $B$  sites hosting an equal number of  $\text{Fe}^{2+}$  and  $\text{Fe}^{3+}$  ions, making up to two thirds of the iron ions in the composition. The  $B$  sites by themselves form a pyrochlore lattice by building up a network of corner-sharing tetrahedral (figure 3.2).

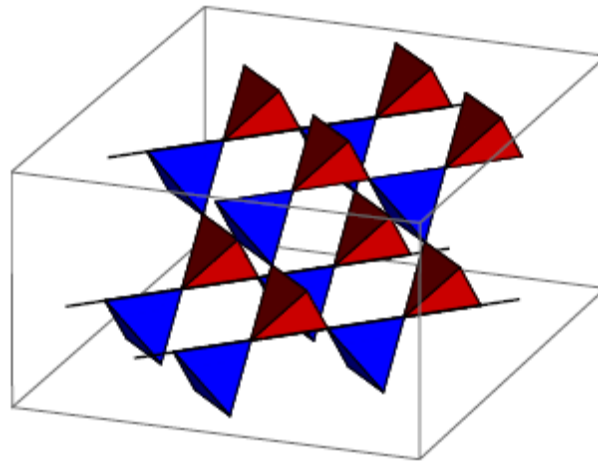


Figure 3.2: Pyrochlore lattice made up by the  $B$  sites of the spinel structure. The iron ions are found at the corners of the tetrahedra. The oxygen ions are not shown here for simplicity [42].

Each pyramid in figure 3.2 would have a mixture of  $\text{Fe}^{2+}$  and  $\text{Fe}^{3+}$  ions. Density functional theory calculations [94] for the charge-ordered phase revealed that one-fourth of the pyramids has an equal number of  $\text{Fe}^{2+}$  and  $\text{Fe}^{3+}$  (i.e.:  $\frac{\text{Fe}^{2+}}{\text{Fe}^{3+}} = \frac{2}{2}$ ), satisfying what is known as Anderson's criterion [95], which is proposed as a necessary condition for charge ordering to take

place in spite of inherent geometrical frustration in the spinel structure. The calculations also showed that the other three-fourth of the tetrahedra host either  $\frac{Fe^{2+}}{Fe^{3+}} = \frac{3}{1}$  or  $\frac{1}{3}$  in a violation to Anderson's criterion. These calculations [94] also show that the structure below Verway transition is monoclinic with  $P2/c$  space group, although a concern arises regarding the centrosymmetric nature of the  $P2/c$  space group precluding the possibility of ferroelectric ordering [42]. Another study [96] based on magnetoelectric measurements on  $Fe_3O_4$  single crystals deduced a triclinic structure for the ferroelectric phase.

The ferroelectric behavior in  $Fe_3O_4$  doesn't manifest itself until low temperatures, even lower than Verway transition.  $Fe_3O_4$  thin films prepared by pulsed laser deposition technique were shown to have non-zero polarization moment only below around 40 K [93]. The disruption of long range charge order above 40 K was attributed to the failure of molecular dipoles to follow the applied low frequency driving field, which is referred to as Debye relaxation. This was supported by the observed dependence of  $\epsilon''$  vs  $T$  peak positions on signal frequency, where  $\epsilon''$  is the imaginary component of the dielectric constant, and  $T$  is the temperature. Such frequency dependence is not observed in conventional ferroelectrics, and indicates a dynamical process, rather than a phase transition.

The observed frequency dependence in dielectric constant data is characteristic of either a relaxor ferroelectric or Maxwell-Wagner-Sillars effect (MWS). The latter was ruled out because similar behavior was seen in dielectric data of  $Fe_3O_4$  single crystals [97]. Since MWS behavior is due to accumulation of charges at the interface between two regions with different dielectric constant, it should not be observed in homogenous single crystals.

The in-phase and out-of-phase components magnetic susceptibility ( $\chi'$  and  $\chi''$ ) dependence on temperature is also reported in reference [93]. Besides the observed discontinuity



around 120 K marking Verwey transition, broad peaks are also observed at lower temperatures – between 40 K and 60 K– in  $\chi''$  vs T plots. These peaks also point towards Debye relaxation model. In such model, the system is considered to consist of non-interacting electric dipoles, with no restoring forces, hence no resonance. The relaxation effect results from the failure of heavy molecular dipoles to follow the applied low frequency driving electric field. Since the ferroelectric order in  $\text{Fe}_3\text{O}_4$  is disrupted by relaxation effects –rather than a crystal phase transition– far below the Verwey transition, it is classified as a relaxor ferroelectric.

Motivated by the ambiguity of the microscopic origin of ferroelectric order in  $\text{Fe}_3\text{O}_4$ , Yamauchi *et al.* [98] studied the differences between the monoclinic centrosymmetric  $P2/c$  and the non-centrosymmetric  $Cc$  structures using first-principles calculations. They conclude that the spontaneous ferroelectricity in  $\text{Fe}_3\text{O}_4$  is a result of the combination of site-centered charge ordering and modulation in Fe—Fe bond lengths, as argued in [42]. Such situation can be better understood with the help of figure 3.3, where the difference in charge-ordering between the two monoclinic space groups is depicted. Such difference breaks the space inversion symmetry and allows the creation of ferroelectric polarization. The accompanied modulation in the Fe—Fe bond lengths results in a displacement of  $\sim 0.1$  Å for some iron ions, creating a net polarization moment along the monoclinic  $b$ -axis [42].

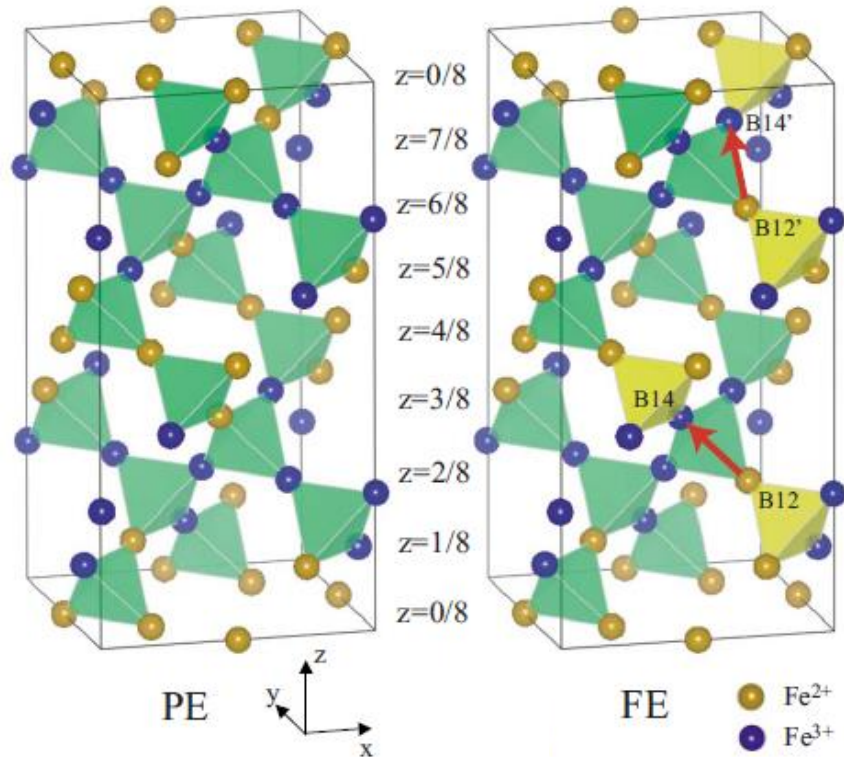


Figure 3.3: Iron ions positions in the paraelectric monoclinic  $P2/c$  (left) and the ferroelectric  $Cc$  (right) structures. The red arrows indicate the direction of electric dipole moments created by charge ordering [98].

In this chapter, we present a brief summary of the magnetic characterization work done on gadolinium ( $Gd^{64}$ ) doped  $Fe_3O_4$ . We follow by detailed presentation of the dielectric and ferroelectric characterization carried out on undoped and Gd-doped  $Fe_3O_4$  nanoparticles. The choice of Gd as a dopant is based on its use in magnetic resonance imaging (MRI) as a contrast agent [99, 100]. On the other hand, the use of  $Fe_3O_4$  nanoparticles in cancer treatment via induced hyperthermia is being established [11, 101]. It has been found that  $Fe_3O_4$  nanoparticles doped with 2% Gd show a specific power adsorption rate (SAR) that is four-times higher than undoped  $Fe_3O_4$  [102]. Moreover, the use of magnetoelectric nanoparticles in drug delivery has been studied in vitro [103], where the application of a small amplitude (10 Oe) oscillating magnetic field was used for on-demand release of anti-HIV drug. In general, the use of

nanoparticles in drug delivery is promising for their ability to cross the highly selective blood-brain barrier [104]. From physics point of view, first-principle calculations suggest Gd to prefer octahedral site occupancy when introduced as a dopant to  $\text{Fe}_3\text{O}_4$  inverse spinel environment [105]. Considering the reported ionic radii of  $\text{Gd}^{3+}$  and  $\text{Fe}^{3+}$  in octahedral coordination, 0.938 Å and 0.645 Å respectively [106], one expects Gd dopants to induce high chemical pressure on  $\text{Fe}_3\text{O}_4$  structure.

## **3.2 EXPERIMENTS AND RESULTS**

### **3.2.1 NANOPARTICLES PREPARATION AND CHARACTERIZATION**

Undoped  $\text{Fe}_3\text{O}_4$  samples were prepared via a standard co-precipitation chemical route, starting with the appropriate stoichiometric ratios of iron(II) chloride and iron(III) chloride. The Gd dopant was introduced to substitute iron  $\text{Fe}^{3+}$  by adding the proper quantity of gadolinium(III) chloride. The target stoichiometry is  $(\text{Fe}^{2+}\text{O})(\text{Fe}_{2-x}^{3+}\text{Gd}_x\text{O}_3)$ , with  $x = 0.03$ , 0.075 and 0.15, which correspond to Gd:Fe ratios of 1%, 2.5% and 5% respectively. More details on the preparation process are presented in reference [99]. The samples will be referred to herein as Gd-0, Gd-1, Gd-2.5 and Gd-5 in the order of increasing Gd content.

The  $\text{Fe}_3\text{O}_4$  spinel structure was confirmed by recording XRD diffraction pattern for the undoped and doped samples, for which the formation of secondary phases is also ruled out within the limits of the XRD sensitivity. The data show a monotonic increase in crystallite size with increasing Gd content, as estimated by Scherrer formula [107]. EDS analysis indicate that the actual doping percentages are 1.3%, 3.0% and 5.5%; slightly higher than what was aimed for.

### **3.2.2 MAGNETIC DATA (SUMMARY)**

Detailed magnetic analysis presented in [99] confirm the superparamagnetic nature of the synthesized nanoparticles, with the Blocking temperature falling in the range between 150 K and

200 K for different compositions. The saturation magnetization at room temperature, as well as the anisotropy constant  $K$ , showed a uniform decrease with increasing Gd content. The anisotropy constant  $K$  is defined through equation 3.1:

$$E = K \sin^2 \theta \quad (3.1)$$

Where  $E$  is the difference between the magnetic energies (per unit volume) needed to achieve saturation along the crystal's easy and hard axes, and  $\theta$  is the angle between the direction of magnetization and the easy direction.

### 3.2.3 DIELECTRIC PROPERTIES

The temperature dependence of the dielectric constant is determined by recording the capacitance of cold-pressed pellets made of the synthesized nano-powders. Silver paste is applied to both sides of disk-shaped pellets, to which gold wires are attached, creating a parallel-plate capacitor setting. The driving AC signal delivered to the pellets is generated using HP 4284A Precision LCR meter, controlled by a LabVIEW program to monitor and record the data. The temperature control is provided by Quantum Design Physical Property Measurement System (PPMS). In this set of measurements, we report the temperature dependence of the relative dielectric constant ( $\epsilon_r$ ) and the loss tangent ( $\tan \delta$ ), which is defined by equation 3.2:

$$\tan \delta = \frac{\epsilon''(\omega)}{\epsilon'(\omega)} \quad (3.2)$$

Where  $\epsilon'$  and  $\epsilon''$  are the real and imaginary parts of the material's dielectric constant. The loss tangent is in general written as the sum of two parts: losses due to conduction and losses due to polarization [108]. Also, we note the relation between  $\epsilon'$  and  $\epsilon_r$ :  $\epsilon' = \epsilon_r \times \epsilon_0$ , where  $\epsilon_0$  is the permittivity of free space.

The dielectric behavior of different samples is presented in figures 3.4. The monotonic rise in the loss tangent at higher temperatures (i.e.:  $T > 200$  K) is due to increase in the number

and root mean square speed of the thermally activated Fermi electrons. The high temperature feature observed in the Gd-0 data coincides with the ice-water transition ( $\sim 273$  K) and could be originating from adsorbed water molecules on the pellet's surface [109]. The most interesting feature in figure 3.4 is perhaps the broad peaks observed in dielectric loss, whose positions shift with temperature. Such peaks are a signature of relaxor ferroelectrics, confirming the ferroelectric nature of the Gd-doped samples. On the same note, the dielectric loss peaks' heights being frequency independent is indicative of Debye relaxation mechanism.

In Debye process, the relaxation mechanism stems from the conformation of molecular dipoles, whose charge centers are the iron (or gadolinium) and oxygen ions in case of  $\text{Fe}_3\text{O}_4$ . Since this dipolar rearrangement is driven by thermal agitations, the needed activation energy ( $U$ ) is estimated with the help of Arrhenius equation [110]:

$$f_p = f_0 e^{-U/kT} \quad (3.3)$$

Where  $f_p$  is the loss peak frequency,  $f_0$  is a constant,  $k$  is Boltzmann's constant and  $T$  is the temperature. The semi-log plots in figure 3.5 were generated after extracting the curve frequencies and the corresponding peak temperatures from figure 3.4. The activation energy is found to increase from 0.1 eV for undoped  $\text{Fe}_3\text{O}_4$  to  $\sim 0.12$  eV for the Gd-5 sample. This increase is expected as a result of substituting some Fe transition metal ions with the heavier Gd lanthanide ions.

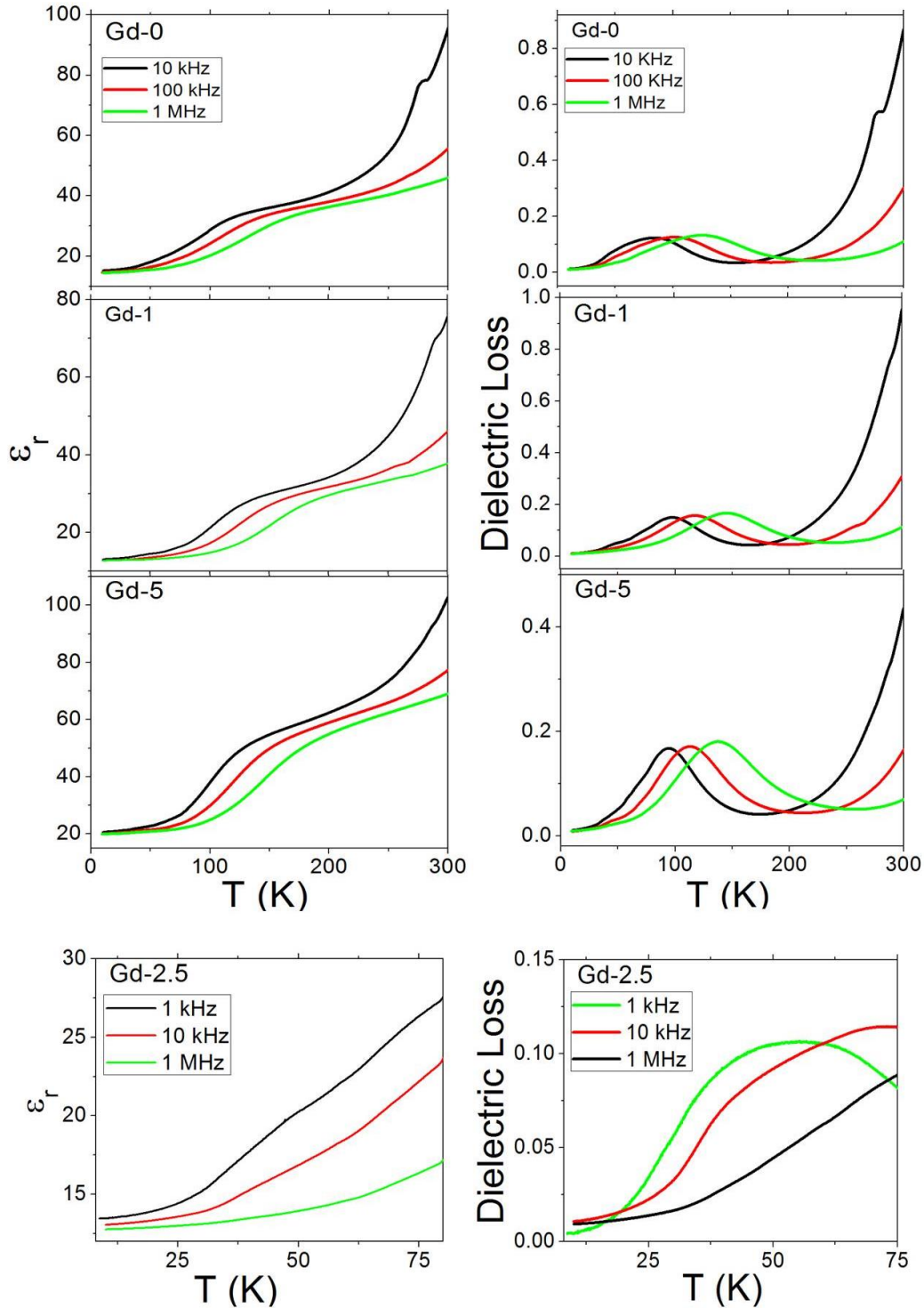


Figure 3.4: Change in relative dielectric constant ( $\epsilon_r$ ) and dielectric loss of  $\text{Fe}_3\text{O}_4$  and Gd-doped  $\text{Fe}_3\text{O}_4$  nanoparticles versus temperature. The data for Gd-2.5 sample was recorded only up to 80K.

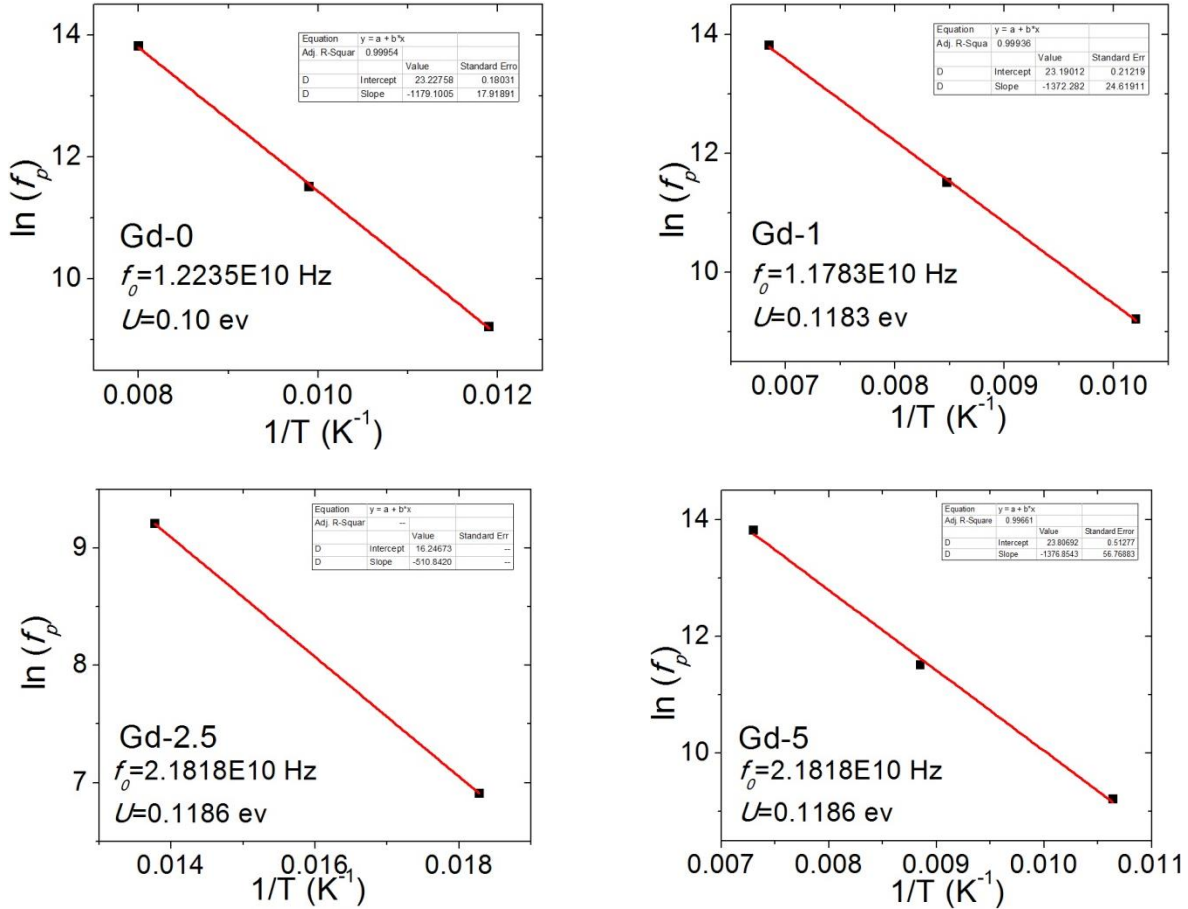


Figure 3.5: Semi-log straight line fits of dielectric loss peak frequencies vs temperature reciprocal for pure and Gd-doped  $\text{Fe}_3\text{O}_4$ .

We also report the frequency dependence of the dielectric constant and loss on Gd-0 and Gd-5 pellets at room temperature (i.e.: 300 K) in figure 3.6. The data were recorded only between 10 kHz and 1 MHz because the dielectric loss of the Gd-0 sample was higher than 10 below this range, which made it outside the measurable range of the used LCR meter. The presented curves exhibit a steady non-linear decrease in both quantities for the two samples, which is in part due to aging effects –triggered by reorientation of defect dipoles– usually observed in ferroelectrics [111]. Such effects cause the measured capacitance to depend on the time waited before commencing the data acquisition process, which is why the values reported in figure 3.6 are discrepant from those seen in the temperature dependent plots (figure 3.4). Besides

the time drift effect, the decrement in dielectric constant and loss values is described as the ‘universal’ dielectric response [110, 112], and is attributed to slowly hopping mobile charge carriers.

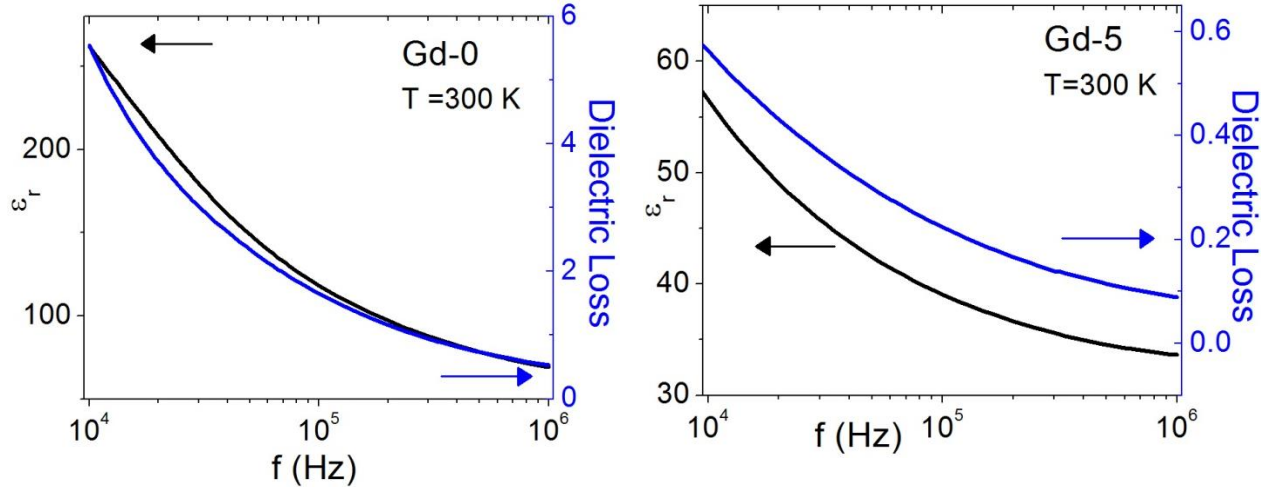


Figure 3.6: Frequency dependence of the dielectric constant (left axes) and dielectric loss tangent (right axes) for Gd-0 and Gd-5 samples at 300 K.

### 3.2.4 MAGNETO-DIELECTRIC COUPLING

The effect of magnetic field on the dielectric properties was studied. In general, spin-charge coupling is possible in systems which are simultaneously magnetic and piezoelectric due to the strain induced by magnetic anisotropy. Consider the free energy ( $F$ ) expansion in terms of ferroelectric polarization ( $P$ ) and magnetization ( $M$ ) [84]:

$$F = \gamma P^2 M^2 + (\text{other terms}) \quad (3.4)$$

The ‘other terms’ are generally forbidden due to symmetry considerations [84, 113]. The scalar  $P^2 M^2$  term has been used to explain magneto-electric behavior in a number of systems (see [114] for example).

For the  $\text{Fe}_3\text{O}_4$  set of samples at hand, the dielectric constant and loss were recorded as a function of magnetic field at a number of fixed temperature values. LabVIEW interface was used



to record the data while providing the needed control over the PPMS and LCR meter. In an attempt to eliminate the steady time dependent decrease in capacitance caused by aging effects, the magnetic field was swept in steps rather than continuously. That is, the magnetic field strength was held constant at the desired value before recording the capacitance and loss for one minute. The capacitance/loss raw data was then averaged after subtracting a linear background. The process was repeated at different magnetic field values, and the whole routine was carried out at  $T = 10$  K, 50 K and 300 K. The averaged magneto-dielectric data are presented in figure 3.7.

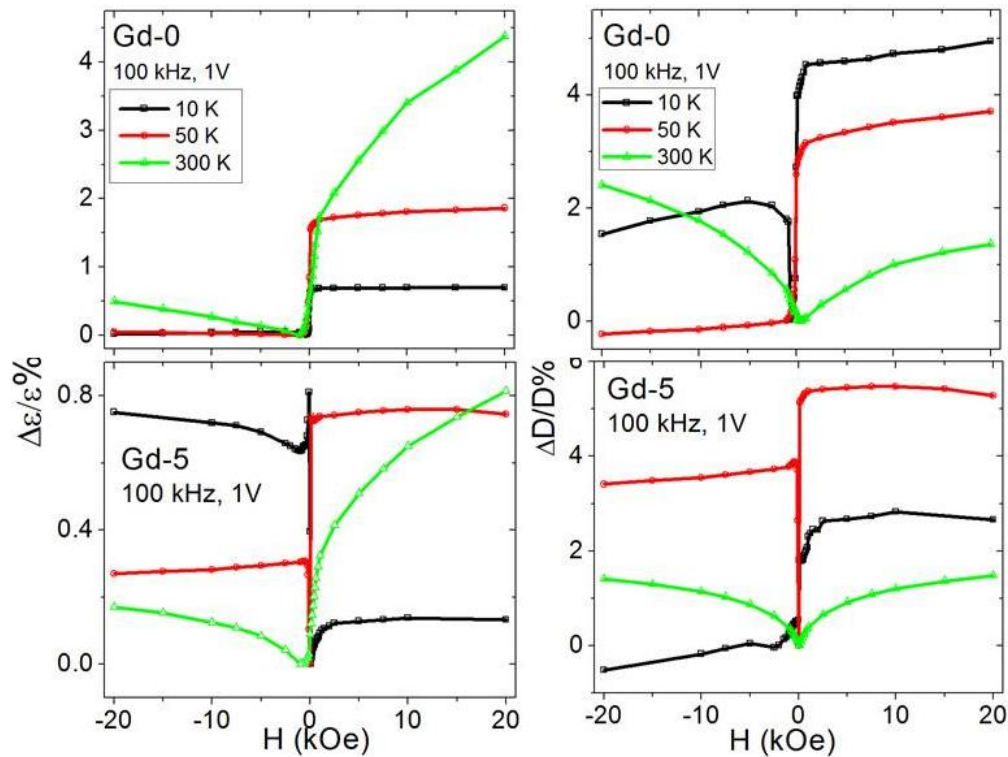


Figure 3.7: Relative change in dielectric constant and dielectric loss tangent as a function of magnetic field for Gd-0 and Gd-5 samples.

The quantities shown on the y-axes in figure 3.7 are the percent discrepancies in the dielectric constant and loss; with the reference values  $\epsilon_0$  and  $D_0$  are chosen as the dielectric constant and loss tangent –respectively– at  $H=0$  Oe. In spite of the step-wise routine followed,

the obtained data are still influenced by time drift effects to some extent, observed in the skewness of some plots. In addition, the data also involve spurious magneto-capacitive signals [84], making it difficult to comment on the significance of the obtained numerical values. It can be noted, though, that the asymmetry in coupling curves could be either due to magnetostriction or due to magnetic hysteresis. While the reported  $\text{Fe}_3\text{O}_4$  magnetostriction values in literature [115] are typically in the order of  $10^{-4}\%$ , which is three orders of magnitude smaller than the observed change in figure 3.7, magnetite nanoparticles have been recently reported to exhibit giant magnetostriction [116] in the order of  $10^{-1}\%$ . With the probability of such immense change in the pellets' thickness in picture, it is not possible to explain the physics behind figure 3.7 plots.

### **3.2.5 FERROELECTRIC PROPERTIES**

We attempt to measure the ferroelectric polarization moment for Gd-0 and Gd-5 samples by integrating the recorded pyrocurrent signal with respect to time. The samples were cooled from 150 K down to 10 K under a poling voltage of 100 V, which corresponds to an electric field in the order of kV/cm considering the thicknesses of the used pellets. Higher voltage values could not be applied as the Gd-0 sample had a relatively low resistivity at 150 K. A linear background was subtracted from the pyrocurrent signal prior to integrating with respect to time. The obtained polarization moments, shown in figure 3.8, are two orders of magnitude smaller than previously reported values [93, 117, 118]. We attribute this in part to the inherent defects in our pressed nanoparticle pellets samples, compared to thin films [93, 117] and single crystals [118] which, by definition, have better crystallinity. Moreover, polarization measurements carried out on nanoparticles are usually averaged on the randomly oriented crystallites, in contrast to thin films which have preferred growth orientation.

The calculated polarization moment for the Gd-5 sample is more than double that of pristine  $\text{Fe}_3\text{O}_4$ . This is ascribed to  $\text{Gd}^{3+}$  having a larger ionic radius compared to  $\text{Fe}^{3+}$ , which leads to effectively decreasing the bond length between the cation and the oxygen anion, hence increasing the absolute value of ferroelectric lattice distortions.

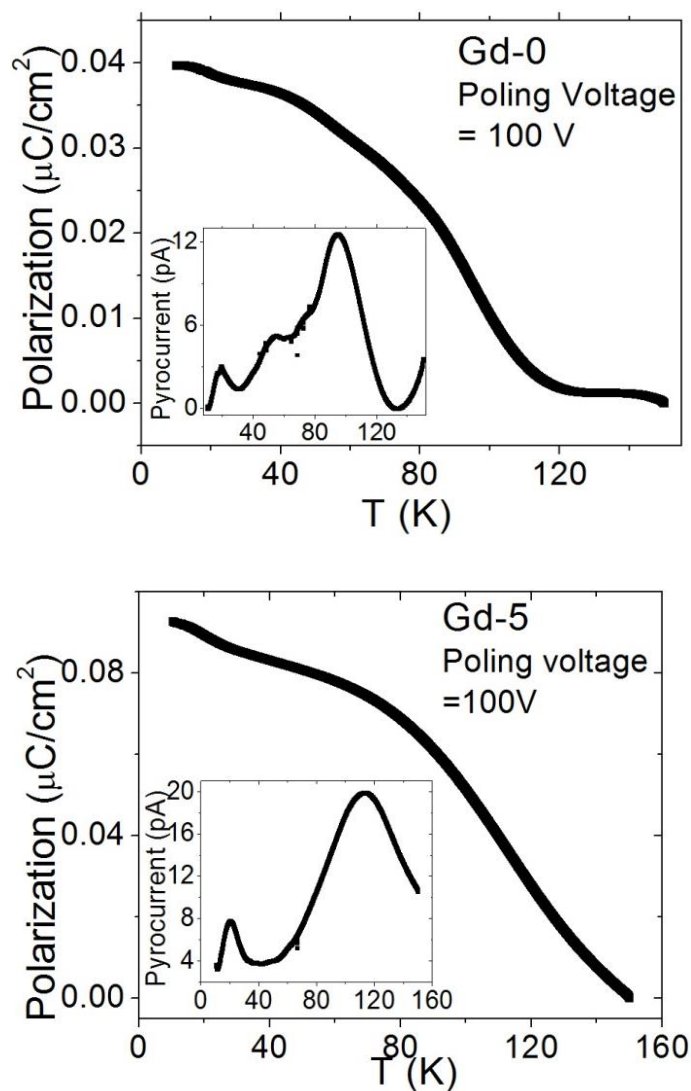


Figure 3.8: Calculated ferroelectric polarization moment for Gd-0 and Gd-5. The measured pyrocurrent signals are included in the insets.

### 3.2.6 TEMPERATURE DEPENDENT XRD AND HEAT CAPACITY

It was discussed above how the charge ordering mechanism needed for generating ferroelectricity is triggered by Verway transition. With this motivation, we investigate the structural changes around Verway transition by recording the XRD diffraction pattern at different temperatures in that vicinity for  $\text{Fe}_3\text{O}_4$ . The obtained data are presented in figure 3.9. While all the major peaks were indexed to  $\text{Fe}_3\text{O}_4$ , crystalline NaCl was also identified, with the corresponding peaks marked by ‘\*’ in figure 3.9. The NaCl impurity is a result of using sodium hydroxide to trigger precipitation of magnetite during the preparation process. It should be noted that the spectra in figure 3.9 are obtained for a different batch than that was used in other measurements.

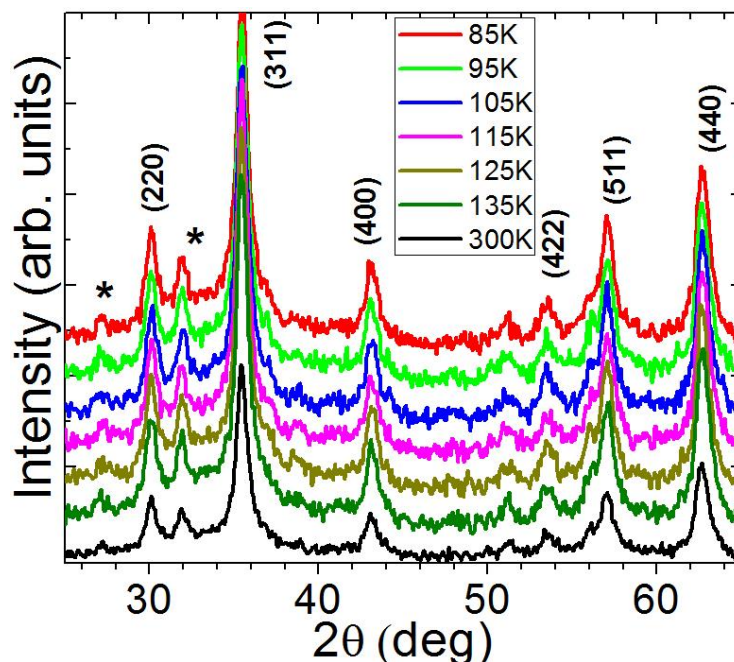


Figure 3.9: XRD patterns recorded at different temperatures in the vicinity of Verway transition for  $\text{Fe}_3\text{O}_4$ . The curves are vertically displaced for clarity.

The reported theoretical calculations [94] inform us of an expected Bravais lattice change accompanying Verway transition ( $\sim 120$  K). Such change will definitely exhibit itself in XRD

spectra as a change in the peaks' pattern. Surprisingly, no difference is seen upon crossing 120 K in our data. We propose the reason behind this to be the diminished nature of lattice distortion ( $\sim 0.1 \text{ \AA}$ ) accompanying the long range ferroelectric order. The distortion is too small to have a noticeable effect on XRD peak positions.

Finally, the heat capacity at constant pressure was measured for sample Gd-0 in Quantum Design PPMS. For this purpose, a few milligrams of the sample were mixed with an equal mass of silver powder and pressed into a disk-shaped pellet. Silver was used to ensure proper thermal conductivity throughout the pellet. Details on the heat capacity measurement routine can be found in Ref. [119].

The molar heat capacity values obtained for sample Gd-0 –shown in figure 3.10– agree with earlier reported data [118]. However, there's no clear signature of any phase transition around 120 K. This observation coincides with earlier measurements on nanocrystalline magnetite [120], where the absence of heat capacity anomaly was attributed to Verwey transition being particle-size dependent. It has been reported also [121] that the sample's stoichiometry affects the clarity by which the transition is manifested in magnetic remanence curves.

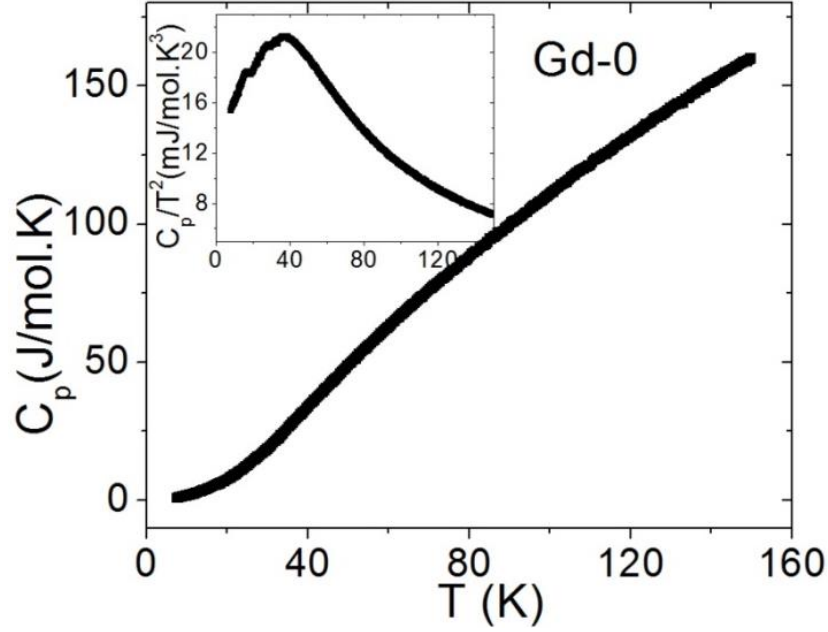


Figure 3.10: Heat capacity of sample Gd-0. The inset shows a  $\frac{C}{T^2}$  vs  $T$  plot.

For metal oxides, the heat capacity is generally given by:

$$C = aT + bT^3 \quad (3.5)$$

Where  $a$  and  $b$  are proportionality constants. The linear term represents electronic contribution, and is exhibited only in conductors. The  $\sim T^3$  term, on the other hand, is due to phonons. It is noticed in the inset of figure 3.10 that  $\frac{C}{T^2}$  vs  $T$  is not a straight line, as expected from equation 3.5. Instead, the curve peaks around 40 K, which indicates contribution from the ferroelectric phonon modes. The plot also shows slight deviation from linearity above 40 K, a behavior which is due to magnon (spin wave) excitations [118].

### 3.3 CONCLUSIONS AND FUTURE WORK

We investigated the dielectric and ferroelectric properties of Gadolinium-doped  $\text{Fe}_3\text{O}_4$  nanoparticles. While  $\text{Fe}_3\text{O}_4$  nanoparticles have been utilized in cancer treatment research via

hyperthermia, Gd-based compounds also find popularity as MRI contrast agents. In addition, magnetoelectric nanoparticles are within the research interests for drug delivery applications.

$\text{Fe}_3\text{O}_4$  is a multiferroic material, with the ferroelectric property attributed to long-range charge ordering among the octahedral *B*-sites in the magnetite inverse spinel lattice. Partial substitution of  $\text{Fe}^{3+}$  with  $\text{Gd}^{3+}$  aims to induce chemical pressure, based on the considerable difference in ionic radii. The formation of secondary phases was ruled out based on XRD spectra, and the precise Gd compositions were estimated using EDS technique.

Increasing Gd content was linked to a decrease in saturation magnetization and the magnetic anisotropy constant. On the other hand, Debye activation energy –estimated from temperature dependent dielectric loss plots– was found to be higher in samples with more Gd content. Also, frequency dependent dielectric constant and loss showed a common dielectrics behavior of charge carriers hopping, besides revealing a time dependent drift which is characteristic to ferroelectrics and is caused by the reorientation of defect dipoles.

The magneto-dielectric plots told us a little about the nature of magnetoelectric coupling in this system because of the persistence of aging effects, which manifested itself in significant skewness. Furthermore, spurious magneto-capacitive signals also affected the outcome of our measurements. The magneto-dielectric plots showed some asymmetry, owing to magnetostriction and magnetic hysteresis.

The ferroelectric polarization moment for the undoped and 5%Gd-doped were calculated by integrating the pyrocurrent signal. The data showed an increase in polarization moment upon doping, although the obtained values were two orders of magnitude smaller than reported on thin films and single crystals because of being averaged on the randomly oriented crystallites. The increase in polarization moment was attributed to the larger ionic size of  $\text{Gd}^{3+}$  leading to

enhanced lattice distortions. Finally, a contribution of phonon modes associated with the ferroelectric order was detected in specific heat capacity data of undoped  $\text{Fe}_3\text{O}_4$ .

Overall, a complete understanding of the ferroelectric order mechanism in  $\text{Fe}_3\text{O}_4$  is yet to be understood. Our structural characterization attempts (XRD at different temperatures) were not conclusive about the nature of structural transition taking place at Verwey transition, which is possibly due to the sample's stoichiometry being unbalanced. A step towards a better understanding of this system will be to have a better control on the stoichiometry while introducing the dopants.

On the other hand, while studying nanoparticles is attractive for the herein introduced biomedical applications, their inherent structural defects are unavoidable. A better understanding of the physics behind ferroelectricity in this system requires preparing higher quality samples; sputtered thin films and single crystals will be considered.



## **CHAPTER 4: MAGNETO-DIELECTRIC COUPLING IN POLYVINYLIDENE FLUORIDE (PVDF)-BASED NANOCOMPOSITE FILMS**

### **4.1 OVERVIEW AND PREVIOUS WORK**

There has been an increase in the research activity aiming to design suitable magneto-electric systems for different room temperature applications. Among the materials being the focus of a significant number of research articles in this concern is Polyvinylidene Fluoride (PVDF), which is produced by polymerization of  $(\text{CH}_2\text{—CF}_2)$  monomers.

PVDF, which is commercially available under other names (e.g.: Foraflon, Kynar, Hylar) fits in a wide range of applications, owing to its corrosion resistance, thermal stability (melting point:  $170\text{ }^\circ\text{C}$ ) and mechanical strength [122] (Young's Modulus: 2.4 GPa). In addition, reported piezoelectricity in PVDF [123] widened the scope of possible applications. With its lightweight (density:  $1.78\text{ g/cm}^3$ ), flexibility and ability to form self-standing films, PVDF is a potential candidate for different biomedical sensors [124].

The vinylidene difluoride monomer shown in figure 4.1 has a natural electric polarity; due to the difference in electronegativity between the hydrogen and fluorine ions. Instead of forming amorphous solid structure, PVDF polymer chains tend to arrange in semi-crystalline configurations, where some chains will retain long range alignment, while others are trapped due to entanglement. Five different crystalline forms have been reported for PVDF so far [125], which are defined based on the orientation of successive monomers on the polymer chain.

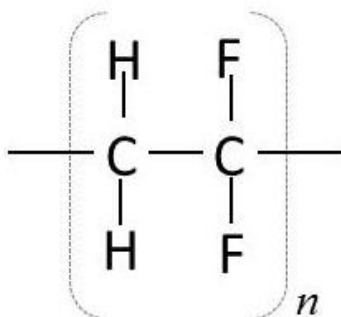


Figure 4.1: Structure of vinylidene difluoride, the PVDF monomer.

The different orientations (formally called conformations) arise due to different possible orientations of the two hydrogen atoms and the two fluorine atoms with respect to each other around the C—C bond. When the hydrogen and fluorine pairs are farthest from each other, the conformation is called ‘*trans*’. On the other hand, ‘*gauche*’ conformation denotes a situation where the hydrogen and fluorine pairs are closest to each other. The different crystalline forms of PVDF represent different possible iterations of *trans* (T) and *gauche* (G) conformations along the polymer chain.

The two most common crystallographic phases of PVDF are shown in figure 4.2. The  $\alpha$ -phase, shown in figure 4.2(a), is the most stable phase [126], and is characterized by the polymeric chain having the (TG<sup>+</sup>TG<sup>-</sup>) conformation. As a result of this alternation, the molecular dipoles end up being anti-parallel, resulting in a non-polar structure. The polar  $\beta$ -phase, on the contrary, has the (TTTT) conformation, resulting in a net non-zero dipole moment that is perpendicular to the polymer chain’s axis [127]. Other known polymorphs of PVDF include the polar  $\gamma$ - [128] and  $\delta$ - [129] phases, and the anti-polar  $\epsilon$ -phase [125].

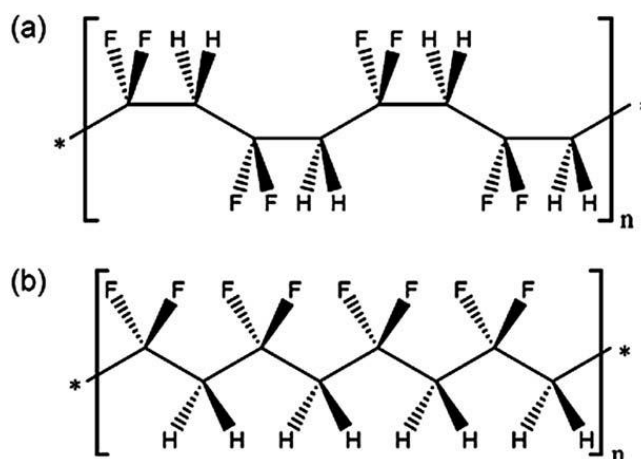


Figure 4.2: (a) The non-polar  $\alpha$ -PVDF phase and (b) the polar  $\beta$ -PVDF phase [127].

The piezoelectricity and the non-zero dipole moment of  $\beta$ -PVDF make it the most desirable phase for technological applications. As a result, researchers aim to come up with techniques to convert from  $\alpha$ - to  $\beta$ -PVDF with higher ease and efficiency. For instance, the effect of using different solvents on the polymorphism of grown PVDF films has been reported [130]. In other instances, it was found that PVDF favors nucleation in the polar  $\beta$ -phase upon addition of some nanofillers [131-133]. In particular, a significant number of reports have been dedicated to studying the effect of loading PVDF with zinc oxide nanoparticles [134-137], where an enhancement in the optical and dielectric properties of PVDF has been reported. Another well studied nanofiller is reduced graphene oxide (RGO), which is obtained by reduction of graphene oxide (exfoliated graphite oxide). RGO attracts attention of materials scientists due to its high theoretical specific surface area ( $2600 \text{ m}^2/\text{g}$ ) and high electric and thermal conductivities [138]. An earlier study on RGO-loaded PVDF has shown an increase in its dielectric constant [139].

In this chapter, we report the effect of loading PVDF- $\text{Fe}_3\text{O}_4$  hybrid films with RGO and ZnO on the dielectric and ferroelectric properties. Magnetic  $\text{Fe}_3\text{O}_4$  nanoparticles are added as fillers to introduce ferromagnetism and induce magneto-dielectric coupling in composite films.

We also study the effect of using graphene oxide on PVDF-Fe<sub>3</sub>O<sub>4</sub> films. At the end, we present the results of using surface modified nickel nanoparticles and barium hexaferrite –non-simultaneously– on PVDF matrix.

## **4.2 EXPERIMENTAL WORK**

### **4.2.1 PVDF-Fe<sub>3</sub>O<sub>4</sub> HYBRID FILMS WITH REDUCED GRAPHENE OXIDE (RGO) AND ZINC OXIDE (ZnO) NANOFILLERS [140]**

Composite films were prepared by solvent casting method, where calculated amounts of the Fe<sub>3</sub>O<sub>4</sub>, RGO and ZnO nanofillers were mixed with PVDF solution in dimethyl formamide (DMF) at room temperature. The fillers were prepared beforehand; Fe<sub>3</sub>O<sub>4</sub> was synthesized by co-precipitation of Fe<sup>2+</sup> and Fe<sup>3+</sup> in alkaline medium, ZnO nanorods were grown by solvothermal method and RGO was prepared by reduction of commercially available graphene oxide via sonication in DMF and hydrazine hydrate. The nanofillers constituted 5% by weight of PVDF. The mixture was then poured on a glass slide and heated at 80 °C to evaporate DMF. The dried films of PVDF, PVDF-RGO, PVDF-RGO-Fe<sub>3</sub>O<sub>4</sub> and PVDF-RGO-Fe<sub>3</sub>O<sub>4</sub>-ZnO could then be peeled off glass and had a thickness of ~50 μm.

The structure and morphology of the prepared films were studied by X-ray diffraction (XRD), Raman spectroscopy, Fourier Transform Infrared Spectroscopy (FTIR), Scanning electron microscopy (SEM) and Transmission electron microscopy (TEM). The dielectric and ferroelectric measurements were carried out in parallel plate capacitor configuration using an Agilent 4284A LCR meter and an aixACCT TF Analyzer-2000.

The X-ray diffraction patterns of the prepared films are shown in figure 4.3, along with the patter of a commercial PVDF film for reference. Commercial PVDF consists predominantly of  $\alpha$ -phase, with the peaks at  $2\theta = 17.6^\circ$ ,  $18.4^\circ$  and  $19.9^\circ$  and  $26.6^\circ$  represent reflections from

(100), (020), (110) and (021) respectively. The films prepared in this study show mainly a broad peak around  $2\theta = 20.6^\circ$ , corresponding to (110) peak [141, 142]. The broadening in the films' peaks implies the presence of semi-crystalline mixtures of  $\alpha$ -,  $\beta$ - and  $\gamma$ -phases. Characteristic peaks of  $\text{Fe}_3\text{O}_4$  and RGO nanoparticles are weak and just lead to some broadening, owing to the small concentrations added (5%). On the contrary, ZnO nanorods possess a highly crystalline nature, and corresponding peaks are easily detected, indicated by '\*' in figure 4.3.

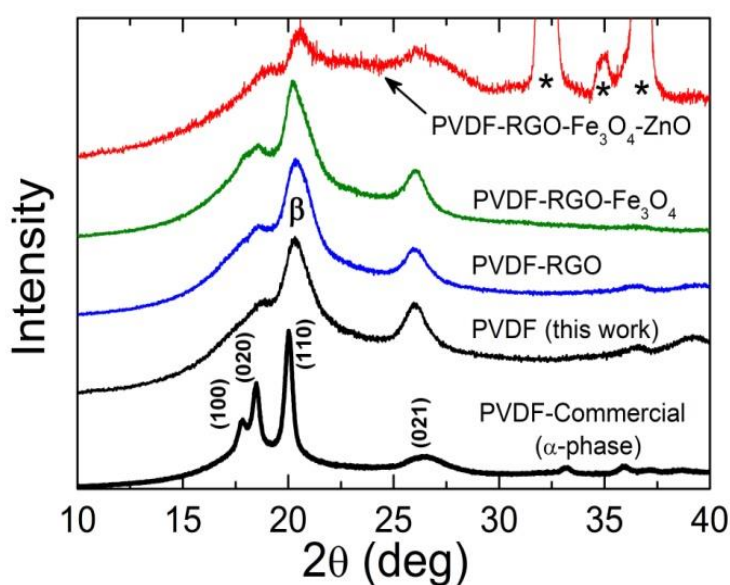


Figure 4.3: XRD patterns of commercial PVDF film, prepared pristine PVDF and composite films.

The average size of the  $\text{Fe}_3\text{O}_4$  nanoparticles is estimated from TEM images to be  $\sim 12$  nm. Similarly, ZnO nanorods are found to be  $\sim 10$   $\mu\text{m}$  in length on average. Low resolution SEM images of the composite films (figure 4.4) show that PVDF film is smooth and dense with no visible voids, whereas nanoparticle-loaded PVDF composite films have rough surfaces with granular particles distributed homogeneously in the film.

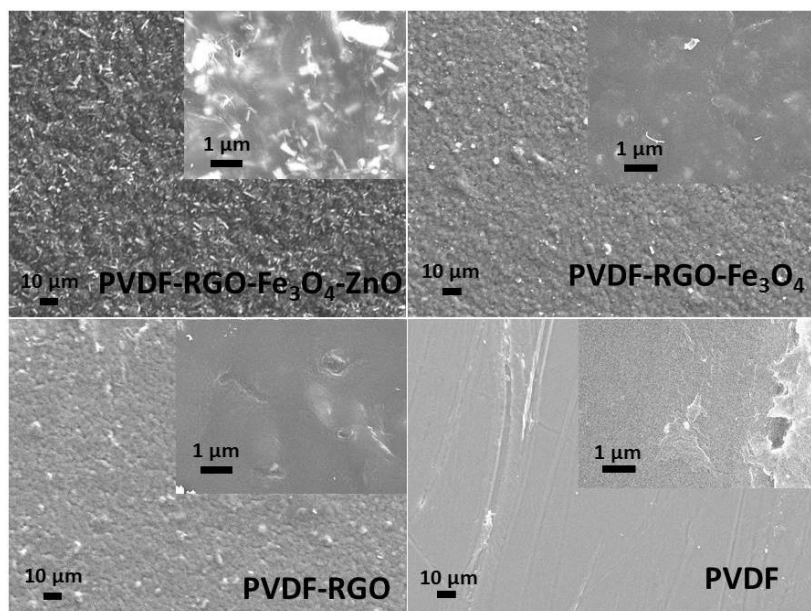


Figure 4.4: Low resolution SEM images for PVDF films.

The Raman spectra shown in figure 4.5(a) are used to estimate the relative quantities of  $\alpha$ - and  $\beta$ -phases in the prepared pristine PVDF film. The spectra of PVDF films loaded with nanofillers are dominated by D- and G- bands characteristic of RGO [143], making the weak PVDF characteristic bands barely discernible. On the other hand, the Raman spectra of pure PVDF samples show distinct bands. Specifically, the bands observed at  $795\text{ cm}^{-1}$  and  $839\text{ cm}^{-1}$  correspond to  $\alpha$ - and  $\beta$ -phases [144] and can be used to quantify those phases in PVDF film. We have estimated the relative amounts of  $\alpha$ - and  $\beta$ -phases in the solvent cast PVDF film prepared for this study and in the commercial film, by fitting the Raman spectra in the  $700\text{-}950\text{ cm}^{-1}$  region with Lorentzian-Gaussian line profiles (figure 4.5(b)). Our estimates yield  $\alpha$ - and  $\beta$ -percentages of 18% and 82% respectively for our PVDF film, whereas the estimated numbers for the commercial film are  $\alpha$ : 74% and  $\beta$ : 26%. Thus, the solvent cast film is  $\beta$ -phase predominant. Since the other samples are dark colored (i.e.: show high absorbance in the visible region) they tend to burn when incident laser power is increased in an attempt to obtain good Raman spectra

outside the RGO D- and G-band regions. Therefore, we used FTIR spectra to estimate the phase composition of those films.

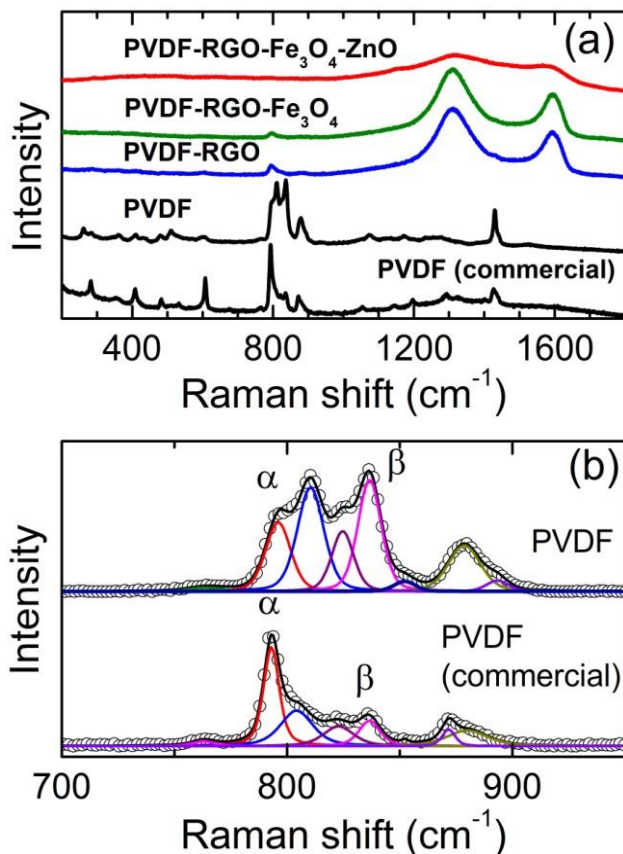


Figure 4.5: (a) Raman spectra for the PVDF films prepared for this study and the commercial PVDF film. (b) Lorentzian-Gaussian peak fits to the PVDF films spectra.

The FTIR spectra –recorded in attenuated total reflection setting- of the studied PVDF samples are shown in figure 4.6. The commercial PVDF film shows the expected bands of the  $\alpha$ -phase at 762 and 795 cm<sup>-1</sup>, while the pure PVDF film prepared for this study shows mainly the  $\beta$ -phase bands at 840 and 878 cm<sup>-1</sup> [145-147] with a minor fraction of  $\alpha$ . The bands at 762 and 840 cm<sup>-1</sup> were used in estimating the fractional composition in the samples utilizing equation 4.1 [148]:

$$f_{\beta} = \frac{A_{\beta}}{1.3A_{\alpha} + A_{\beta}} \quad (4.1)$$

Where  $A_{\alpha}$  and  $A_{\beta}$  are the IR absorbances at 762 and 840  $\text{cm}^{-1}$ . The fractions of  $\beta$ -phase determined for different samples are listed in table 4.1. Both Raman and IR spectral analyses yield the same value for the fraction of  $\beta$ -phase in the commercial as well as the solvent cast PVDF films, implying either technique can be used to determine the fraction of the  $\beta$ -phase in these films.

<b>Film</b>	<b>Fraction of <math>\beta</math>-phase (%)</b>	
	From IR	From Raman
PVDF-Commercial	27	26
PVDF	81	82
PVDF-RGO	77	—
PVDF-ZnO (spectrum not shown)	58	—
PVDF-RGO- $\text{Fe}_3\text{O}_4$	53	—
PVDF-RGO- $\text{Fe}_3\text{O}_4$ -ZnO	49	—

Table 4.1: PVDF composite films and their  $\beta$ -phase fractions.

It is found that the PVDF and PVDF-RGO films possess the highest  $\beta$ -phase percentage ( $\approx 80\%$ ), whereas films which carry  $\text{Fe}_3\text{O}_4$  and ZnO nanofillers have the lowest  $\beta$  content ( $\approx 50\%$ ). Such decrease in  $\beta$ -phase content upon addition of nanofillers is contrary to earlier observations reported in literature [149]. It has been shown that the dispersion of nanoparticles in polymer composites is enhanced when polymer films are confined to nanometer size thickness [150]. However, in the present study the self-standing film thickness is large ( $\sim 50 \mu\text{m}$ ) and the nanoparticles may not be well dispersed, forming larger aggregates. The inclusion of  $\text{Fe}_3\text{O}_4$  and



ZnO nanofillers will likely induce crystallographic texture, disrupting the all-*trans* planar zigzag conformation of the PVDF backbone in the  $\beta$ -phase leading to an increase in the  $\alpha$ -phase in the vicinity of the nanoparticles.

The dielectric, magnetic and ferroelectric characterization data are collectively shown in figure 4.6. The dielectric constant dependence on frequency is plotted in figure 4.6(A), where the nanofillers loaded films show enhance dielectric constant compared to the pure PVDF film. Since the polymer matrix and the inorganic fillers have different dielectric constant, a large number of charge carriers accumulate on these interfaces leading to strong Maxwell-Wagner-Sillars (MWS) polarization [139]. On the other hand, films loaded with  $\text{Fe}_3\text{O}_4$  show a reduced dielectric constant compared to PVDF-RGO and PVDF-ZnO. We attribute this to increased electrical conduction in  $\text{Fe}_3\text{O}_4$  aggregates in the PVDF composite films containing  $\text{Fe}_3\text{O}_4$ . The PVDF-RGO film, which contains a high percentage of  $\beta$ -phase, shows a lower dielectric loss (figure 4.6(E)) and a higher dielectric constant compared to pure PVDF and other composite films. This results in a higher electrical polarization as described below. Generally, the dielectric loss arises from several contributions, including direct current conduction, MWS relaxation and the Debye loss factor:

$$\delta = \delta_{DC} + \delta_{MW} + \delta_D \quad (4.2)$$

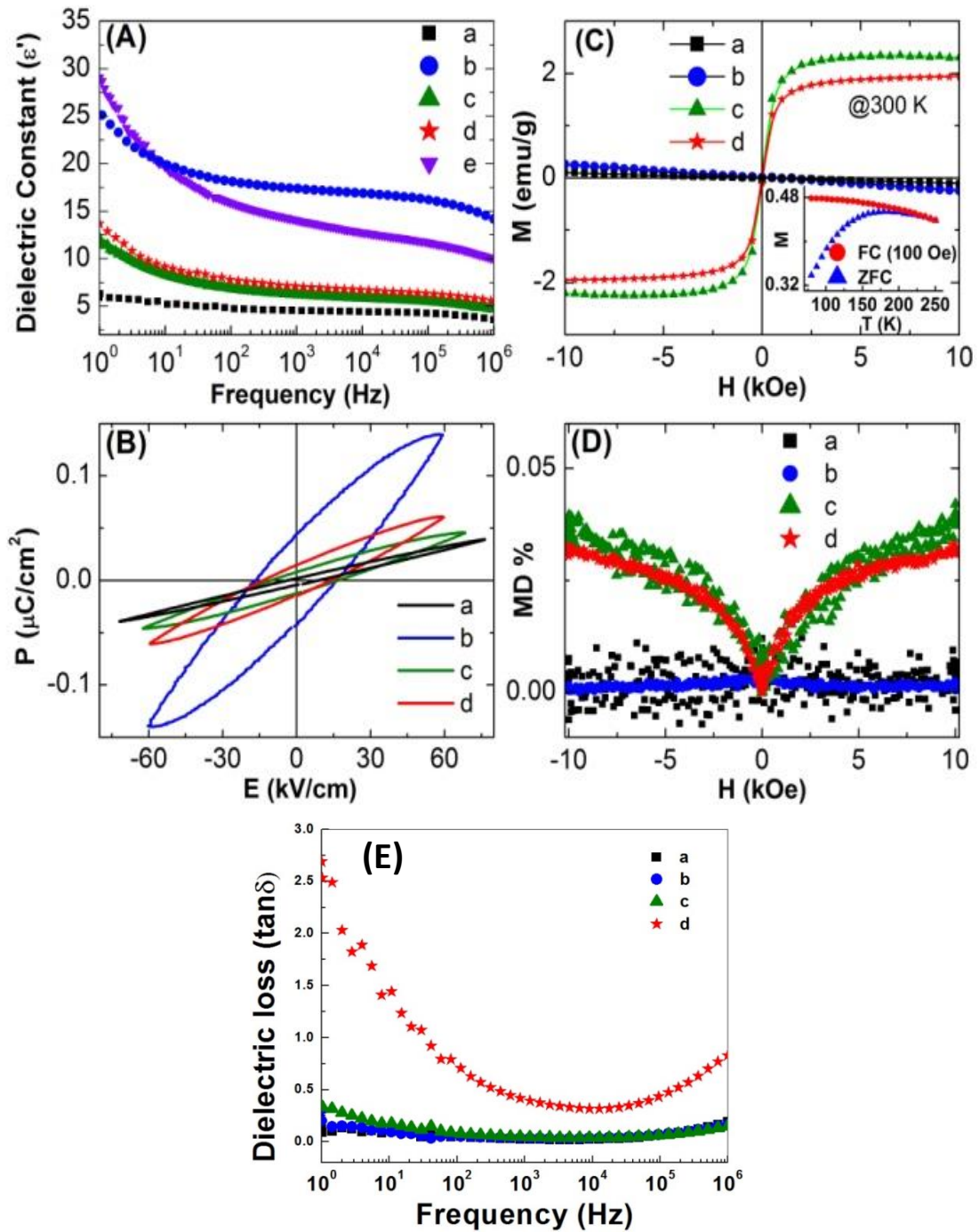


Figure 4.6: (A) Dielectric constant vs frequency plots, (B) P-E curves, (C) M vs H curves, (D) MD coupling and (E) Dielectric loss vs frequency of (a) PVDF, (b) PVDF-RGO, (c) PVDF-RGO-Fe<sub>3</sub>O<sub>4</sub>, (d) PVDF-RGO-Fe<sub>3</sub>O<sub>4</sub>-ZnO and (e) PVDF-ZnO. Inset in (C) shows FC and ZFC curves for PVDF-RGO-Fe<sub>3</sub>O<sub>4</sub>-ZnO.

Figure 4.6(B) shows room temperature ferroelectric (P-E) loops of the studied films. The highest polarization observed was for PVDF-RGO ( $0.13 \mu\text{C cm}^{-2}$ ) at poling field  $60 \text{ kV/cm}$ . The polarization seems to be affected by both the dielectric constant and the percentage of the piezoelectric  $\beta$ -phase in the film. Although the fraction of  $\beta$ -phase is similar ( $\sim 80\%$ ) in both PVDF and PVDF-RGO films, the increase in polarization in PVDF-RGO seems to be due to the accumulation of the charges at the interface of the conducting and dielectric phases, facilitating the heterogeneous polarization in the systems. However, both PVDF-RGO- $\text{Fe}_3\text{O}_4$  and PVDF-RGO- $\text{Fe}_3\text{O}_4$ -ZnO films show lower polarization because of significant reduction in  $\beta$ -phase ( $\sim 50\%$ ) as well as reduced dielectric constant.

The magnetic nature of the  $\text{Fe}_3\text{O}_4$ -loaded films is confirmed by the magnetization curves at room temperature shown in figure 4.6(C). Furthermore, ZFC-FC curves in the inset confirm the superparamagnetic nature of the used  $\text{Fe}_3\text{O}_4$  nanoparticles. The magneto-dielectric behavior of the films is measured at room temperature (Figure 4.6(D)). The magneto-dielectric coupling MD(%) is defined as  $\frac{\varepsilon_H - \varepsilon_0}{\varepsilon_0} \times 100(\%)$ , where  $\varepsilon_H$  and  $\varepsilon_0$  are the dielectric constants with and without magnetic field,  $H$ . Clearly, only the  $\text{Fe}_3\text{O}_4$ -loaded films show dielectric constant dependence on magnetic field. The curves can be fitted using a parabolic equation:  $\text{MD} = \gamma H^2$ , which originates from the lowest-order coupling terms in the free energy expansion as discussed before in section 3.2.4 (refer to equation 3.4). As mentioned before, symmetry considerations allow the scalar term  $P^2 M^2$  in Ginzburg-Landau free energy expansion [151], where  $P$  and  $M$  are the electric polarization and magnetization of the system. A similar quadratic dependence of MD coupling on magnetic field has been observed in other multiferroics [84, 152].

The origin of magneto-dielectric coupling in these samples could be attributed to the effect of magnetostriction in magnetic  $\text{Fe}_3\text{O}_4$  causing piezoelectricity in ferroelectric PVDF.

Upon application of magnetic field, the magnetic domains of  $\text{Fe}_3\text{O}_4$  align in such a way which can cause stress on neighboring PVDF phase via magnetostriction, which eventually leads to accumulation of some surface charge due to the piezoelectric effect. The elastic interaction between the magnetic ( $\text{Fe}_3\text{O}_4$ ) and ferroelectric (PVDF) phases strongly depends on the microstructure and coupling interaction between the magnetic and ferroelectric interfaces.

#### **4.2.2 PVDF FILMS LOADED WITH $\text{Fe}_3\text{O}_4$ AND GRAPHENE OXIDE (GO) [153]**

Here, we report the effect of loading PVDF matrix with graphene oxide (GO) and  $\text{Fe}_3\text{O}_4$  nanoparticles on the dielectric and MD coupling of PVDF self-standing thin film composites. The films were prepared using a solvent casting routine similar to the one reported in the previous section. GO was used because of its high surface area, mechanical strength and thermal conductivity [154]. In addition, it has been reported in a previous study [155] that the dielectric constant of the PVDF composites can be increased by loading it with GO by the solvent casting method.

Structural characterization carried out using XRD and FTIR spectroscopy revealed a decrease in  $\alpha$ -phase characteristic peaks and modes, on the expense of the piezoelectric  $\beta$ -phase in the GO-loaded films (figure 4.7). This is attributed to strong interaction between carbonyl groups in graphene oxide and fluorine ions in PVDF, causing a transformation of the  $\alpha$ -phase's  $\text{TG}^+\text{TG}^-$  conformation into the TTTT conformation characteristic of the  $\beta$ -phase [132].

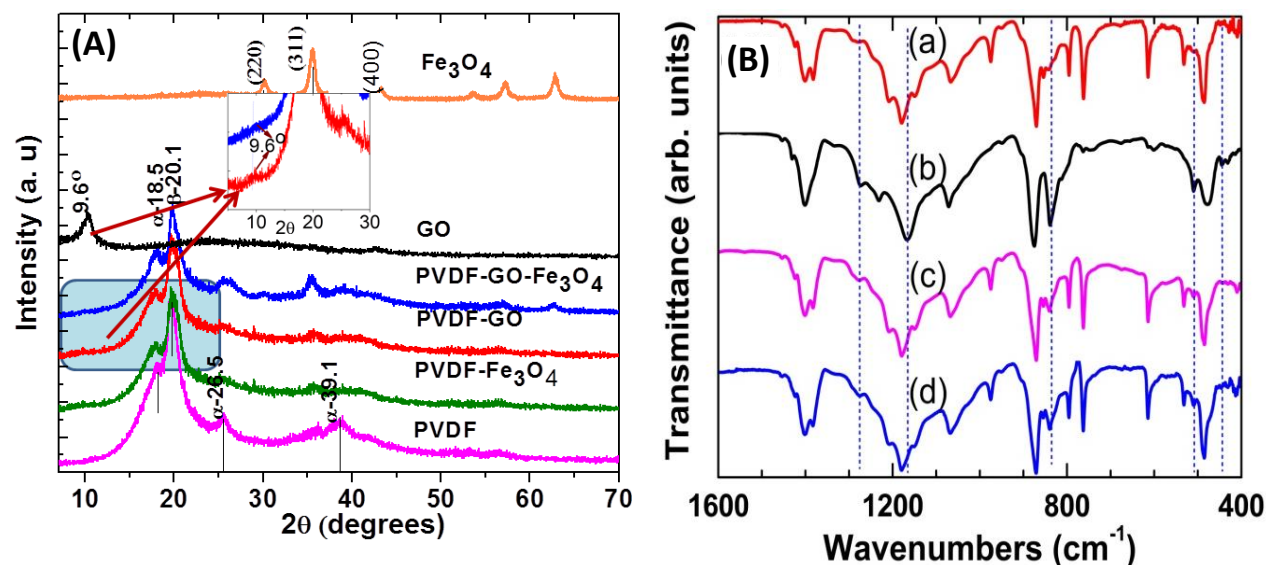


Figure 4.7: (A) XRD spectra of PVDF composite films. The inset highlights the GO characteristic peak at  $2\theta = 9.6^\circ$ . (B) FTIR spectra for PVDF (a), PVDF-GO (b), PVDF-Fe<sub>3</sub>O<sub>4</sub> (c) and PVDF-GO-Fe<sub>3</sub>O<sub>4</sub> (d).

The room temperature ferroelectric loops of the composite films are shown in figure 4.8. It should be noted that samples with no GO content exhibit banana-shaped ferroelectric loops, which is indicative of lossy behavior [156]. However, the other composite films show higher polarization values compared to the pristine PVDF film. This is due to the accumulation of charges at the interfaces of the conducting Fe<sub>3</sub>O<sub>4</sub> and the dielectric GO, which enhances the formation of electric dipoles. The increase in ferroelectric polarization values in films loaded with GO can also be attributed to the increase in the  $\beta$ -phase content of those films.

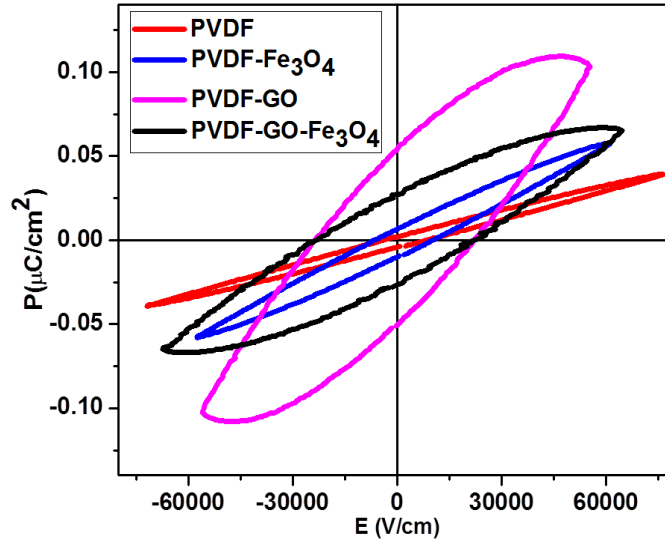


Figure 4.8: Room temperature  $P$ - $E$  loops at 100 Hz of undoped PVDF and composite films.

The dielectric constant of the studied films is measured at room temperature as a function of frequency (figure 4.9(a)). It was found that the dielectric constant generally drops at higher frequencies, which is due to molecular dipoles being unable to follow the driving signal oscillations. The addition of  $\text{Fe}_3\text{O}_4$  and GO particles to the polymer matrix leads to increasing permittivity due MWS polarization brought up earlier; where the charge carriers accumulate at the polymer-nanofillers interface.

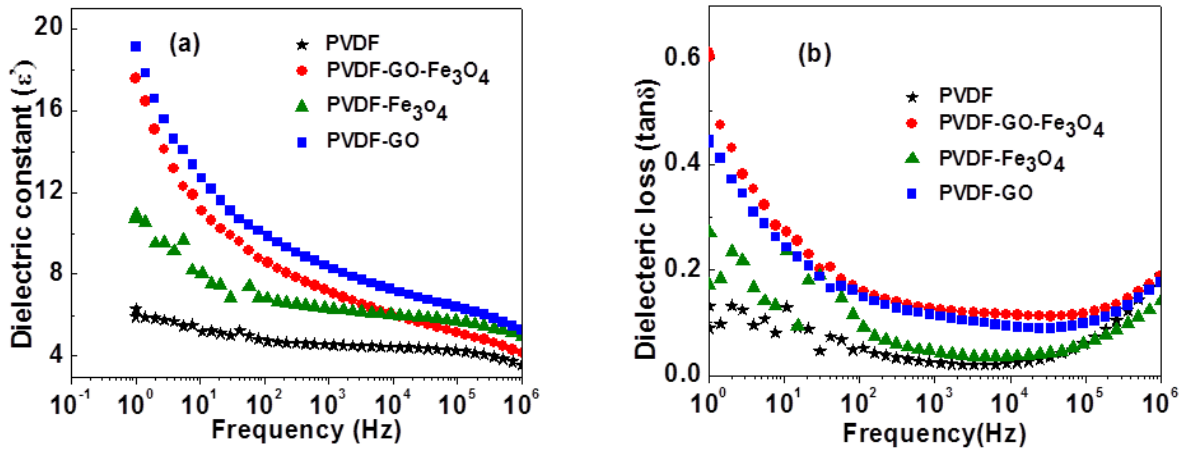


Figure 4.9: (a) Dielectric constant and (b) dielectric loss dependence on frequency at room temperature.

The dielectric loss (figure 4.9(b)) shows a similar decreasing trend as a function of frequency. The factors contributing to dielectric loss in composite films were brought up in section 4.2.1 (refer to equation 4.2).

The room temperature MD coupling curves for PVDF composite films are compiled in figure 4.10(a). In resemblance to the previous set of PVDF-RGO composites reported in section 4.2.1, the samples loaded with magnetite show variation in dielectric constant upon applying magnetic field. The obtained curves have a quadratic dependence on magnetic field ' $H$ ' as allowed by symmetry (refer to section 4.2.1). The observed MD coupling is extrinsic in part, resulting of magnetostriction of  $\text{Fe}_3\text{O}_4$  particles and the piezoelectricity of PVDF  $\beta$ -phase. Figure 4.10(b) depicts the MD coupling behavior of the PVDF-GO- $\text{Fe}_3\text{O}_4$  film at different temperatures. Considering the temperatures examined, we note that the MD coupling peaks at 100 K and it becomes lower at higher temperatures. This can be explained with the help of the film's ZFC-FC curves shown in figure 4.11, where the blocking temperature is found to between 50 K and 100 K. As mentioned in chapter 1, the magnetite nanoparticles –being responsible for the blocking behavior– will have just the enough thermal energy to flip in response to an external magnetic field at the blocking temperature. This will result to maximum magnetization value and the strongest magnetostriction effect, which implies highest MD coupling.

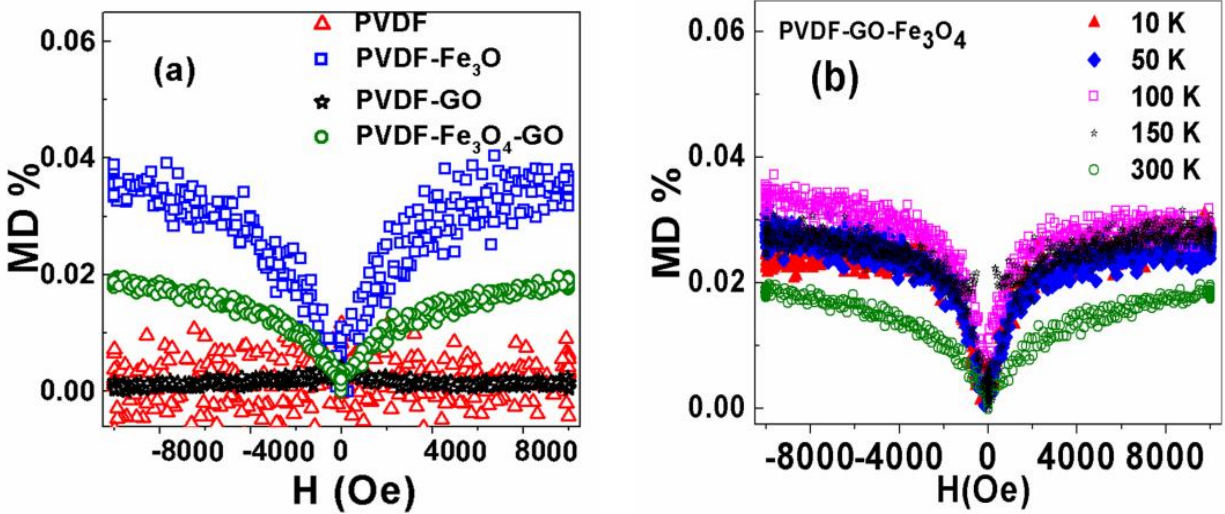


Figure 4.10: (a) MD coupling for composite films at room temperature and (b) MD coupling for the PVDF-GO-Fe<sub>3</sub>O<sub>4</sub> film at different temperatures.

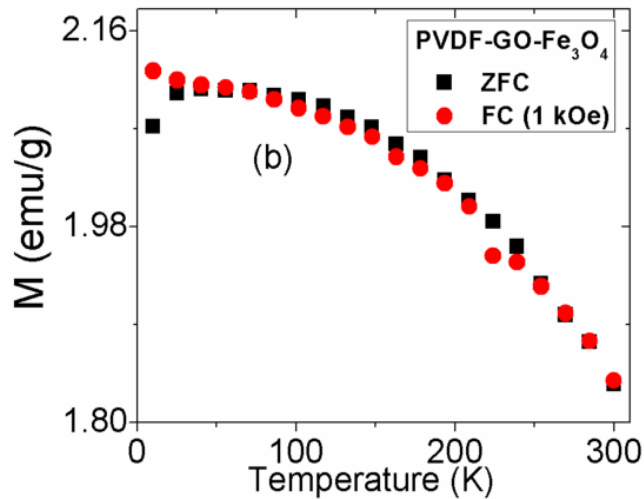


Figure 4.11: ZFC-FC curves for the PVDF-GO-Fe<sub>3</sub>O<sub>4</sub> film.

#### 4.2.3 PVDF-Ni NANOHYBRIDS [149]

In this work, MD coupling between magnetic nickel nanoparticles and piezoelectric PVDF films was studied. Before being dispersed in the PVDF matrix, Ni nanoparticles were subject to surface functionalization using hydrogen peroxide (H<sub>2</sub>O<sub>2</sub>) with the aim of attaching



hydroxyl functional groups (OH) to the particles' surface. The goal was to enhance the strain transfer efficiency among the magnetic and piezoelectric phases.

The composite films were prepared by solvent casting route, and characterized with XRD and FTIR techniques. In particular, absorption bands characteristic to Ni—OH bonds were detected in FTIR spectra. Also, PVDF crystallographic composition of the Ni-doped films showed an enhancement in the  $\beta$ -phase to  $\alpha$ -phase ratio.

PVDF films loaded with a 10% weight ratio of surface modified Ni nanoparticles showed higher polarization values in measured  $P$ - $E$  loops compared to films hosting non-functionalized Ni. The PVDF-modified Ni composite films also had higher the breakdown voltage, as well as lower leakage current. It is noted that the amount of Ni used was below the percolation threshold reported for PVDF-Ni system. Therefore, the leakage current has low effect on polarization. The improvement in ferroelectric polarization in hybrid films utilizing functionalized Ni is attributed to improved interface between the two phases due to the strong dipolar interaction between the OH groups and fluorine ions on the PVDF chain. Such interaction improves the dispersion of Ni nanoparticles in the PVDF matrix.

The MD coupling for the PVDF-Ni (modified) and PVDF-Ni (non-modified) films are compared in figure 4.12. The obtained data for both samples show parabolic behavior proportional to the square of applied field ( $\sim\gamma H^2$ ). Again, the MD coupling behavior is attributed to the strain induced on piezoelectric PVDF due to magnetostriction manifested by magnetic Ni nanoparticles. The effect is stronger for functionalized Ni because of hydroxyl groups inducing better coupling.

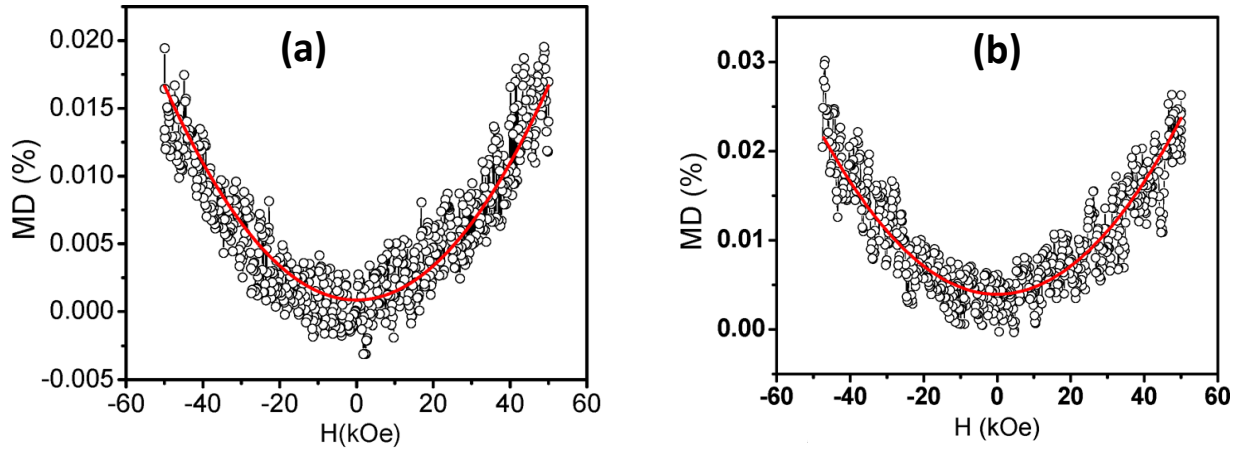


Figure 4.12: MD coupling of the (a) PVDF-Ni and (b) PVDF-functionalized Ni films.

#### 4.2.4 MAGNETO-DIELECTRIC PROPERTIES IN PVDF-BARIUM HEXAFERRITE ( $\text{BaFe}_{12}\text{O}_{19}$ ) COMPOSITE FILM [157]

In this work, barium hexaferrite (BHF) was used as a filler due to its high magnetocrystalline anisotropy. BHF nanoparticles synthesized via sol-gel route were used to make PVDF-( $x$  volume %) of BHF –with  $x$  ranging between 2.5 and 15– by solvent casting method. In addition, pure PVDF film and BHF pellet were made and measured for comparison.

Structural characterization was carried out by XRD and FTIR, where it was found that all the films –including the undoped PVDF– consist of a mixture of  $\alpha$  and  $\beta$  polymorphs. The ratio of  $\beta$  to  $\alpha$  was estimated from FTIR spectra where it was found to increase in the BHF loaded films up to  $x = 5\%$ .

An increase in the electric conductivity with frequency has been observed in all samples. It was noticed also that the conductivity increases with increasing BHF amount in an agreement with the standard conductor-insulator percolative systems. Additionally, the dielectric constant and loss decrease with increasing frequency, and films with higher BHF content show a higher dielectric constant at fixed frequency. The enhanced dielectric constant is mainly attributed to

interfacial polarization, with a minimal contribution to the increased  $\beta$ -phase. The ferroelectric moment and leakage current also showed an enhancement with BHF content up to  $x = 15\%$ .

The quality of MD coupling data for heavily BHF loaded PVDF films is found to be poor because of high dielectric loss (figure 4.13). On the other hand, samples with low BHF content show linear MD behavior, suggesting the possibility of spin-charge coupling.

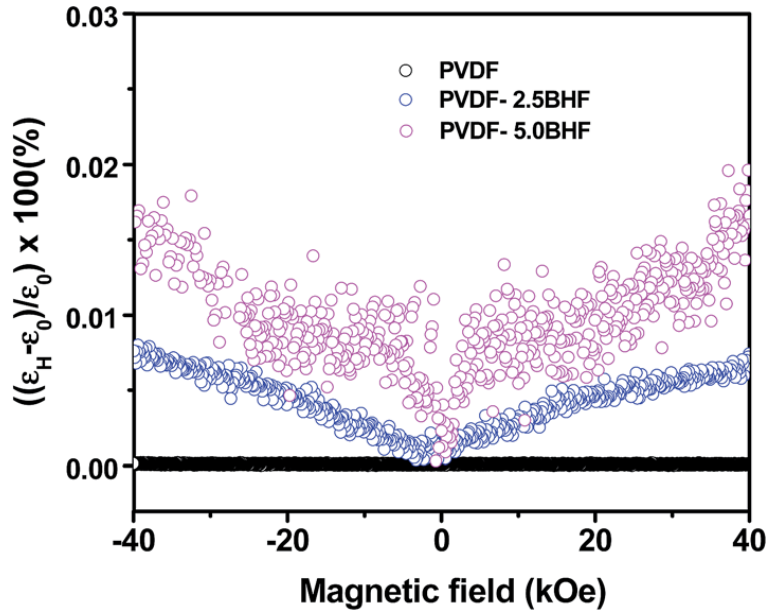


Figure 4.13: MD coupling of undoped and lower BHF percentage PVDF films.

### 4.3 CONCLUSIONS

Improving extrinsic magneto-electric coupling in hybrid systems is becoming the focus of many researchers owing to the promising room temperature uses. An attractive system in this research area is polyvinylidene difluoride (PVDF) based film composites, on account of the ease to prepare the thermodynamically stable at room temperature piezoelectric  $\beta$ -phase of PVDF. In this chapter, four systems of solvent-cast PVDF composite films were presented.

The work on PVDF-Fe<sub>3</sub>O<sub>4</sub> hybrid films loaded with reduced graphene oxide (RGO) powder and zinc oxide (ZnO) nanorods showed a reduction in the  $\beta$ -phase composition in the

PVDF matrix upon loading with  $\text{Fe}_3\text{O}_4$  and ZnO nanofillers. The relative  $\alpha$  and  $\beta$  composition was estimated from FTIR and Raman spectra using Lambert-Beer's law. All nanofillers-loaded PVDF films show an increase in the dielectric constant but the electric polarization depends on the percentage of polar ferroelectric  $\beta$ -phase in the films.  $\text{Fe}_3\text{O}_4$ -loaded hybrid PVDF films exhibit multiferroic behavior with a magneto-dielectric (MD) coupling constant of  $\sim 0.04\%$ . The low MD feature was attributed in part to agglomeration of  $\text{Fe}_3\text{O}_4$  particles in the PVDF polymer matrix, suggesting that improving the efficiency of nanofillers dispersion in PVDF film composites is a step towards making them suitable for room temperature MD device applications.

On the other hand, using graphene oxide (GO) as a nanofiller in PVDF matrix was shown to increase the  $\beta$ -phase content, which was attributed to better dispersity owing to the functional groups attached to the nanofiller's lattice. Nevertheless, the PVDF-GO based composite films also showed an increase in dielectric constant and polarization moment compared to pristine PVDF. MD coupling measurements on ternary PVDF-GO- $\text{Fe}_3\text{O}_4$  films showed a maximum coupling value around the  $\text{Fe}_3\text{O}_4$  nanoparticles' blocking temperature, in accordance with the thermally induced spin flip mechanism as expected from ZFC-FC data.

The effect of using nickel (Ni) and barium hexaferrite (BHF) as PVDF nanofillers was also reported. In both cases, the amount of polar  $\beta$ -phase of PVDF was found to increase in PVDF composites compared to pristine films. It was also found that modifying the Ni nanoparticles to carry  $-\text{OH}$  functional groups prior to dispersion in PVDF improved the ferroelectric polarization and reduced the leakage current. MD measurements show that surface functionalized nickel-PVDF composites exhibit a higher coupling factor than that of the unmodified one, which was again attributed to the functional groups improving the film homogeneity and resulting in better strain-transfer efficiency. In case of using BHF, the

dielectric permittivity of the system increases nearly eight fold upon addition of 12.5% BHF by volume without much compromising the dielectric loss. Moreover, small magnetolectric coupling in this system is detected, suggesting the possible tunability of the dielectric permittivity with external magnetic field.

In conclusion, it seems that improving the dispersity of nanofillers in PVDF film is a critical factor in enhancing the dielectric and ferroelectric properties. One seemingly successful way to achieve better dispersity is via surface functionalization, suggesting such direction for future research activities. Also, the dependence of MD coupling coefficient is plotted as a function of magnetostriction coefficients and magnetic saturation (listed in table 4.2) in figure 4.14 (a,b). It seems from the plot that nanofillers with a higher magnetostriction coefficient ( $\text{Fe}_3\text{O}_4$  in this case) would induce higher MD coupling in loaded PVDF films.

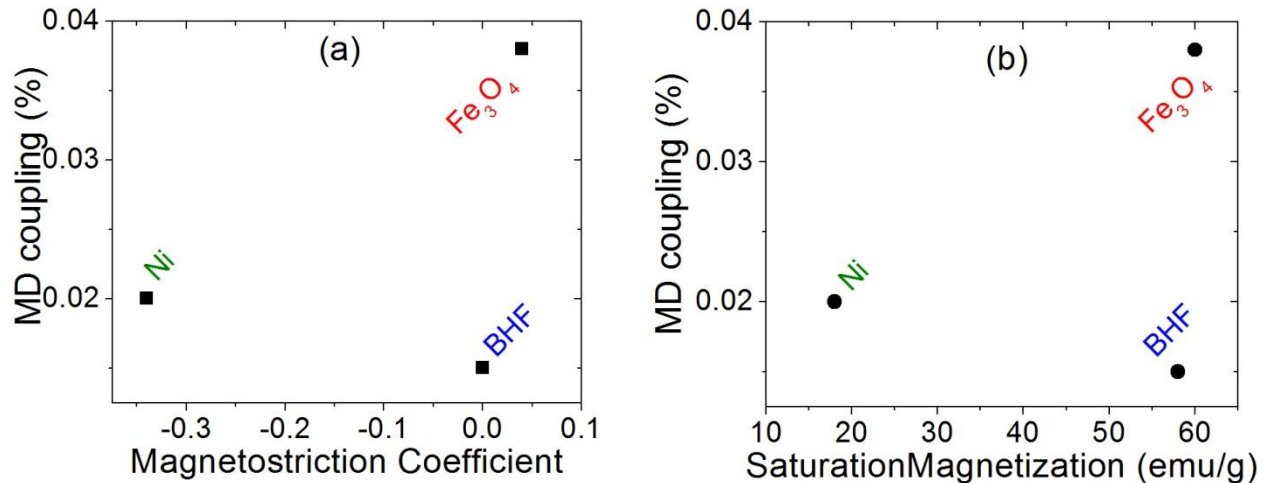


Figure 4.14: MD coupling in nanofillers loaded PVDF films as a function of magnetostriction and saturation magnetization of the magnetic nanofillers.

Magnetic Nanofiller	Magnetostriction Coefficient [Ref]	Saturation Magnetization emu/g [Ref]
BHF	$-1.5 \times 10^{-5}$ [158]	58 [157]
Ni	-0.34 [159]	18 [149]
Fe <sub>3</sub> O <sub>4</sub>	0.04 [116]	60 [160]

Table 4.2: Magnetostriction and saturation magnetization values of the magnetic nanofillers reported in this chapter, along with the reference in which each values is reported.

## CHAPTER 5: SUMMARY AND FUTURE WORK

The topics of multiferroicity and magnetoelectricity were the focus of this thesis. Two intrinsic multiferroic systems: Iron (III) vanadate ( $\text{FeVO}_4$ ) as an example of type II multiferroics, and magnetite ( $\text{Fe}_3\text{O}_4$ ) as a ferromagnetic material where charge ordered ferroelectricity is observed. Also, polyvinylidene difluoride (PVDF)-based film composites were studied as extrinsic, strain-induced magnetoelectric systems, where PVDF served as the ferroelectric phase while the magnetic constituent was  $\text{Fe}_3\text{O}_4$ , nickel or barium hexaferrite nanoparticles.

In chapter 2, we investigated the magnetic and ferroelectric anisotropy in undoped single crystals of triclinic  $\text{FeVO}_4$  synthesized by flux-growth method. It was revealed that the crystallographic  $a$ -axis as a magnetically easy axis and favorable for magnetic moments alignment. Our ferroelectric measurements also showed the polarization moment density of  $\text{FeVO}_4$  be higher in the direction of  $a$ , denoting this direction to be favorable from electric polarization viewpoint also. This is supported by noting that the relative change in dielectric constant versus temperature is larger along the  $a$ -axis.

The relative change in dielectric constant as a function of magnetic field was also presented. The data manifested a strong dependence of the dielectric behavior on magnetic field, in a similar manner to what was observed before in  $\text{Ni}_3\text{V}_2\text{O}_8$  system, suggesting field-induced spin reorientations. Unlike  $\text{Ni}_3\text{V}_2\text{O}_8$ , the isothermal  $M$  vs  $H$  data showed a paramagnetic linear response, unresponsive to the assumption of spin reorientations.

$\text{FeVO}_4$  single crystals doped with zinc and manganese were also prepared. The choice of Zn aimed to reduce exchange striction between the  $\text{Fe}^{3+}$  and  $\text{Zn}^{2+}$ , and to investigate the role of magnetically induced lattice distortions in creating the spontaneous ferroelectric moment. On the

other hand, Mn-doped crystals were also prepared to test for the role played by Dzyaloshinskii-Moriya interaction in  $\text{FeVO}_4$  ferroelectricity.

The magnetic susceptibility dependence on temperature for the doped crystals was found to be qualitatively similar to the undoped  $\text{FeVO}_4$ . However, unexpectedly, the effective moment per magnetic ion increased for some zinc contents, which was assigned to  $\text{Zn}^{2+}$  induced asymmetries. The doped crystals were shown to retain the ferroelectric nature as well.

A better route for doping  $\text{FeVO}_4$  single crystals shall be considered in the future work, to gain better control on the dopant percentages. Doping on the vanadium site may be investigated as well.

The dielectric and ferroelectric properties of gadolinium-doped  $\text{Fe}_3\text{O}_4$  nanoparticles were investigated in chapter 3 for better understanding of charge-ordered ferroelectricity in this system, besides the potential biomedical applications. Samples with higher Gd content were found to have higher activation energy for Debye relaxation process. Also, pellets made of Gd-doped nanopowder showed higher ferroelectric polarization moment which we attribute to the larger ionic size of  $\text{Gd}^{3+}$  leading to enhanced lattice distortions. Heat capacity data of undoped  $\text{Fe}_3\text{O}_4$  carried some contribution around 40 K of phonon modes which are possibly associated with the ferroelectric order.

For better understanding of ferroelectricity in  $\text{Fe}_3\text{O}_4$ , finer control on the sample's stoichiometry should be achieved to rule out possible perturbations in oxygen content.

Strain induced magnetoelectric coupling in (PVDF)-based film composites was the focus of the last chapter. The effect of various nanofillers on PVDF piezoelectricity and on the resulting magnetoelectric coupling was investigated. For instance, the use of reduced graphene oxide and zinc oxide as nanofillers in PVDF- $\text{Fe}_3\text{O}_4$  hybrid films was found to reduce the  $\beta$ -phase



content, which is ferroelectric and piezoelectrically active phase of PVDF. The films still exhibited weak magneto-dielectric behavior, owing in part to agglomeration of  $\text{Fe}_3\text{O}_4$  particles in the PVDF polymer matrix. Using graphene oxide, on the other hand, as a nanofiller was shown to increase the  $\beta$ -phase content, which we attribute to better dispersity as a result of the functional groups attached to the graphene oxide lattice.

The effect of using nickel (Ni) and barium hexaferrite (BHF) as PVDF nanofillers was also reported. It was found PVDF films which carry surface-functionalized Ni nanoparticles show enhanced ferroelectric polarization and higher magneto-dielectric coupling as compared to films with non-functionalized Ni. On the other hand, an enhancement in the dielectric permittivity and magneto-dielectric behavior was seen in BHF-loaded films.

Dielectric studies of PVDF hybrid films suggested that improving the dispersity of nanofillers in PVDF film is a critical factor in enhancing the dielectric and ferroelectric properties. One seemingly successful way to achieve better dispersity is via surface functionalization, suggesting such direction for future research activities.

## APPENDIX: SINGLE CRYSTALS SYNTHESIS USING FLUX GROWTH METHOD

From scientific and technological points of view, single crystals are preferred over powder or ceramic samples for the following reasons [161]:

- Powder samples have a higher surface to volume ratio, which affects and interferes with manifestation of intrinsic properties.
- Inter-granular composition and porosity effects.
- Anisotropy measurements are not possible on powder samples.
- Single crystals generally have a higher purity; many macroscopic and microscopic probes can only be effectively utilized in the form of single crystals.

Several methods are available for crystal growth from melts. Examples are:

- ❖ Zone melting: in which a small melting zone is moved along the crystal.
- ❖ Crystal pulling: where a seed crystal is pulled very slowly out of a molten flux of the same material.
- ❖ Bridgmann cooling: Here, a seed crystal is placed at the side of the container with the molten flux. The container is cooled slowly from the side.

All of the above techniques are suitable for materials which melt consistently or uniformly, and have other limitations. Such limitations can be handled via growth from ‘molten metal flux’ technique, which is known for short as ‘*flux growth*’. In this method, powder precursors are mixed and kept in a non-reactive container, brought to melting and cooled down at a slow rate. The precursors are chosen so that they melt congruently, and sometimes mixed in non-stoichiometric ratios to account for one precursor volatility or to use one as a solvent for the other(s).

Advantages of this technique include growing crystals below their melting point, which results in fewer defects and less thermal strain. Also, it is a relatively cheap technique, and it offers a clean environment for crystal growth.

One of the technique's disadvantages is the possibility of the flux entering the growing crystal as impurity, or the crystal growing around pockets of flux. This can be handled by adjusting the growth rate.

It is important to understand the binary phase diagram of the materials involved before growing the crystal. For example, to grow silicon crystals, choosing zinc as a solvent is not a good idea; since the Si-Zn solution becomes homogenous (technical term: *eutectic*) only at 99.955% Zn content [162]. Also, Zn has a high vapor pressure hence is volatile.

Among the parameters which need to be decided is the soak period. The kinetics of many solutions is slow, and the soak time needed to blend the solute and the solvent needs experimentation. Another parameter is the cooling time; in general, the slower the cooling rate the better (i.e.: higher quality) is the crystal growth and the fewer flux inclusions. For furnaces with no temperature controllers, a good trick to slow down the cooling rate is to increase the thermal mass. For example, the crucible could be packed in sand ( $\text{SiO}_2$ ) for a slower natural cooling rate.

To separate the product crystals from the flux, chemical leaching may be used. Heating on a hot plate can speed the process of washing away the solvent. The formed crystals should be visible on the surface of the flux before leaching. It worth noting that, whenever leaching is not possible for chemical considerations, centrifugation of molten flux may be applied.

The reactivity of the involved materials has to be taken in account. Some materials may be reactive with the crucible, which will result in discoloration or deformation of the crucible.

Such problem becomes more profound at higher temperatures. Also, it is important to consider the thermal shock resistance of the crucible material while making the crucible choice.

When the phase diagram involves more than one solid phase, the product of flux growth process will depend on the compositions involved. It is usually the case that getting a specific phase would be bounded by certain compositions.

Generally, it is helpful to start with diagnostic trials in case of new systems. Such diagnosis involved growing several batches at fairly fast rates. The grown crystals will be small in this case, which is why it becomes hard to separate them. In this case, sewing through the flux and looking at the cross section under a microscope would be a useful trick.

A suitable container for the process should be chosen. Some fluxes work better with certain materials. Likewise, some crucibles are better with certain fluxes and metals. It can be the case where the reactants attack the crucible. In some cases, welding the crucible shut is necessary to maintain the correct stoichiometry.

Flux incorporation in the final product is a common problem, sometimes identifiable by visual inspection. It can be avoided or minimized by including nucleation sites (i.e.: smaller-sized crystals). Another possible problem is getting one of the elements in the forming crystals partially substituted by the flux. This can happen if the flux element is similar to one of the solutes chemically or in atomic size.

The formed crystals can be separated from flux either chemically or mechanically. A suitable chemical reagent should be used to dissolve the flux while not affecting the formed crystals. In some cases, the crystals start reacting with the reagent once they are separated from the flux. Therefore, removal from reagent is preferred as soon as separation occurs. In other

instances, chemical separation of crystals can take as long as one month, to avoid damaging the crystals.

One specifically useful technique is dissolving the flux metal in another metal. This would be possible once a suitable solvent is available. For example, indium flux can dissolve in mercury.

In such cases where chemical separation is not possible, one is left only with cutting the crystals from the melt, or any other appropriate mechanical route.

A problem that is usually encountered upon attempting to grow crystals from flux is the slow solution kinetics. In other words may have slow solubility in a specific solvent, much slower than the other components, that it gets substituted by other elements. Such problem can be addressed by pre-reacting the desired compound and using it in the growth charge (i.e.: the flux), rather than using the forming elements. Also, longer soaking time at the maximum temperature is required to increase the solubility.

Because of the popularity and ease of the flux growth technique, some modifications are sometimes incorporated to meet specific needs or address encountered issues. Among these modifications:

- Using temperature gradient: In this technique, one compound has a very low solubility in the used solvent. An arc-melted pellet would be placed in the flux which is then brought up to the maximum temperature. Then, a temperature gradient would be kept between the top and bottom parts of the crucible. After several days, crystals will start forming at the cooler end of the crucible.

- Evaporation growth: Done by super-saturating the inside environment of the crucible with vapors of the flux material, which has to be the most volatile constituent in the mixture. One disadvantage is the formation of too many small crystals on the surface.
- Traveling solvent method: This method, discussed by Wolff and Mlavsky [163], is specifically useful when larger sized crystals are desired.

**BIBLIOGRAPHY**

- [1] W. Kohn, *Reviews of Modern Physics* **71** (2), S59-S77 (1999).
- [2] B. D. Cullity and C. D. Graham, *Introduction to magnetic materials*. (John Wiley & Sons, 2011).
- [3] S. Blundell, *Magnetism in Condensed Matter (Oxford Master Series in Physics)*. (Oxford University Press, USA, 2001).
- [4] N. A. Frey, S. Peng, K. Cheng and S. Sun, *Chemical Society Reviews* **38** (9), 2532-2542 (2009).
- [5] S. Horikoshi and N. Serpone, in *Microwaves in Nanoparticle Synthesis* (Wiley-VCH Verlag GmbH & Co. KGaA, 2013), pp. 1-24.
- [6] D. L. Leslie-Pelecky and R. D. Rieke, *Chemistry of Materials* **8** (8), 1770-1783 (1996).
- [7] G. C. Papaefthymiou, *Nano Today* **4** (5), 438-447 (2009).
- [8] Q. A. Pankhurst, J. Connolly, S. K. Jones and J. Dobson, *Journal of Physics D: Applied Physics* **36** (13), R167 (2003).
- [9] C. P. Bean and J. D. Livingston, *Journal of Applied Physics* **30** (4), S120-S129 (1959).
- [10] I. Rhee, *Journal of the Korean Physical Society* **54** (4), 1721-1724 (2009).
- [11] H. Nemala, J. S. Thakur, V. M. Naik, P. P. Vaishnava, G. Lawes and R. Naik, *Journal of Applied Physics* **116** (3), 034309 (2014).
- [12] I. Rabias, D. Tsi trouli, E. Karakosta, T. Kehagias, G. Diamantopoulos, M. Fardis, D. Stamopoulos, T. G. Maris, P. Falaras, N. Zouridakis, N. Diamantis, G. Panayotou, D. A. Verganelakis, G. I. Drossopoulou, E. C. Tsilibari and G. Papavassiliou, *Biomicrofluidics* **4** (2), 024111 (2010).

- [13] F. M. Koehler, M. Rossier, M. Waelle, E. K. Athanassiou, L. K. Limbach, R. N. Grass, D. Gunther and W. J. Stark, *Chemical Communications* (32), 4862-4864 (2009).
- [14] A. Schätz, O. Reiser and W. J. Stark, *Chemistry – A European Journal* **16** (30), 8950-8967 (2010).
- [15] N. A. Frey and S. Sun, *Inorganic Nanoparticles: Synthesis, Applications, and Perspectives*, CRC Press, Boca Raton, USA, 33-67 (2010).
- [16] G. Lawes, A. B. Harris, T. Kimura, N. Rogado, R. J. Cava, A. Aharony, O. Entin-Wohlman, T. Yildirim, M. Kenzelmann, C. Broholm and A. P. Ramirez, *Physical Review Letters* **95** (8), 087205 (2005).
- [17] H. Katsura, N. Nagaosa and A. V. Balatsky, *Physical Review Letters* **95** (5), 057205 (2005).
- [18] R. Moessner and A. P. Ramirez, *Phys. Today* **59** (2), 24 (2006).
- [19] A. Ramirez, *Annual Review of Materials Science* **24** (1), 453-480 (1994).
- [20] D. Khomskii, *Physics* **2**, 20 (2009).
- [21] A. B. Harris, *Physical Review B* **84** (6), 064116 (2011).
- [22] R. Mangalam, N. Ray, U. V. Waghmare, A. Sundaresan and C. Rao, *Solid State Communications* **149** (1), 1-5 (2009).
- [23] S. Hans, *Journal of Physics: Condensed Matter* **20** (43), 434201 (2008).
- [24] H.-R. Wenk and A. Bulakh, *Minerals: their constitution and origin*. (Cambridge University Press, 2004).
- [25] C. Kittel, *Introduction to solid state physics*. (Wiley, 2005).
- [26] V. Wadhawan, *Introduction to ferroic materials*. (CRC Press, 2000).



- [27] D.-C. Jia, J.-H. Xu, H. Ke, W. Wang and Y. Zhou, *Journal of the European Ceramic Society* **29** (14), 3099-3103 (2009).
- [28] J. Wang, J. B. Neaton, H. Zheng, V. Nagarajan, S. B. Ogale, B. Liu, D. Viehland, V. Vaithyanathan, D. G. Schlom, U. V. Waghmare, N. A. Spaldin, K. M. Rabe, M. Wuttig and R. Ramesh, *Science* **299** (5613), 1719-1722 (2003).
- [29] E. K. Salje, *Annual Review of Materials Research* **42**, 265-283 (2012).
- [30] B. B. Van Aken, J.-P. Rivera, H. Schmid and M. Fiebig, *Nature* **449** (7163), 702-705 (2007).
- [31] H. Schmid, *Ferroelectrics* **162** (1), 317-338 (1994).
- [32] N. A. Hill, *The Journal of Physical Chemistry B* **104** (29), 6694-6709 (2000).
- [33] O. Auciello, J. F. Scott, R. Ramesh, M. S. Division, U. o. N. S. Wales and U. o. Maryland, *Journal Name: Phys. Today; Journal Issue: Jul. 1998, Medium: X; Size: 22-27* (1998).
- [34] A. Iyama and T. Kimura, *Physical Review B* **87** (18), 180408 (2013).
- [35] L. W. Martin, *Dalton Transactions* **39** (45), 10813-10826 (2010).
- [36] M. Nic, L. Hovorka, J. Jirat, B. Kosata and J. Znamenacek, *IUPAC Compendium of Chemical Terminology-The Gold Book*. (International Union of Pure and Applied Chemistry, 2005).
- [37] R. Seshadri and N. A. Hill, *Chemistry of Materials* **13** (9), 2892-2899 (2001).
- [38] A. A. Belik, S. Iikubo, T. Yokosawa, K. Kodama, N. Igawa, S. Shamoto, M. Azuma, M. Takano, K. Kimoto, Y. Matsui and E. Takayama-Muromachi, *Journal of the American Chemical Society* **129** (4), 971-977 (2007).
- [39] C. E. Mohn and S. Stølen, *Physical Review B* **83** (1), 014103 (2011).

- [40] E. H. Smith, N. A. Benedek and C. J. Fennie, *Inorganic Chemistry* **54** (17), 8536-8543 (2015).
- [41] J. B. Neaton, C. Ederer, U. V. Waghmare, N. A. Spaldin and K. M. Rabe, *Physical Review B* **71** (1), 014113 (2005).
- [42] B. Jeroen van den and I. K. Daniel, *Journal of Physics: Condensed Matter* **20** (43), 434217 (2008).
- [43] M. S. Senn, J. P. Wright and J. P. Attfield, *Nature* **481** (7380), 173-176 (2012).
- [44] N. Ikeda, K. Kohn, N. Myouga, E. Takahashi, H. Kitôh and S. Takekawa, *Journal of the Physical Society of Japan* **69** (5), 1526-1532 (2000).
- [45] N. Hur, S. Park, P. A. Sharma, J. S. Ahn, S. Guha and S. W. Cheong, *Nature* **429** (6990), 392-395 (2004).
- [46] Y. J. Choi, H. T. Yi, S. Lee, Q. Huang, V. Kiryukhin and S. W. Cheong, *Physical Review Letters* **100** (4), 047601 (2008).
- [47] T. Choi, Y. Horibe, H. T. Yi, Y. J. Choi, W. Wu and S. W. Cheong, *Nat Mater* **9** (3), 253-258 (2010).
- [48] I. Dzyaloshinsky, *Journal of Physics and Chemistry of Solids* **4** (4), 241-255 (1958).
- [49] T. Moriya, *Physical Review* **120** (1), 91-98 (1960).
- [50] S.-W. Cheong and M. Mostovoy, *Nat Mater* **6** (1), 13-20 (2007).
- [51] J. Zhang, L. Ma, J. Dai, Y. P. Zhang, Z. He, B. Normand and W. Yu, *Physical Review B* **89** (17), 174412 (2014).
- [52] I. A. Sergienko and E. Dagotto, *Physical Review B* **73** (9), 094434 (2006).
- [53] T. Kimura, *Annual Review of Condensed Matter Physics* **3** (1), 93-110 (2012).
- [54] R. C. Pullar, *Progress in Materials Science* **57** (7), 1191-1334 (2012).

- [55] L. Wang, D. Wang, Q. Cao, Y. Zheng, H. Xuan, J. Gao and Y. Du, *Scientific reports* **2** (2012).
- [56] P. Shepherd, K. K. Mallick and R. J. Green, *Journal of Magnetism and Magnetic Materials* **311** (2), 683-692 (2007).
- [57] W. Eerenstein, N. D. Mathur and J. F. Scott, *Nature* **442** (7104), 759-765 (2006).
- [58] N. A. Spaldin and M. Fiebig, *Science* **309** (5733), 391-392 (2005).
- [59] F. Manfred, *Journal of Physics D: Applied Physics* **38** (8), R123 (2005).
- [60] W. F. Brown, R. M. Hornreich and S. Shtrikman, *Physical Review* **168** (2), 574-577 (1968).
- [61] A. M. J. G. Van Run, D. R. Terrell and J. H. Scholing, *Journal of Materials Science* **9** (10), 1710-1714 (1974).
- [62] M. Kumar and K. L. Yadav, *Journal of Physics and Chemistry of Solids* **68** (9), 1791-1795 (2007).
- [63] V. M. Petrov, G. Srinivasan, M. I. Bichurin and A. Gupta, *Physical Review B* **75** (22), 224407 (2007).
- [64] K. Raidongia, A. Nag, A. Sundaresan and C. N. R. Rao, *Applied Physics Letters* **97** (6), 062904 (2010).
- [65] J. Zhai, Z. Xing, S. Dong, J. Li and D. Viehland, *Journal of the American Ceramic Society* **91** (2), 351-358 (2008).
- [66] G. Srinivasan, E. T. Rasmussen, J. Gallegos, R. Srinivasan, Y. I. Bokhan and V. M. Laletin, *Physical Review B* **64** (21), 214408 (2001).
- [67] S. Priya, R. Islam, S. Dong and D. Viehland, *Journal of Electroceramics* **19** (1), 149-166 (2007).

- [68] Z. He, J.-I. Yamaura and Y. Ueda, *Journal of Solid State Chemistry* **181** (9), 2346-2349 (2008).
- [69] R. D. Johnson and P. G. Radaelli, *Annual Review of Materials Research* **44** (1), 269-298 (2014).
- [70] L. M. Levinson and B. M. Wanklyn, *Journal of Solid State Chemistry* **3** (1), 131-133 (1971).
- [71] B. Robertson and E. Kostiner, *Journal of Solid State Chemistry* **4** (1), 29-37 (1972).
- [72] A. Daoud-Aladine, B. Kundys, C. Martin, P. G. Radaelli, P. J. Brown, C. Simon and L. C. Chapon, *Physical Review B* **80** (22), 220402 (2009).
- [73] A. P. Ramirez, *Annual Review of Materials Science* **24** (1), 453-480 (1994).
- [74] P. Mendels, A. Olariu, F. Bert, D. Bono, L. Limot, G. Collin, B. Ueland, P. Schiffer, R. J. Cava, N. Blanchard, F. Duc and J. C. Trombe, *Journal of Physics: Condensed Matter* **19** (14), 145224 (2007).
- [75] L. Zhao, M. P. Y. Wu, K.-W. Yeh and M.-K. Wu, *Solid State Communications* **151** (23), 1728-1732 (2011).
- [76] A. Kumarasiri, E. Abdelhamid, A. Dixit and G. Lawes, *Physical Review B* **91** (1), 014420 (2015).
- [77] A. Dixit and G. Lawes, *Journal of Physics: Condensed Matter* **21** (45), 456003 (2009).
- [78] A. Dixit, B. Ramchandran, Y. K. Kuo and G. Lawes, presented at the 2015 IEEE Magnetics Conference (INTERMAG), 2015 (unpublished).
- [79] A. F. Bovina, I. A. Gudim, E. V. Eremin and V. L. Temerov, *Crystallography Reports* **57** (7), 955-958 (2012).

- [80] H. Tian, I. E. Wachs and L. E. Briand, *The Journal of Physical Chemistry B* **109** (49), 23491-23499 (2005).
- [81] J. I. Hoppe, *Journal of Chemical Education* **49** (7), 505 (1972).
- [82] A. Dixit, G. Lawes and A. B. Harris, *Physical Review B* **82** (2), 024430 (2010).
- [83] P. M. Chaikin and T. C. Lubensky, *Principles of condensed matter physics*. (Cambridge Univ Press, 2000).
- [84] G. Lawes, T. Kimura, C. Varma, M. Subramanian, N. Rogado, R. Cava and A. Ramirez, *Progress in Solid State Chemistry* **37** (1), 40-54 (2009).
- [85] M. Mochizuki, N. Furukawa and N. Nagaosa, *Physical Review B* **84** (14), 144409 (2011).
- [86] M. Iizumi, T. F. Koetzle, G. Shirane, S. Chikazumi, M. Matsui and S. Todo, *Acta Crystallographica Section B* **38** (8), 2121-2133 (1982).
- [87] M. A. Gilleo, *Physical Review* **109** (3), 777-781 (1958).
- [88] D. O. Smith, *Physical Review* **102** (4), 959-963 (1956).
- [89] Z. L. Liu, Y. J. Liu, K. L. Yao, Z. H. Ding, J. Tao and X. Wang, *Journal of Materials Synthesis and Processing* **10** (2), 83-87 (2002).
- [90] E. Verwey, *Nature* **144** (3642), 327-328 (1939).
- [91] W. Friedrich, *Journal of Physics: Condensed Matter* **14** (12), R285 (2002).
- [92] J. Tang, K.-Y. Wang and W. Zhou, *Journal of Applied Physics* **89** (11), 7690-7692 (2001).
- [93] M. Ziese, P. D. Esquinazi, D. Pantel, M. Alexe, N. M. Nemes and M. Garcia-Hernández, *Journal of Physics: Condensed Matter* **24** (8), 086007 (2012).
- [94] J. P. Wright, J. P. Attfield and P. G. Radaelli, *Physical Review Letters* **87** (26), 266401 (2001).

- [95] P. W. Anderson, *Physical Review* **102** (4), 1008-1013 (1956).
- [96] Y. Miyamoto, S. and s. Chikazumi, *Journal of the Physical Society of Japan* **57** (6), 2040-2050 (1988).
- [97] M. Kobayashi, Y. Akishige and E. Sawaguchi, *Journal of the Physical Society of Japan* **55** (11), 4044-4052 (1986).
- [98] K. Yamauchi, T. Fukushima and S. Picozzi, *Physical Review B* **79** (21), 212404 (2009).
- [99] S. S. Laha, "Understanding the physics of magnetic nanoparticles and their applications in the biomedical field" PhD Thesis, Wayne State University, 2015.
- [100] Z. Zhou and Z.-R. Lu, *Wiley interdisciplinary reviews. Nanomedicine and nanobiotechnology* **5** (1), 1-18 (2013).
- [101] H. Rudolf, D. Silvio, M. Robert and Z. Matthias, *Journal of Physics: Condensed Matter* **18** (38), S2919 (2006).
- [102] P. Drake, H.-J. Cho, P.-S. Shih, C.-H. Kao, K.-F. Lee, C.-H. Kuo, X.-Z. Lin and Y.-J. Lin, *Journal of Materials Chemistry* **17** (46), 4914-4918 (2007).
- [103] M. Nair, R. Guduru, P. Liang, J. Hong, V. Sagar and S. Khizroev, *Nat Commun* **4**, 1707 (2013).
- [104] G. A. Silva, *BMC neuroscience* **9** (3), 1 (2008).
- [105] Y.-I. Kim, W. B. Im, M. K. Jeon, Y.-H. Lee, K.-B. Kim and K.-S. Ryu, *Journal of nanoscience and nanotechnology* **11** (1), 810-814 (2011).
- [106] R. t. Shannon, *Acta Crystallographica Section A: Crystal Physics, Diffraction, Theoretical and General Crystallography* **32** (5), 751-767 (1976).
- [107] A. L. Patterson, *Physical Review* **56** (10), 978-982 (1939).

- [108] S. J. Orfanidis, *Electromagnetic waves and antennas*. (Rutgers University New Brunswick, NJ, 2002).
- [109] M. Schönherr, B. Slater, J. Hutter and J. VandeVondele, *The Journal of Physical Chemistry B* **118** (2), 590-596 (2014).
- [110] K. J. Andrew, *Journal of Physics D: Applied Physics* **32** (14), R57 (1999).
- [111] D. C. Lupascu, Y. A. Genenko and N. Balke, *Journal of the American Ceramic Society* **89** (1), 224-229 (2006).
- [112] A. K. Jonscher, *Thin Solid Films* **100** (4), 329-334 (1983).
- [113] G. Lawes and G. Srinivasan, *Journal of Physics D: Applied Physics* **44** (24), 243001 (2011).
- [114] T. Kimura, S. Kawamoto, I. Yamada, M. Azuma, M. Takano and Y. Tokura, *Physical Review B* **67** (18), 180401 (2003).
- [115] C. W. Heaps, *Physical Review* **24** (1), 60-67 (1924).
- [116] G. Balaji, R. A. Narayanan, A. Weber, F. Mohammad and C. S. S. R. Kumar, *Materials Science and Engineering: B* **177** (1), 14-18 (2012).
- [117] M. Alexe, M. Ziese, D. Hesse, P. Esquinazi, K. Yamauchi, T. Fukushima, S. Picozzi and U. Gösele, *Advanced Materials* **21** (44), 4452 (2009).
- [118] F. Schrettle, S. Krohns, P. Lunkenheimer, V. A. M. Brabers and A. Loidl, *Physical Review B* **83** (19), 195109 (2011).
- [119] Quantum Design PPMS Heat Capacity User Option's Manual, 2004
- [120] C. L. Snow, Q. Shi, J. Boerio-Goates and B. F. Woodfield, *The Journal of Physical Chemistry C* **114** (49), 21100-21108 (2010).

- [121] Ö. Özdemir, D. J. Dunlop and B. M. Moskowitz, *Geophysical Research Letters* **20** (16), 1671-1674 (1993).
- [122] J. Liu, X. Lu and C. Wu, *Membranes* **3** (4), 389-405 (2013).
- [123] K. Heiji, *Japanese Journal of Applied Physics* **8** (7), 975 (1969).
- [124] S. B. Lang, B. D. Sollish, M. Moshitzky and E. H. Frei, *Ferroelectrics* **24** (1), 289-292 (1980).
- [125] A. J. Lovinger, *Macromolecules* **15** (1), 40-44 (1982).
- [126] K. Chelakara Satyanarayana and K. Bolton, *Polymer* **53** (14), 2927-2934 (2012).
- [127] L. Li, M. Zhang, M. Rong and W. Ruan, *RSC Advances* **4** (8), 3938-3943 (2014).
- [128] S. Weinhold, M. H. Litt and J. B. Lando, *Journal of Polymer Science: Polymer Letters Edition* **17** (9), 585-589 (1979).
- [129] M. Bachmann, W. L. Gordon, S. Weinhold and J. B. Lando, *Journal of Applied Physics* **51** (10), 5095-5099 (1980).
- [130] M.-m. Tao, F. Liu, B.-r. Ma and L.-x. Xue, *Desalination* **316**, 137-145 (2013).
- [131] P. Martins, C. Caparros, R. Gonçalves, P. Martins, M. Benelmekki, G. Botelho and S. Lanceros-Mendez, *The Journal of Physical Chemistry C* **116** (29), 15790-15794 (2012).
- [132] M. El Achaby, F. Arrakhiz, S. Vaudreuil, E. Essassi and A. Qaiss, *Applied Surface Science* **258** (19), 7668-7677 (2012).
- [133] S. F. Mendes, C. M. Costa, C. Caparros, V. Sencadas and S. Lanceros-Méndez, *Journal of Materials Science* **47** (3), 1378-1388 (2012).
- [134] P. I. Devi and K. Ramachandran, *Journal of Experimental Nanoscience* **6** (3), 281-293 (2011).
- [135] J. S. Dodds, F. N. Meyers and K. J. Loh, *IEEE Sensors Journal* **12** (6), 1889-1890 (2012).



- [136] M. S. Gaur and A. P. Indolia, *Journal of thermal analysis and calorimetry* **103** (3), 977-985 (2011).
- [137] A. Chilvery, A. Batra and T. Mychal, *Physical Science International Journal* **4** (5), 734 (2014).
- [138] D. He, K. Cheng, T. Peng, X. Sun, M. Pan and S. Mu, *Journal of Materials Chemistry* **22** (39), 21298-21304 (2012).
- [139] D. Wang, Y. Bao, J.-W. Zha, J. Zhao, Z.-M. Dang and G.-H. Hu, *ACS applied materials & interfaces* **4** (11), 6273-6279 (2012).
- [140] E. H. Abdelhamid, O. D. Jayakumar, V. Kotari, B. P. Mandal, R. Rao, V. M. Naik, R. Naik and A. K. Tyagi, *RSC Advances* **6** (24), 20089-20094 (2016).
- [141] G. T. Davis, J. E. McKinney, M. G. Broadhurst and S. C. Roth, *Journal of Applied Physics* **49** (10), 4998-5002 (1978).
- [142] R. Gregorio, *Journal of Applied Polymer Science* **100** (4), 3272-3279 (2006).
- [143] J. Zhang, H. Yang, G. Shen, P. Cheng, J. Zhang and S. Guo, *Chemical Communications* **46** (7), 1112-1114 (2010).
- [144] S. Satapathy, S. Pawar, P. Gupta and K. Varma, *Bulletin of Materials Science* **34** (4), 727-733 (2011).
- [145] T. Boccaccio, A. Bottino, G. Capannelli and P. Piaggio, *Journal of Membrane Science* **210** (2), 315-329 (2002).
- [146] Y. Bormashenko, R. Pogreb, O. Stanevsky and E. Bormashenko, *Polymer Testing* **23** (7), 791-796 (2004).
- [147] S. Lanceros-Mendez, J. Mano, A. Costa and V. Schmidt, *Journal of Macromolecular Science, Part B* **40** (3-4), 517-527 (2001).

- [148] V. Sencadas, R. Gregorio Jr and S. Lanceros-Méndez, *Journal of Macromolecular Science*® **48** (3), 514-525 (2009).
- [149] B. P. Mandal, K. Vasundhara, E. Abdelhamid, G. Lawes, H. G. Salunke and A. K. Tyagi, *The Journal of Physical Chemistry C* **118** (36), 20819-20825 (2014).
- [150] S. Chandran, N. Begam, V. Padmanabhan and J. Basu, *Nature communications* **5** (2014).
- [151] B. Ramachandran, A. Dixit, R. Naik, G. Lawes and M. R. Rao, *Journal of Applied Physics* **110** (10), 104105 (2011).
- [152] D. P. Dutta, B. P. Mandal, R. Naik, G. Lawes and A. K. Tyagi, *The Journal of Physical Chemistry C* **117** (5), 2382-2389 (2013).
- [153] O. Jayakumar, E. H. Abdelhamid, V. Kotari, B. P. Mandal, R. Rao, V. M. Naik, R. Naik and A. Tyagi, *Dalton Transactions* **44** (36), 15872-15881 (2015).
- [154] F. He, S. Lau, H. L. Chan and J. Fan, *Advanced Materials* **21** (6), 710-715 (2009).
- [155] Y. Kuwahara, M. Ueyama, R. Yagi, M. Koinuma, T. Ogata, S. Kim, Y. Matsumoto and S. Kurihara, *Materials Letters* **108**, 308-310 (2013).
- [156] J. Scott, *Journal of Physics: Condensed Matter* **20** (2), 021001 (2007).
- [157] P. Anithakumari, B. P. Mandal, E. Abdelhamid, R. Naik and A. K. Tyagi, *RSC Advances* **6** (19), 16073-16080 (2016).
- [158] G. Srinivasan, I. Zavislyak and A. Tatarenko, *Applied physics letters* **89** (15), 152508-152508 (2006).
- [159] H. K. Kim, L. T. Schelhas, S. Keller, J. L. Hockel, S. H. Tolbert and G. P. Carman, *Nano letters* **13** (3), 884-888 (2013).
- [160] G. Goya, T. S. Berquó, F. C. Fonseca and M. Morales, *Journal of Applied Physics* **94** (5), 3520-3528 (2003).

- [161] Z. Fisk and J. Remeika, Elsevier Science Publishers, Handbook on the Physics and Chemistry of Rare Earths. **12**, 53-70 (1989).
- [162] R. Olesinski and G. Abbaschian, Journal of Phase Equilibria **6** (6), 545-548 (1985).
- [163] G. Wolff and A. Mlavsky, (Plenum Press, New York, 1974).

**ABSTRACT****MULTIFERROICITY IN IRON VANADATE, MAGNETITE AND  
POLYVINYLIDENE FLUORIDE NANOCOMPOSITE FILMS**

by

**EHAB ABDELHAMID****August 2016****Advisors:** Drs. Boris Nadgorny and Ratna Naik**Major:** Physics**Degree:** Doctor of Philosophy

With the increasing demand on cheaper and better performance multifunctional materials for different applications, it is becoming more crucial to have a better understanding of the physics needed to tailor more devices and materials to fit better in every day's technological needs. Materials which show more than one ferroic order simultaneously –namely, multiferroics– are of particular importance for their potential applications as multiple state memory elements, transducers and electrically tunable microwave devices.

In this work, we studied  $\text{FeVO}_4$  single crystals as an example on low symmetry multiferroics. We focused on the anisotropy in those crystals in an attempt to nail the origin of the ferroelectric and magnetoelectric behaviors. Our data suggest the crystallographic *a*-axis to be a favorable direction for magnetic and ferroelectric alignment.  $\text{FeVO}_4$  single crystals doped with Zn and Mn were also prepared to investigate the role of magnetically induced lattice distortions (in case of Zn) in creating the spontaneous ferroelectric moment, and to test for the role played by Dzyaloshinskii-Moriya interaction (in case of Mn) in  $\text{FeVO}_4$  ferroelectricity. Doped crystals were shown to retain the ferroelectric nature as well.

Gd-doped  $\text{Fe}_3\text{O}_4$  nanoparticle system –a charge ordered ferroelectric– was also studied. Partial substitution of  $\text{Fe}^{3+}$  with  $\text{Gd}^{3+}$  aims to induce chemical pressure, based on the considerable difference in ionic radii. The dielectric constant of  $\text{Fe}_3\text{O}_4$  was found to increase upon doping with Gd. Also, the ferroelectric polarization moment was found to be higher for the 5% Gd-doped sample. Our magneto-dielectric data were not conclusive about the nature of magnetoelectric coupling in this system.

Strain induced magnetoelectric coupling in polyvinylidene difluoride (PVDF)-based film composites was investigated as well. The use of reduced graphene oxide (RGO) and ZnO as nanofillers in PVDF- $\text{Fe}_3\text{O}_4$  hybrid films was found to reduce the piezoelectric  $\beta$ -phase (i.e.: the ferroelectric phase) content, even though PVDF-RGO composite films showed the highest ferroelectric polarization moment in the measured set. Using graphene oxide (GO), on the other hand, was shown to increase the  $\beta$ -phase content and to enhance the ferroelectric response as well. We also show that PVDF films carrying surface-functionalized Ni nanoparticles show enhanced ferroelectric polarization and higher magneto-dielectric coupling as compared to films with non-functionalized Ni. Finally, an enhancement in the dielectric permittivity and magneto-dielectric behavior was seen in barium hexaferrite (BHF)-loaded films.

## AUTOBIOGRAPHICAL STATEMENT

Ehab H. Abdelhamid

### Education:

- Ph.D. in Physics. Wayne State University, Detroit MI. (July 2016)
- M.Sc. in Physics. Wayne State University, Detroit MI. (June 2011)
- B.Sc. in Physics. Ain Shams University, Cairo Egypt. (July 2005)

### Experiences:

- Graduate Research Assistant. Department of Physics and Astronomy, Wayne State University, Detroit MI. (June 2010 – Present).
- Teaching Assistant. Department of Physics and Astronomy, Wayne State University, Detroit MI. (September 2009 – December 2013).
- Teaching Assistant. The British University in Egypt, School of Engineering, Cairo, Egypt. (September 2007 – August 2009).
- Teaching Assistant. Misr University for Science and Technology, School of Engineering, Cairo, Egypt. (January 2006 – August 2007).

### Publications:

- E Abdelhamid, OD Jayakumar, V Kotari, BP Mandal, R Rao, VM Naik, R Naik, AK Tyagi. “Multiferroic PVDF– $Fe_3O_4$  hybrid films with reduced graphene oxide and ZnO nanofillers”. **RSC Advances** 6 (24) 2016, 20089-20094
- OD Jayakumar, E Abdelhamid, V Kotari, BP Mandal, R Rao, VM Naik, R Naik, AK Tyagi. “Fabrication of flexible and self-standing inorganic–organic three phase magneto-dielectric PVDF based multiferroic nanocomposite films through a small loading of graphene oxide (GO) and  $Fe_3O_4$  nanoparticles”. **Dalton Transactions** 44 (36) 2015, 15872-15881
- BP Mandal, V Kotari, E Abdelhamid, G Lawes, HG Salunke, AK Tyagi. “Improvement of magneto-dielectric coupling by surface functionalization of nickel nanoparticles in Ni and polyvinylidene fluoride nanohybrids”. **The Journal of Physical Chemistry C** 118 (36) 2014, 20819-20825
- P Anithakumari, BP Mandal, E Abdelhamid, R Naik, AK Tyagi. “Enhancement of dielectric, ferroelectric and magneto-dielectric properties in PVDF– $BaFe_{12}O_{19}$  composites: a step towards miniaturized electronic devices”. **RSC Advances** 6 (19) 2016, 16073-16080
- A Kumarasiri, E Abdelhamid, A Dixit, G Lawes. “Effect of transition metal doping on multiferroic ordering in  $FeVO_4$ ”. **Physical Review B** 91 (1) 2015, 014420
- MA Hettiarachchi, E Abdelhamid, B Nadgorny, SL Brock. “Synthesis of colloidal MnSb nanoparticles: consequences of size and surface characteristics on magnetic properties”. **Journal of Materials Chemistry C** 28 (4) 2016, 6790-6797

### Awards:

- Daniel R. Gustafson graduate student teaching award, Department of Physics, Wayne State University. (2011)